Study of Complex Ferroelectric and Antiferroelectric Systems

by

Zihe Ren

B.Sc., University of British Columbia, 2009

Thesis Submitted In Partial Fulfillment of the
Requirements for the Degree of
Doctor of Philosophy

in the
Department of Chemistry
Faculty of Science

SIMON FRASER UNIVERSITY

Fall 2014

Approval

Name: **Zihe Ren**

Degree: **Doctor of Philosophy (Chemistry)**

Title: ***Study of Complex Ferroelectric and Antiferroelectric Systems***

Examining Committee: **Chair:** Dr. Krzysztof Starosta
Associate Professor

Dr. Zuo-Guang Ye
Senior Supervisor
Professor

Dr. Steven Holdcroft
Supervisor
Professor

Dr. Gary W. Leach
Supervisor
Associate Professor

Dr. Michael H. Eikerling
Internal Examiner
Professor

Dr. Thomas R. Shrout
External Examiner
Professor
Department of Material Sciences and Engineering
Pennsylvania State University

Date Defended/Approved: December 12, 2014

Partial Copyright Licence

Abstract

Rhombohedral (R), monoclinic (M_A/M_C) and tetragonal (T) phases are found in coexistence in a compositionally segregated $xPb(In_{1/2}Nb_{1/2})O_3$- $yPb(Mg_{1/3}Nb_{2/3})O_3$-$zPbTiO_3$ (PIN-PMN-PT) (nominal composition x/y/z = 30/35/35) single crystal. Polarized light (PLM) measurements and X-ray diffraction (XRD) on both single crystal and ceramic series confirms the existence of 2 different monoclinic phases. A phase diagram in the MPB region of the PIN-PMN-PT solid solution is proposed based on both single crystals and ceramic material.

Further study on the temperature driven rhombohedral (R) (*R*3*m*) → monoclinic (M_A) phase transition in the single crystals and ceramics with MPB composition are carried out. It was found that the rhombohedral domain is able to return to its original state after annealed at above the R→M_A phase transition temperature (T_{R-M}) but below the Currie temperature (T_C). A polarization reversal model is proposed based on the polarization rotation theory.

Solid solutions of $(1-x)Pb(Mg_{1/2}W_{1/2})O_3$-$xPb(M_{1/2}W_{1/2})O_3$(M = Zn^{2+} and Mn^{2+}) have been prepared by solid state reaction with composition x up to 30% for Zn and 50% for Mn. The influence of Zn^{2+} and Mn^{2+} on structure, electrical and magnetic properties are revealed. $(1-x)PbZrO_3$-$xPb(Mn_{1/2}W_{1/2})O_3$ (x = 0 - 0.1) as another new solid solution system was also prepared by the solid state reaction method. Its crystal structure, dielectric properties and antiferroelectricity were investigated and it was proven to be an excellent candidate for energy storage devices.

In summary, the study for PIN-PMN-PT ternary solid solution near its MPB composition shall provide a general guideline for designing high performance peizocrystals. The study of PZ-based and PMW-based antiferroelectric solid solutions provided better understanding of antiferroelectric perovskites and provides a different approach for the design of soft antiferroelectric material with high energy density.

Keywords: Perovksite, Ferroelectrics, Antiferroelectric, Solid solutions, Ceramics, Single crystals,

Dedication

Crane Never Dies!

Acknowledgements

First of all, I would like to express my deep gratitude to my senior supervisor, Dr. Zuo-Guang Ye for his guidance, support and encouragement during my PhD study. I would also like to thank my supervisory committee members, Dr. Gary Leach and Dr. Steven Holdcroft for their helpful advice. I would like to further my thanks to Dr. Michael Eikerling for being the internal examiner. My thanks also go to my external examiner, Dr. Thomas R. Shrout, for his valuable comments and suggestions. I thank all the members of Dr. Ye research group, both previous and present, for their support and friendship. I would especially like to thank Dr. Alexei A. Bokov for insightful discussion on data analysis, and Dr. Xifa Long, Dr. Yujuan Xie and Dr. Hamel Tailor for teaching me valuable experimental skills. I appreciate the financial and facility support from 4D Labs, Department of Chemistry, Simon Fraser University, the Natural Sciences and Engineering Research Council of Canada and the U.S. Office of Naval Research. Finally, I would like to thank my parents Cheng Ren and Heng Zhai, and my fiancée Zenan Jiang for their love and support. Without their encouragement, I would never have achieved this stage.

.

Table of Contents

List of Tables

List of Figures

List of Abbreviations

FE	Ferroelectric
AFE	Antiferroelectric
PE	Paraelectric
pc	Pseudocubic
PMN-PT	$Pb(Mg_{1/3}Nb_{2/3})O_3$-$PbTiO_3$
PIN-PMN-PT	$Pb(In_{1/2}Nb_{1/2})O_3$-$Pb(Mg_{1/3}Nb_{2/3})O_3$-$PbTiO_3$
PZT	$PbZrO_3$-$PbTiO_3$
PZN-PT	$Pb(Zn_{1/3}Nb_{2/3})O_3$-$PbTiO_3$
PZ	$PbZrO_3$
PMW	$Pb(Mg_{1/2}W_{1/2})O_3$
PZW	$Pb(Zn_{1/2}W_{1/2})O_3$
PMnW	$Pb(Mn_{1/2}W_{1/2})O_3$
MPB	Morphotropic phase boundary
XRD	X-ray diffraction
PLM	Polarized light microscopy
SQUID	Superconducting Quantum Interference Device
EPR	Electron Paramagnetic Resonance
SEM	Scanning Electron Microscopy
TEM	Transmission Electron Microscopy
EDS	Energy Dispersive Spectroscopy
d_{33}	Piezoelectric constant
k_p	Electromechanical coupling factor
Q_m	Mechanical quality factor
θ_M	Extinction angle for monoclinic phase
E_C	Coercive field
P_r	Remanent polarization
P_S	Spontaneous polarization
T_C	Curie temperature
ε'	Real part of permittivity
ε''	Imaginary part of permittivity
χ	Magnetic susceptibility

t	Tolerance factor
tanδ	Dielectric loss tangent
f_r	Resonance frequency
f_a	Antiresonance frequency
P	Polarizer
A	Analyzer
Δn	Birefringence
R	Retardation
λ	Wavelength
C	Curie constant
i	Pyroelectric current

Chapter 1: Introduction

This thesis presents the synthesis and characterization of several Pb-based complex perovskite ferroelectric/antiferroelectric material systems in the forms of ceramics and single crystals in the interest of providing comprehensive understanding of their electric properties. In this chapter, basic concepts and important background information will be introduced, including perovskite structure, piezoelectricity, ferroelectricity and antiferroelectricity. It provides an overview of the researches on $Pb(Mg_{1/3}Nb_{2/3})O_3$-$PbTiO_3$-based piezo/ferroelectric systems, $Pb(Mg_{1/2}W_{1/2})O_3$-based antiferroelectric system and $PbZrO_3$-based antiferroelectric system.

1.1. Perovskite Structure

Perovskite-type materials form an important class of functional materials. The materials with a perovskite structure generally possess ABX_3 formula. In all research projects presented within this thesis, ABO_3 form is used where O stands for oxygen. This crystal structure was first discovered in the mineral $CaTiO_3$ by Russian mineralogist Lev Perovski. A typical perovskite structure is shown in Fig.1.1.

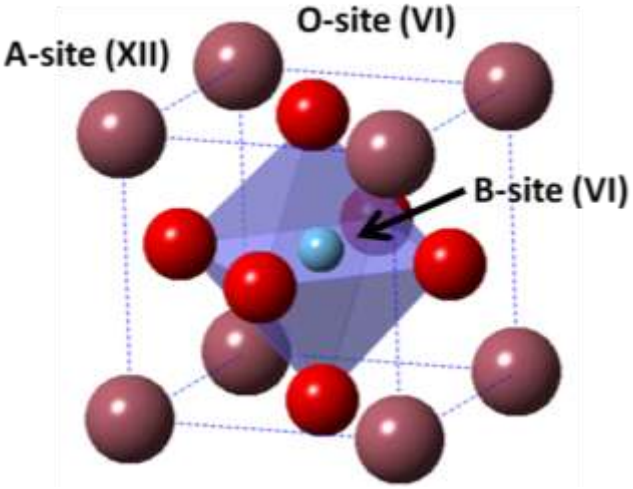

Figure 1.1 Prototype Perovskite ABO_3 structure with $\boldsymbol{Pm\bar{3}m}$ symmetry, with A-site cation at corner of unit cell, O^{2-} ion at face center of unit cell and B-cation at the center of oxygen octahedron

The perovskite compounds investigated in this thesis work have Pb^{2+} ions sitting at the A-site with 12 coordinates, Mg^{2+}, In^{3+}, Nb^{5+}, Ti^{4+} (for $Pb(In_{1/2}Nb_{1/2})O_3$-$Pb(Mg_{1/3}Nb_{2/3})O_3$-$PbTiO_3$ system) Zr^{4+}, , Mn^{2+} and W^{6+} (for $Pb(Mg_{1/2}W_{1/2})O_3$-based and $PbZrO_3$-based antiferroelectric systems) ions occupying the B-site with 6 coordinates. Oxygen ions are located at each of the 6 face centres, creating an oxygen octahedron in which the B-site cation is contained.

Due to the requirement of charge balance, with A-site being 2+ and oxygen being 2-, B-site cations must achieve a net charge of 4+. In addition, in order to maintain the stability of the perovskite structure, the size of cations must be taken into consideration and it is described in terms of tolerance factor *t*:

$$t = \frac{r_A + r_O}{\sqrt{2}\left(r_B + r_O\right)} \ , \tag{1.1}$$

where r_A, r_B, and r_O are the radii of the A(XII), B(VI) and O(VI) ions, respectively[1]. The tolerance factor *t* generally indicates the stability of the perovskite structure (with t = 1 for a perfectly cubic structure). A great range of cation combinations in the perovskite structure allows significant diversity and flexibility in material's properties, making

perovskite–type materials one of the most versatile members in the family of functional materials[2-7].

1.2. Piezoelectricity

The piezoelectric effect was first discovered by Jacques and Pierre Curie in 1880. The effect is exhibited in a lot of minerals such as quartz and Rochelle salt[8]. The prefix "Piezo" originates from the Greek with the meaning of pressure. Therefore, a piezoelectric material is capable to convert mechanical stress into electricity and vice versa. With these unique features, piezoelectric materials play an important role in industrial applications such as SONAR, medical ultrasonic imaging, transducers and actuators[9].

Piezoelectricity can be described by a linear relationship between electrical field and mechanical strain:

$$D_i = d_{ijk} X_{jk} \ , \tag{1.2}$$

$$x_{ij} = d_{kij} E_k \ , \tag{1.3}$$

Eq.(2) describes the direct effect of piezoelectricity, in which D is the electric displacement, *X* is the stress applied and d_{ijk} is the piezoelectric coefficient. Similarly, the Eq.(3) describes the converse effect in which *x* represents the strain and E is the applied external electric field. The electromechanical coupling factor *k* is another important specification for piezoelectric materials. It has the following expressions:

$$k^2 = \frac{\text{Mechanical output energy}}{\text{Electrical input energy}}, \tag{1.4}$$

Or

$$k'^2 = \frac{\text{Electrical output energy}}{\text{Mechanical input energy}}, \tag{1.5}$$

k-factor can also carry subscript indicating the nature of different coupling mechanisms. k_p is the planer coupling factor for a ceramic disc in which the radial coupling is measured between electric field applied in the direction of ceramic internal polarization

and the mechanical vibrations produced along the radial directions; k_{33} is similar to k_p but it measures the coupling factor for longitudinal vibrations for rod shape piezoelectric materials; k_{31} measures the coupling between the electric field parallel to the direction in which the material is polarized and the longitudinal vibrations perpendicular to direction in which the material is polarized

1.3. Ferroelectricity

Ferroelectric materials are subgroups of piezoelectric materials. Ferroelectric materials have spontaneous electrical polarization which can be reoriented in direction by the application of an external electric field[10]. The symmetry restriction for piezoelectric material is the lack of inversion center. There are twenty crystallographic point groups that meets the requirements piezoelectric material, ten of which possess a unique polar axis which allows polarization to be generated spontaneously. These groups are called pyroelectrics. The pyroelectrics with switchable polarizations form ferroelectrics. The most important characteristics of a ferroelectric material is the hysteretic behaviour in the relationship between polarization– electric field shown in Fig.1.2

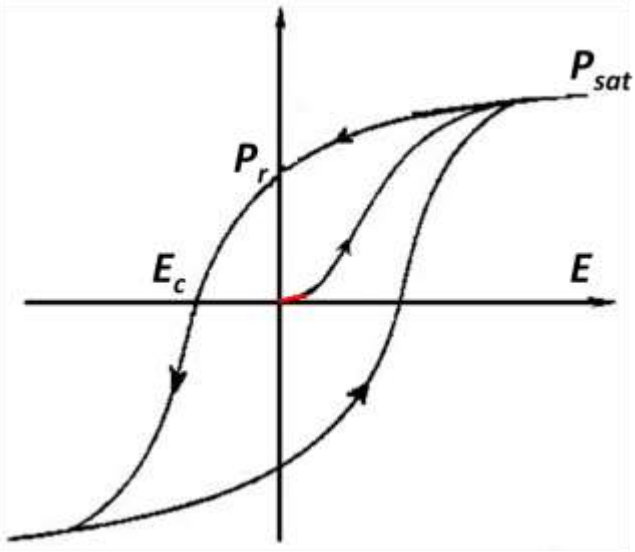

Figure 1.2 Schematic diagram of the hysteresis loop in the relation between polarization(P) and electric field(E) for a ferroelectric material showing saturated polarization (P_{sat}), remanent polarization (P_r) and coercive field (E_C)

Before the application of an external electric field, virgin ferroelectric ceramics have zero polarization. Once the electric field is applied, polarization first increases linearly as the initial field is not large enough to induce ferroelectric domain switching. Therefore, the P-E relationship behaves the same as a regular dielectric material (Red line in the center of the hysteresis loop in Fig.1.2). As the external field continues to increase up to a certain threshold value, electric dipoles in domains, which are originally pointing at random directions start to align towards the direction of the external field. In ferroelectric single crystal, this effect may lead to a monodomain state. In ferroelectric ceramic or thin films, due to large internal stress among grains, dipoles can only be partially aligned towards the direction of the field. Eventually, polarization will reach a maximum value which is defined as “saturated polarization”. Once all the domains are aligned, removing the external field will not result in the vanishing of the polarization. As a result, remanent polarization (P_r) can be obtained at zero field. At this stage, application of electric field up to certain level at opposite direction will lead to the removal of the remanent polarization. The value of the critical field which leads to the reduction of polarization to zero is defined as coercive field (E_C). Further increase of the field in the opposite direction will

lead to the saturation of polarization at that direction. Cycling of the field will complete the loop and a full hysteretic behaviour is thusly displayed.

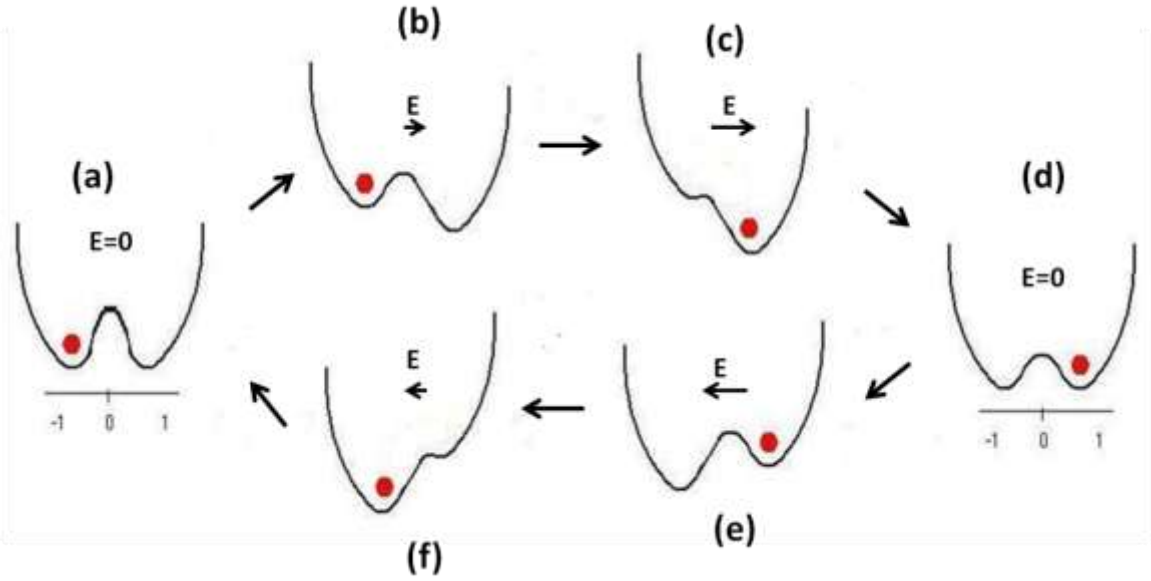

Figure 1.3 Energy diagram of hysteresis loop for ferroelectric material under the influence of an electric field

Ferroelectric hysteresis can also be explained in terms of a free energy change. In Fig. 1.3, (a) is the initial state with system sitting at the bottom of one of the double well potential. 1 and -1 designate the opposite polarization directions. With the increase of the field towards direction 1 (Fig. 1.3 (b)), the right hand side well bottom becomes lower in energy, i.e. the system with polarization pointing at direction 1 is energetically favourable. However, at this stage, the value of applied external field is not yet large enough to overcome the energy barrier and the system remains in the left well. In Fig. 1.3 (c), the field continues to increase and the system finally overcomes the energy barrier, leading to the switching of the polarization. Removing of the field in Fig. 1.3 (d) will not lead to the change of the polarization state and therefore the remnant polarization is obtained. Reversal of the field (Fig. 1.3 (e), (f)) gives similar but opposite effect with the system returning to its original state (Fig. 1.3 (a)).

Another important feature of ferroelectric materials are the Curie temperature (T_C). Above the T_C the crystal will lose its ferroelectricity and become paraelectric. In perovskite ferroelectrics, e.g. $BaTiO_3$, at above T_C, the material adopts an isotropic cubic structure with space group$Pm\bar{3}m$. When cooled down to below T_C, its unit cell becomes tetragonally distorted, with symmetry changed into *P*4*mm*. The B-site Ti^{4+} ion also shows an off-center displacement towards the face center of the unit cell, leading to noncentrosymmetric structure with the spontaneous generation of internal dipole[11].

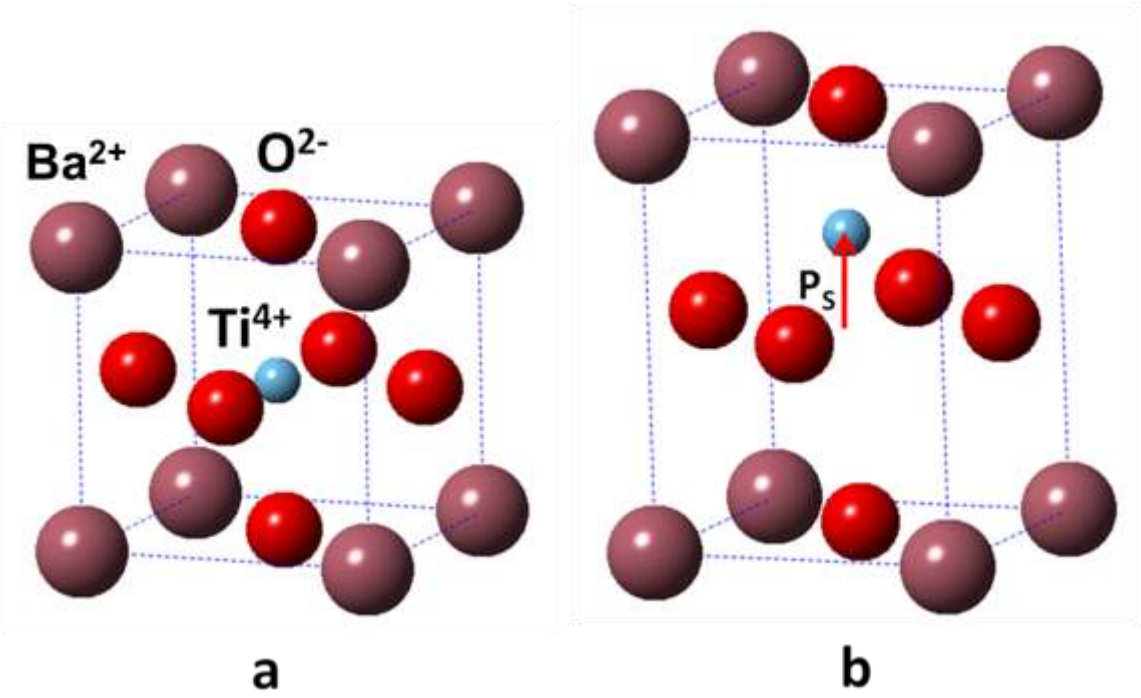

Figure 1.4 (a) Cubic prototype perovskite $BaTiO_3$ unit cell at above T_C. (b) Tetragonal $PbTiO_3$ unit cell at below T_C with the off-centre displacement of the B-site cation creating a spontaneous polarization (P_S).

1.4. Antiferroelectricity

An antiferroelectric material is a crystalline material with internal spontaneous dipoles. In contrast to ferroelectric materials, adjacent dipoles in antiferroelectric material are oriented in antiparallel directions. The symmetry restriction for a material to be

antiferroelectric is also different from ferroelectrics. It requires the net spontaneous polarization to be zero with non-polar symmetry. Like ferroelectricity, antiferroelectricity of a material is also dependent on temperatures, pressure and external electric field. Above a certain temperature, antiferroelectricity disappears. This temperature is named the antiferroelectric Curie temperature.[12]

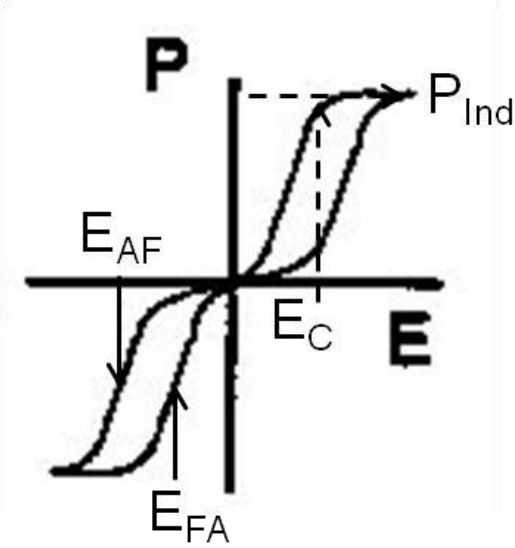

Figure 1.5 Schematic diagram of antiferroelectric double hysteresis loop showing maximum induced polarization (P_{Ind}), field required for AFE→FE phase transition (E_{AF}), field required for FE→AFE phase transition (E_{FA}), and definition of critical field (E_C) based on the average of E_{AF} and E_{FA}.

An antiferroelectric material is characterized by a double hysteretic behaviour (Fig. 1.5) in the relationship between polarization (P) and electric field (E)[13]. The virgin state of an antiferroelectric material shows zero net polarization in the absence of electric field. Increase of the external electric field will lead to near-linear polarization-electric field behaviour. At this stage, the measured polarization is mostly attributable to the dielectric response. As the external electric field continues to increase, an abrupt increase of polarization can be observed, indicating the occurrence of field-induced antiferroelectric→ferroelectric phase transition. The minimum field required for this transition is defined as E_{AF}. The induced polarization will keep increasing with field until it

reaches its maximum. Release of the field results in a hysteretic behaviour between polarization and electric field. The minimum field that the system requires before the abrupt drop of polarization is defined as E_{FA}. In some literature, due to the deviation of the double hysteresis loop from its ideal shape, critical field E_C was defined based on the average of E_{FA} and E_{AF}.

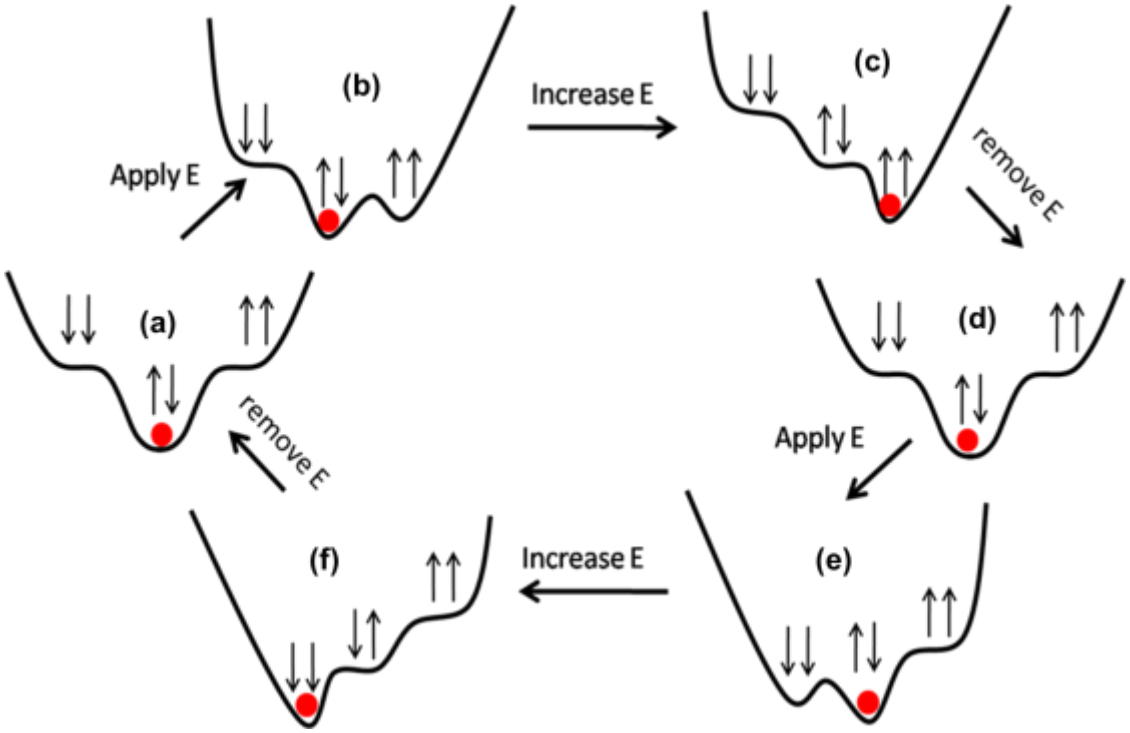

Figure 1.6 Energy diagram of double hysteresis loop for antiferroelectric material under the influence of electric field

Fig. 1.6 describes the change of free energy under the influence of an external electric field. Without the electric field, the spontaneous dipoles within antiferroelectric unit cell lie antiparallel to each other [Fig. 1.6 (a)]. Two ferroelectric states are also allowed but at higher energy level. Therefore the ferroelectric states are considered metastable. In Fig. 1.6 (b), the increase of the field will result in the lowering of the energy level of the ferroelectric phase which has both dipoles pointing in positive direction. Once the field is higher than a threshold level, AFE→FE phase transition is induced along with structural

phase transition. However, the ferroelectric state can only stay at global energy minimum under the presence of a large enough electric field. Withdrawal of the field will result in a complete restoration of the antiferroelectric phase.

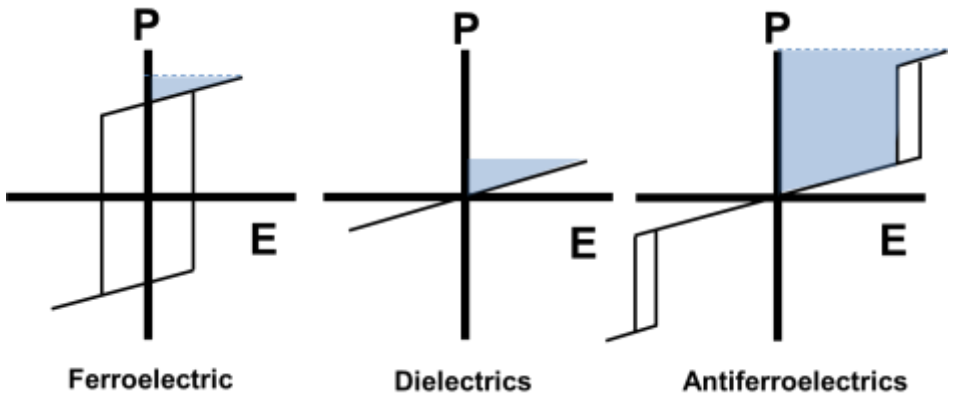

Figure 1.7 Polarization-electric field relationship in ferroelectric, dielectric and antiferroelectric systems

Antiferroelectric materials have the potential to be used as high-energy-storage capacitor. Fig. 1.7 shows the polarization-electric field relationship for typical ferroelectric, dielectric and antiferroelectric materials[12]. The shaded area represents the discharging energy. For ferroelectric materials, input electrical energy is used in domain switching and is retained within the material as remnant polarization. A dielectric material shows linear relationship between polarization and field. However the induced polarization in dielectric material is relatively low. In comparison, the antiferroelectric material is able to exist in metastable ferroelectric phases with large induced polarization; it returns to the non-polar antiferroelectric state when the field is withdrawn. Therefore the antiferroelectric material possesses a superior discharging ability compared with traditional dielectric capacitors[12].

1.5. $Pb(Mg_{1/3}Nb_{2/3})$-$PbTiO_3$-Based Ferroelectric System

The solid solution of $Pb(Mg_{1/3}Nb_{2/3})O_3$–$PbTiO_3$ (PMN-PT) crystallizes in a complex perovskite structure with Pb^{2+} occupying the A-sites and Mg^{2+}, Nb^{5+}, and the Ti^{4+} occupying the B-sites[14, 15]. This complex system is a combination of a relaxor ferroelectric (PMN) with a pseudocubic rhombohedral symmetry and a typical ferroelectric (PT) with tetragonal symmetry. (1-x)PMN-xPT with x< 0.20 is a typical relaxor ferroelectric material with a diffuse FE→PE phase transition and frequency dependent maxima of the dielectric constant. With the increase of x, the (1-x)PMN-xPT system shows more ferroelectric behaviour since $PbTiO_3$ is a typical ferroelectric material with a sharp first order FE→PE phase transition. As a result, mixture of phases is observed within certain composition range in the phase diagram. The composition range was thusly named morphotropic phase boundary (MPB) region. Although the nature of the MPB is still unclear, the highest piezoelectric performance is found within the MPB compositions of PMN-PT. One of the most widely accepted theories for the presence of high piezoelectric performance in MPB composition is the polarization rotation theory developed by Fu and Cohen based on the study in PZN single crystals[16]. Their research shows that for a rhombohedral PZN crystal with an electric field applied along the $[001]_{pc}$ direction, the polarization rotational pathway within the $(110)_{pc}$ plane is more energetically favourable compared with other rotation routes. Facilitated by the flattening of the energy profile, relatively large strain can be induced by an electric field. It is also believed that the polarization rotation mechanism can be influenced not only by the electric field, but also by chemical composition, external stress and temperature. Within the MPB region, rhombohedral, monoclinic and tetragonal phases exhibit very close energy profiles. Therefore, the polarization rotation can be achieved by slight variation in chemical composition, leading to large piezoelectric response.

Although the PMN-PT solid solution shows excellent performance in piezoelectric response, there are still several severe drawbacks, which limit its application. In the PMN-PT system, there exists a rhombohedral to tetragonal transition temperature (T_{RT}) within the range from 50 to 120 ˚C. In addition, the T_C of the system is also much lower than the traditional PZT material, which significantly limits the operating temperature range due to the thermal depoling effect. For applications such as actuators in fuel

injection systems, stability in piezoelectric performance is vital[17]. Therefore, the third component $Pb(In_{1/2}Nb_{1/2})O_3$ is introduced to the PMN-PT binary system, forming a ternary solid solution which overcomes the drawbacks of the PMN-PT binary system.

1.6. $Pb(Mg_{1/2}W_{1/2})O_3$-Based Antiferroelectric System

$Pb(Mg_{1/2}W_{1/2})O_3$ (PMW) was first synthesized in 1959 and is known to have an ordered structure with the orthorhombic centrosymmetric space group *Pmcn*[18]. Based on the diffraction methods, its antiferroelectricity was revealed by the antiparallel displacements of Pb^{2+} ions in the [100] and [010] directions in the cubic perovskite framework (Fig. 1.9)[19, 20]. A sharp antiferroelectric (AFE) → paraelectric (PE) phase transition was also demonstrated by dielectric spectroscopy at a Curie temperature of 38 ˚C. Above T_C, the system adopts the cubic $Fm\bar{3}m$ symmetry due to the ordering between Mg^{2+} and W^{6+}.

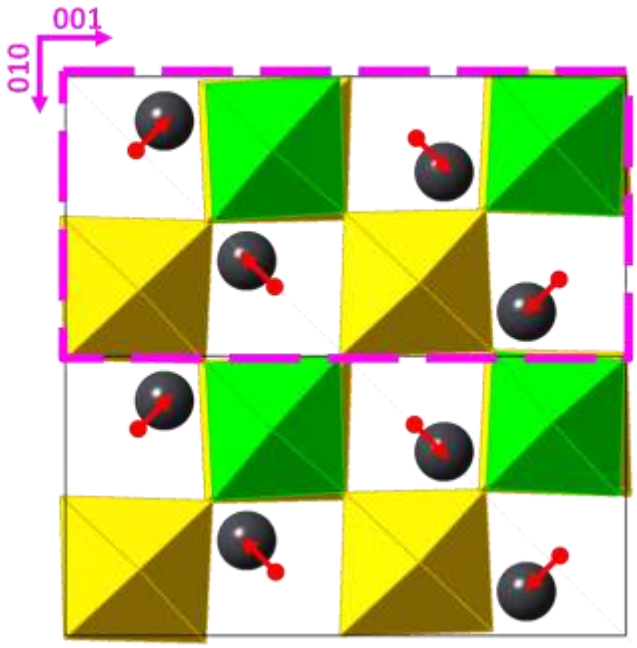

Figure 1.8 Schematic drawings of the $Pb(Mg_{1/2}W_{1/2})O_3$ unit cell (pink rectangle) with *Pmcn* symmetry W^{6+} and Mg^{2+} ions are at inside the green and yellow octahedrons, respectively. Pb-displacements are exaggerated along the $[010]_{pc}$ and $[001]_{pc}$ directions, as indicated by red arrows.

For phase pure $Pb(B^{2+}B'^{6+})O_3$ systems, due to the large difference in charges, it is very difficult to disrupt the ordering between B and B' ions. Therefore, very few $Pb(B^{2+}B'^{6+})O_3$-based solid solutions have been reported, which is mainly due to the low solubility limit. However, the high degree of order of $Pb(Mg_{1/2}W_{1/2})O_3$ makes it possible to make certain types of perovskite phases, which cannot be synthesized under conventional solid state reaction method, such as $Pb(Zn_{1/2}W_{1/2})O3$ or $Pb(Mn_{1/2}W_{1/2})O_3$-based solid solutions. In this work, a new $(1-x)Pb(Mg_{1/2}W_{1/2})O_3$-$xPb(Zn_{1/2}W_{1/2})O_3$ solid solution has been synthesized and its dielectric properties characterized.

1.7. $PbZrO_3$-Based Antiferroelectric System

At room temperature $PbZrO_3$ adopts an orthorhombic structure with the *Pbam* symmetry. The antiferroelectricity of $PbZrO_3$ originates from the antiparallel displacement of Pb^{2+} ions below the Curie temperature (T_C = 236 ˚C)[21-24]. Refinement of X-ray diffraction patterns revealed that Pb^{2+} ions are displaced towards $\{110\}_{pc}$ plane in the pseudocubic framework. As the result of Pb-displacements, $PbZrO_3$shows the double hysteretic behaviour associated with electric-field-induced antiferroelectric (AFE) - ferroelectric (FE) phase transition. In previous experiments on $PbZrO_3$-based antiferroelectric materials, it was found that the electric field aligns the displacements of Pb^{2+} ions in the same direction and therefore induces a structural phase transition from orthorhombic/tetragonal into rhombohedral symmetry[25].

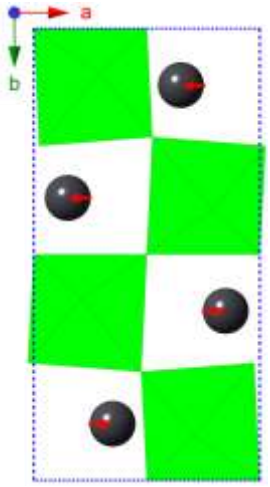

Figure 1.9 Schematic drawing of the orthorhombic (dashed blue) unit cells of the $PbZrO_3$ projected on the a-b plane, with the direction of Pb^{2+} displacements indicated by red arrows.

In order to make use of the AFE-FE phase transition for applications such as energy storage devices, “softening” of the material must be achieved. In this thesis, softening of a ferroelectric or antiferroelectric material means the lowering of the threshold field of domain/polarization switching. The approach is to make the composition of an antiferroelectric material close to the morphotropic phase boundary region (MPB). This MPB region shall contain the mixture of antiferroelectric and ferroelectric phases. According to Jaffe, there are two essential criteria: 1) with the increase of temperature, FE→ AFE → PE phase transition sequence shall be achieved; 2) the dielectric constant maximum at the AFE → PE transition shall be as high as possible. The reason behind these two criteria is to make the energy level as close as possible between the ferroelectric and antiferroelectric states during the FE→AFE and AFE → PE transitions. Chemical modification with Sn^{4+} was first used to meet the two criteria. Later substitution experiments with La^{3+}, Ti^{4+}, $Nb^{5+}$and Hf^{4+}also showed improvement in the electrical properties[26-28].

1.8. Objective and Organization of the Thesis

In the past decade, PMN-PT-based high performance piezoelectric materials have been considered as potential candidates to replace traditional $Pb(Zr,Ti)O_3$ (PZT) material. Continued efforts have been put to develop new solutions to overcome the limitations of the PMN-PT by chemical modifications. In this thesis, one of the most promising candidates, $Pb(In_{1/2}Nb_{1/2})O_3$–$Pb(Mg_{1/3}Nb_{2/3})O_3$–$PbTiO_3$(PIN-PMN-PT) ternary system was investigated. Our objective is to (i) establish a comprehensive phase diagram of PIN-PMN-PT system from ceramic with various compositions, (ii) to learn the growth behaviour of PIN-PMN-PT single crystal and (iii) to study the effect of external electric field, high temperature annealing treatments and oxygen vacancies on the structure and properties of PIN-PMN-PT single crystals.

$Pb(Mg_{1/2}W_{1/2})O_3$ (PMW) as a completely ordered system has been proven to be difficult to form a solid solution with other perovskite material due to the large disparity in the size and the change of B-cations. However, its high degree of ordering provides unique opportunities to explore the effects of certain elements on the structure and properties of this antiferroelectric system. In this work, the isovalent substitution method was used by partially replacing Mg^{2+} with Zn^{2+} and Mn^{2+}. Therefore, $Pb(Mg_{1/2}W_{1/2})O_3$-$Pb(M_{1/2}W_{1/2})O_3$ (M = Zn and Mn) solid solutions are synthesized with solid state reaction method. Their mechanical, electrical and magnetic properties are thoroughly investigated.

$PbZrO_3$ is one of the most widely studied antiferroelectric materials. When the applied external electric field exceed the threshold value, E_{AF}, an antiferroelectric (AFE) → ferroelectric (FE) phase transition will occur, manifesting itself in double hysteresis polarization –electric field loop. However, for pure $PbZrO_3$, the threshold field is too high to achieve AFE→FE phase transition at room temperature. In order to observe the field-induced AFE-FE phase transition before dielectric breakdown occurs, high temperature measurement or chemical modification is required to reduce the critical field for polarization switching. Previous research showed that by doping with La^{3+}, Ti^{4+}, Nb^{5+}, Sn^{4+} and Hf^{4+} in $PbZrO_3$, the electrical properties can be optimized. In this work, an alternative approach is used by adding another antiferroelectric material $Pb(Mn_{1/2}W_{1/2})O_3$ to form $PbZrO_3$ - $Pb(Mn_{1/2}W_{1/2})O_3$ solid solution. Experiments show that by the addition of $Pb(Mn_{1/2}W_{1/2})O_3$, the $PbZrO_3$ - $Pb(Mn_{1/2}W_{1/2})O_3$ solid solution system attains a higher

induced polarization, lower critical field and denser ceramics. It also leads to the generation of a ferroelectric intermediate phase with the increase of the $Pb(Mn_{1/2}W_{1/2})O_3$ substitution level.

1.8.1. $Pb(In_{1/2}Nb_{1/2})O_3 – Pb(Mg_{1/3}Nb_{2/3})O_3–PbTiO_3$ (PIN-PMN-PT) Ternary Ferroelectric Solid Solution System

The $Pb(In_{1/2}Nb_{1/2})O_3–Pb(Mg_{1/3}Nb_{2/3})O_3–PbTiO_3$ (PIN-PMN-PT) ternary solid solution system is studied in **Chapter 3**. It begins with a general introduction of the system, including literature review on the development of PIN-PMN-PT system in the past decades. Based on previous researches, we estimate the chemical composition in the morphotropic phase boundary region. High temperature X-ray powder diffraction is used to determine the structure of the ceramic system. Low symmetry monoclinic phases were discovered based on the refinement of x-ray patterns. Growth of PIN-PMN-PT single crystals is also performed. Analyzing the single crystal with polarized light microscopy provides solid evidence that there exists a monoclinic M_C phase (*Pm*) in the morphotropic phase boundary region. Following the discovery of the monoclinic M_C phase, a series of poling and annealing experiments were performed, demonstrating that oxygen vacancies within the single crystals will collectively migrate under the influence of an external electric field. Furthermore, such migration behaviour can also result in an irreversible monoclinic→tetragonal phase transition. A phenomenological model was developed to explain this behaviour. In the end of the Chapter 3, polarization reversal effect is discussed based on the evidence collected from PIN-PMN-PT single crystals and the ceramic system. It was found that for PIN-PMN-PT single crystal with rhombohedral(*R*3*m*)→monoclinic(*Cm*) phase transition, the domain pattern can be restored if the sample is annealed at $T_{RM}<T<T_C$. Similar behaviour was found in the ceramic system with similar compositions as the piezoelectric constant of the ceramic does not decay significantly when annealed at $T_{RM}<T<T_C$. A model is developed based on previously published polarization rotation theory to provide direction for designing piezoelectric materials with high temperature resistance.

1.8.2. $Pb(Mg_{1/2}W_{1/2})O_3$ –$Pb(M_{1/2}W_{1/2})O_3$ (M = Zn and Mn) Binary Antiferroelectric Solid Solution System

Chapter 4 of the thesis is on the structure of the $Pb(Mg_{1/2}W_{1/2})O_3$ (PMW)-based new antiferroelectric solid solution systems. It introduces the synthesis and characterization of the (1-x)$Pb(Mg_{1/2}W_{1/2})O_3$ - x$Pb(Zn_{1/2}W_{1/2})O_3$(PMW-PZW) solid solution. According to X-ray analysis, the solubility limit for this system is around x=0.3 with the crystal symmetry (*Pmcn*) remaining the same as $Pb(Mg_{1/2}W_{1/2})O_3$. Dielectric analysis shows the increase of T_C with x. Polarization-electric field measurements show that the ceramics sintered at relatively low temperature (<1200 ˚C) still possess high dielectric breakdown field which makes it a possible candidate for dielectric capacitor material.

In the second part of **Chapter 4**, the other member of PMW-based solid solution, (1-x)$Pb(Mg_{1/2}W_{1/2})O_3$ - x$Pb(Mn_{1/2}W_{1/2})O_3$ will be introduced. Unlike the PMW-PZW system, replacing Mg^{2+} with Mn^{2+} leads to significant change in the crystal structure, physical and electric properties. This system is synthesized with solid state reaction method and characterized by X-ray diffraction, dielectric spectroscopy, scanning electron microscopy (SEM), atomic force microscopy (AFM), electron paramagnetic resonance spectroscopy (EPR) and superconducting quantum interference device (SQUID). It is found that with the increase of x up to 0.2, T_C of the solid solution is increased. When x>0.2, T_C starts to decrease and eventually the phase transition behavior vanishes.

1.8.3. $PbZrO_3$–$Pb(Mn_{1/2}W_{1/2})O_3$ Soft AntiferroelectricSolid Solution System

Chapter 5 of the thesis focuses on the $PbZrO_3$-based antiferroelectric materials. In this Chapter, the solid solution of the perovskite (1-x)$PbZrO_3$-x$Pb(Mn_{1/2}W_{1/2})O_3$ is introduced. The crystal structure, dielectric properties and antiferroelectric properties of compositions from x=0 to 0.1 are investigated by X-ray powder diffraction, dielectric spectroscopy and polarization-field analysis. It is found that the crystal structure of the solid solution remains in the orthorhombic *Pbam* symmetry with $x \leq 0.1$. The induced polarization (P_{Ind}) is improved whereas the critical field (E_{Cr}) is decreased with increasing x. The Curie temperature (T_C) is also decreased with the substitution of $Pb(Mn_{1/2}W_{1/2})O_3$for $PbZrO_3$. The magnetic properties are measured with SQUID, confirming that the Mn ion exists in a high spin state with 2+ oxidation state.

The discovery of ferroelectric phase in (1-x)$PbZrO_3$-x$Pb(Mn_{1/2}W_{1/2})O_3$antiferroelectric ceramics is also reported in Chapter 6. Dielectric spectroscopy, pyroelectric current measurements and high temperature X-ray diffraction method are used to verify the existence of the ferroelectric phase. From $x \geq 0.01$, a dielectric anomaly is observed as the result of antiferroelectric-ferroelectric phase transition slightly below the Curie temperature. High temperature P-E measurements show double hysteresis loop slightly above T_C as a typical feature of first order FE-PE phase transition. Pyroelectric current measurements carried out at different conditions confirmed the existence of ferroelectric phase which can be retained down to low temperature after removal of the external field. Structural analysis by high temperature x-ray diffraction method suggests a rhombohedral *R*3*m*symmetry for this ferroelectric phase.

In summary, the thesis divides in three parts: Chapter 3 for the synthesis and characterization of PIN-PMN-PT ferroelectric single crystal and ceramics; Chapter 4 for the synthesis and characterization of PMW-based antiferroelectric solid solutions and Chapter 5 for PZ-PMnW soft antiferroelectric ceramics.

Chapter 2: Material Characterization: Principle and Technique

2.1. Introduction

This chapter introduces the characterization techniques used in this work to interpret the structure and electrical properties of materials. Principles of X-ray diffraction, dielectric spectroscopy, hysteresis measurements and polarized light microscopy will be illustrated.

2.2. X-ray Diffraction

X-ray powder diffraction is used to perform structural analysis for crystalline materials. In this technique, X-ray radiation is produced by leading a beam of field-accelerated-electrons to hit a metal target. The incoming electrons eject electrons of the metal target into higher energy orbital. The vacancies can be created within the innermost K shell of the metal. Filling the vacancies in the K shell by electrons from outer L and M shells gives two intense radiations: K_{α} and K_{β}. In addition, different target materials provide X-rays with different wavelengths. For our XRD instruments, copper is used as target and the resulting Cu-$K_{\alpha 1}$ radiation with wavelength of 1.541Å is selected to demonstrate diffraction patterns[29]. Fig. 2.1 illustrates the interaction mechanism between x-ray and crystalline materials.

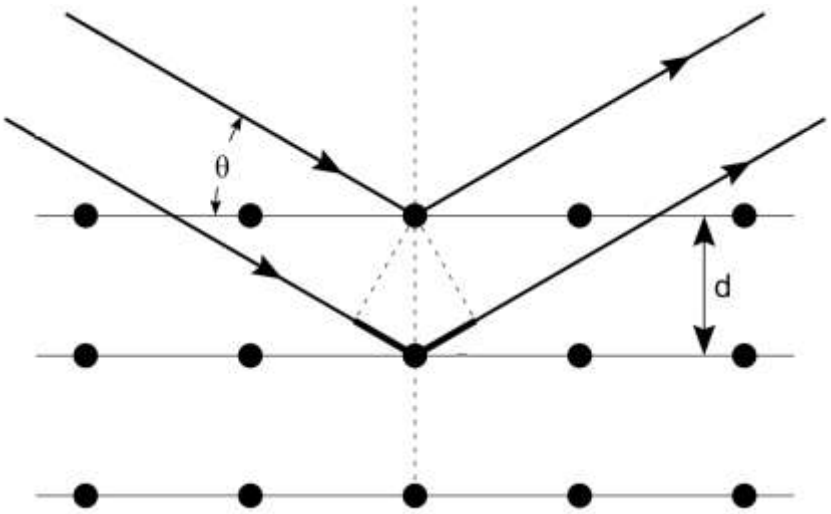

Figure 2.1 Illustration of diffraction of X-rays by a crystal

Incoming x-ray beams have a θ angle towards a certain crystal plane indexed as *hkl*. Diffraction can only be detected when the incident X-rays and the diffracted X-rays have a constructive interference with each other. Therefore, the path length difference between the diffracted X-rays and the incident X-rays is nλ, where n is an integer. Bragg's Law is shown below to describe this condition:

$$2d_{hkl}\,sin\,\theta = n\lambda, \tag{2.1}$$

where d_{hkl} is the distance between the planes indexed with (*hkl*); θ represents the angle between the incident beam and the *hkl* plane; λ is the wavelength of X-ray; n represents the order of diffraction. The *d*-spacing depends on the crystal symmetry, lattice parameters and Miller indices (*hkl*) for the choice of the plane. Fig. 2.2 shows the 6 lattice parameters used to describe the crystal symmetry of a unit cell. The schematic diffraction patterns for the major peaks are shown in Fig. 2.3. For example, the cubic unit cell has lattice parameters a = b = c, α = β = γ = 90˚. Therefore, 100, 110 and 111 diffraction planes all manifest in a single peaks. For a tetragonal unit cell with a = b ≠ c, α = β = γ = 90˚, 100 plane and 010 plane will diffract at the same θ angle which is different from 001 plane. Therefore, splitting of the 100 (and 200) peak can be observed for (a perovskite structure with) tetragonal symmetry. For a rhombohedral unit cell with a = b =

c, α = β = γ ≠ 90°, there is no splitting between 100, 010 and 001 peaks due to the equivalency in a, b and c. However, two distinguishable peaks can be seen for the $\{111\}_{pc}$ peaks due to the splitting between the 111 and $11\bar{1}$ peaks. Therefore, based on the peak position and peak splitting, symmetry elements can be deduced from the X-ray diffraction patterns.

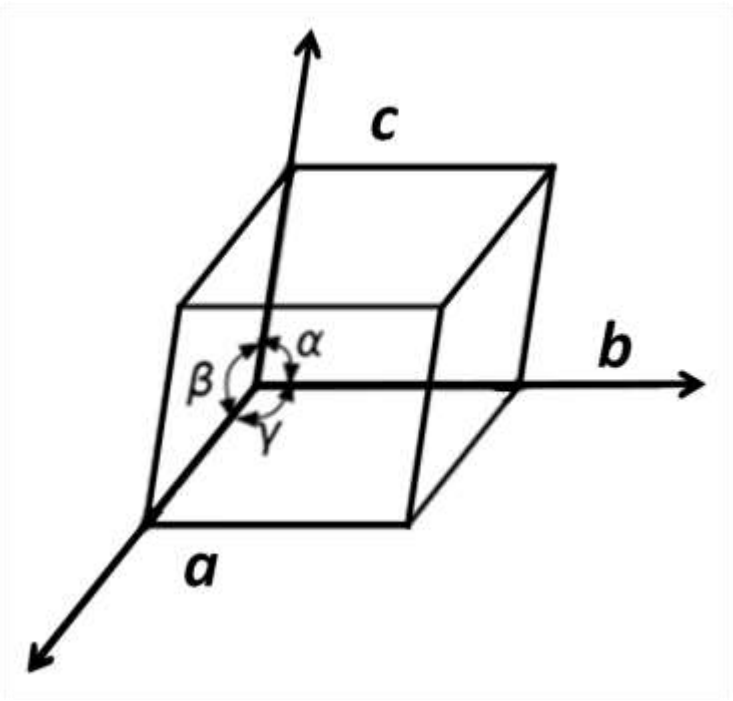

Figure 2.2 Demonstration of all lattice parameters within space-lattice

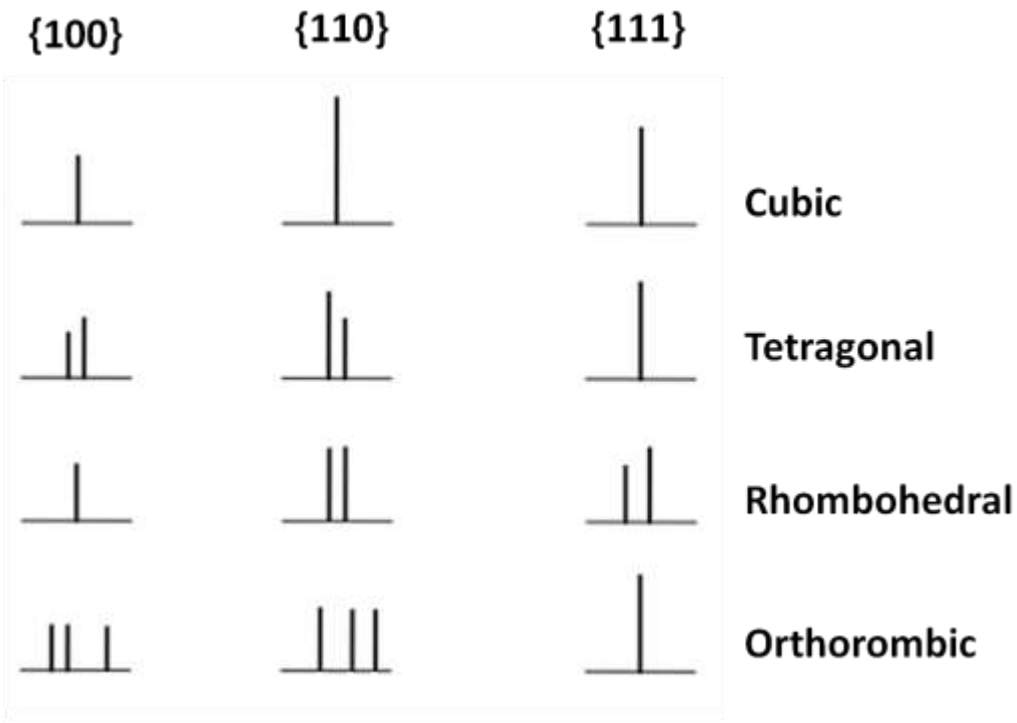

Figure 2.3 Schematics of the major XRD diffraction peaks for materials with different symmetries

2.3. Dielectric Spectroscopy

Dielectric spectroscopy measures various electrical properties with the change of frequencies and temperatures[30]. For ferroelectric and antiferroelectric materials, it provides the information of the change in polarization and phase transitions. In this work, dielectric spectroscopy measurements are conducted with a *Novocontrol* high-resolution broadband dielectric spectrometer. The schematic drawing of the circuit is shown in Fig. 2.4. The sample is made in the form of a parallel plate capacitor. Both surfaces of the sample are covered either by silver paste or gold as electrodes. The voltage is in the range from 1 to 3 V with the frequency varying between 1 Hz and 10^7 Hz. In this circuit, sample and reference are connected in series with two voltmeters measuring their voltage signals, respectively. Due to the serial connection between the sample and reference, the charge on the reference capacitor (Q_r) must be equal to the charge on the

sample capacitor (Q_s). Therefore the capacitance of the sample (C_s) can be calculated with the following equation:

$$C_s = \frac{Q}{V_s}, \tag{2.2}$$

where V_s is the voltages measured on the sample.

With the calculation of the C_s value, the dielectric permittivity can be determining the following equation:

$$C = \varepsilon_r \varepsilon_o \left(\frac{A}{d}\right), \tag{2.3}$$

where C is the capacitance; ε_r is the permittivity of the sample which we intended to calculate; ε_o is the permittivity of the vacuum; A is the area of the electrode plate; and d is the sample thickness.

As the external voltage applied to the circuit is time-dependent, the permittivity we obtain is therefore a complex number:

$$\varepsilon^* = \varepsilon' - i\varepsilon'', \tag{2.4}$$

where ε' and ε" are the real part and imaginary part of the permittivity, respectively; $i = \sqrt{-1}$.

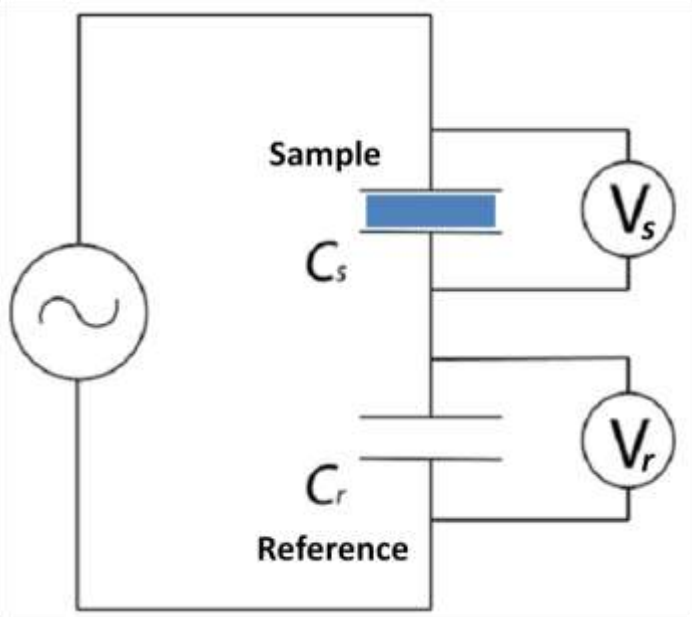

Figure 2.4 Schematic drawing of the circuit used in the dielectric spectroscopy

Dielectric loss is related to both the real and the imaginary part of the permittivity. It describes the dissipation of electromagnetic energy. The loss in dielectric material can be caused by the friction between polarization and electric dipoles. It is usually expressed in the loss tanδ as illustrated in the following equation and Fig. 2.5:

$$tan\,\delta = \frac{\varepsilon''}{\varepsilon\prime}\,, \tag{2.5}$$

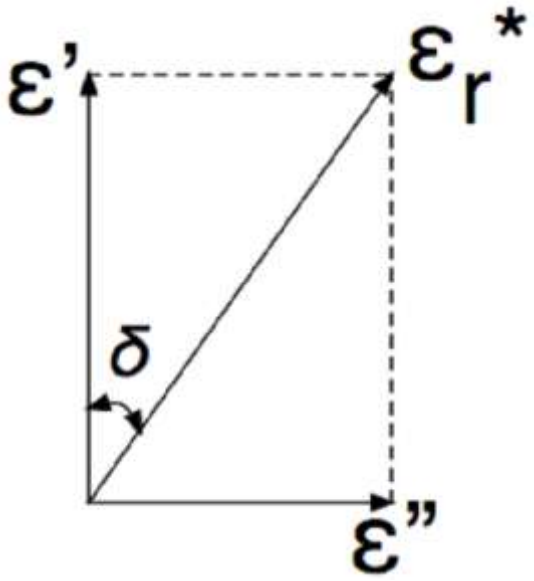

Figure 2.5 Illustration of the loss angle with respect to the real part and imaginary part of dielectric permittivity.

2.4. Polarized Light Microscopy

Polarized light microscope (PLM) is a powerful instrument used to determine the structural anisotropy in birefringent single crystals[31]. The instrument used in this work is an Olympus BX60 (Fig. 2.9) with a Linkam HTMS600 heating/cooling stage. The most important components of a PLM are a pair of polarizing filters.

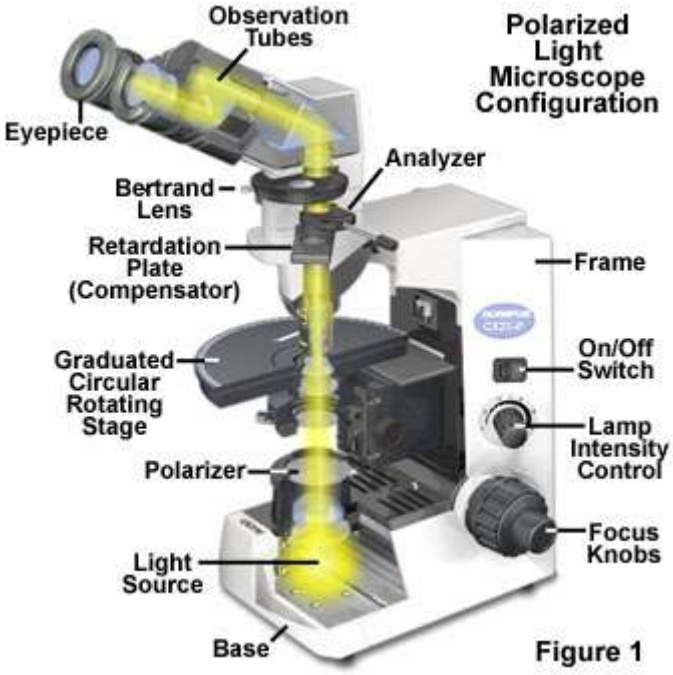

Figure 2.6 Basic Setup of polarized light microscope

As illustrated in Fig. 2.9, the polarizer (P) is located between light source and sample specimen; the analyzer (A), is located between the sample and eyepiece. In most of the cases, the polarizer and analyzer are placed perpendicular to each other so that no light can go through without additional interference, leaving a complete dark background. For uniaxial crystals with different refraction of index parallel to the sample plane, light entering the crystals is decomposed into two polarized rays, ordinary ray (*o*) and extraordinary ray (*e*). The ordinary ray with refraction index n_o has it polarization perpendicular to the optical axis whereas the extraordinary ray with refraction index n_e has it polarization parallel to the optical axis. Birefringence is therefore defined as the difference between the two corresponding indices of refraction:

$$\Delta n = |n_o - n_e| \ , \tag{2.6}$$

The birefringence value is obtained by PLM through the measurement of the retardation of the light with the following equation:

$$R = \ t \ \times \ \Delta n \ , \tag{2.7}$$

where *R* is the retardation, and *t* is the thickness of the crystal. When the crystal is placed between the crossed P and A with its optical axis lying at an angle θ to the polarizer, light will first decompose within the crystal into ordinary and extraordinary rays, as shown in Fig. 2.7.

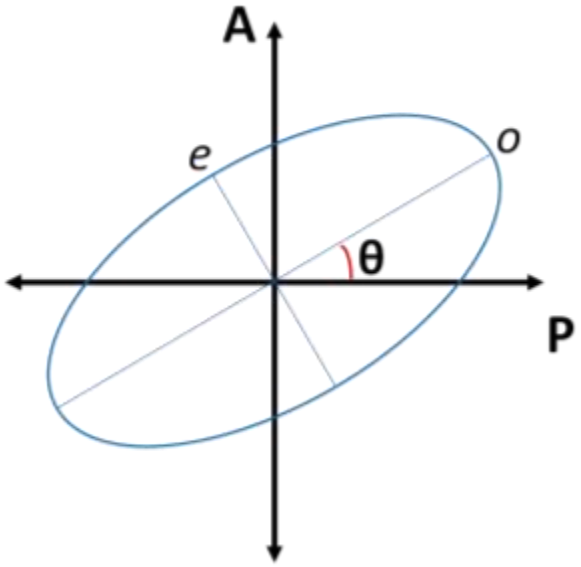

Figure 2.7 Schematic diagram of the decomposition and the recombination of a polarized light through a uniaxial crystal

The polarized light coming out of the polarizer (P) has its electric wave vibrating in the direction θ degree to the optical axis of the crystal. As the light passes through the crystal, it splits into two rays with the angle θ and 90 – θ degree respectively. Due to the difference in refraction of index, one ray will travel faster than the other. Therefore, the two rays are out of phase as they come out of the crystal and will recombine at the second polarizer (named as analyzer) (A). Interference of the two rays which are out of phase causes the retardation. The intensity of the light passing through the analyzer can be expressed as:

$$I = I_0 \cdot \mathrm{Sin}^2 2\alpha \cdot \mathrm{Sin}^2 \frac{\phi}{2}, \tag{2.8}$$

where I_0 is the intensity of the light passing through polarizer; Φ is the phase difference of the two rays given by:

$$\phi = (\frac{2\pi}{\lambda}) \cdot t \cdot \Delta n \ , \tag{2.9}$$

where λ is the wavelength of light; t is the thickness of the crystal and Δn is the birefringence of the crystal. When θ = 45°, maximum intensity of the interfered light can be reached. Similarly, zero intensity is reached when θ = 0° since the vibration direction of light has no partial component parallel to the direction of analyzer. The θ angle is therefore defined as the extinction angle. By examining the extinction angle of a crystal, the orientation of the crystal axis and the crystal symmetry can be determined. For example, rhombohedral crystals with the spontaneous polarization direction pointing along the {111} directions will show an extinction angle θ = 45°; tetragonal crystals with the spontaneous polarization direction pointing along the {001} directions will show extinction angle θ = 0 or 90°. The detailed information on extinction angles for different symmetries can be found in Fig. 2.8. For ferroelectric materials, spontaneous polarization only exists at below Curie temperature T_C. In most of the cases, if not experiencing phase transitions, the birefringence of a ferroelectric material will decreases with the increase of temperature. Above the T_C, the ferroelectric material becomes isotropic so that total extinction is observed at all positions under PLM. In some ferroelectric material with low symmetry, such as monoclinic or triclinic phases, both the magnitude and the direction of the spontaneous polarization are temperature dependent. Therefore, studying the birefringence and extinction angle with changing temperature will provide important information on crystal symmetry, and phase transition behaviour for ferroelectrics.

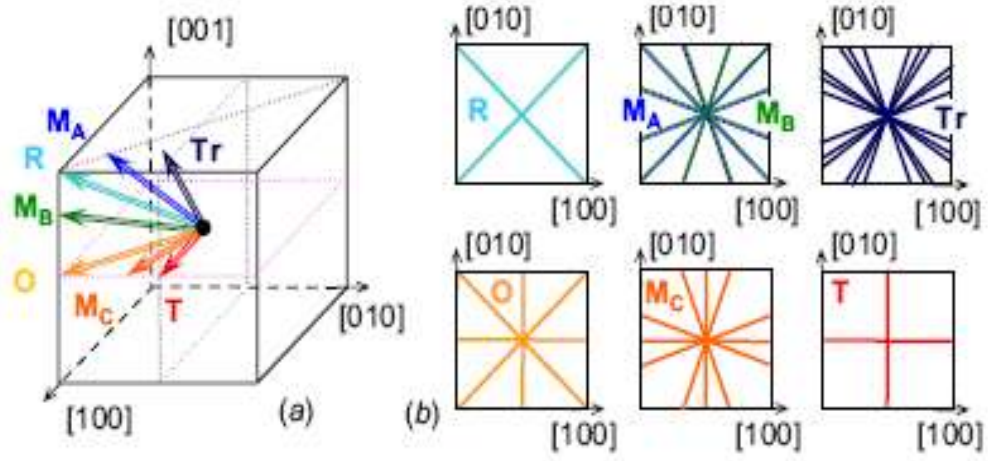

Figure 2.8 Extinction angles of (001)-cut perovskite ferroelectric crystals with different symmetries (Adapted from Ref 32)

2.5. Ferroelectric Hysteresis Measurement

The ferroelectric properties are characterized by the ferroelectric hysteresis polarization-electric field (P-E) loop. In this work, P-E loops are measured by an RT66A Standard Ferroelectric Testing System (Radiant Technologies Inc.). Fig. 2.9 shows a modified Sawyer-Tower circuit used to demonstrate the hysteresis loops[8]. The sample is prepared in the form of parallel plate capacitor. In Fig. 2.9, C_s is the capacitance of the sample; Rs is the resistance of the sample; C_r is the capacitance of the reference. An RC circuit is connected in the series with C_s in order to compensate the phase shift and leakage current from the sample. An AC voltage with triangle wave is applied to the sample.

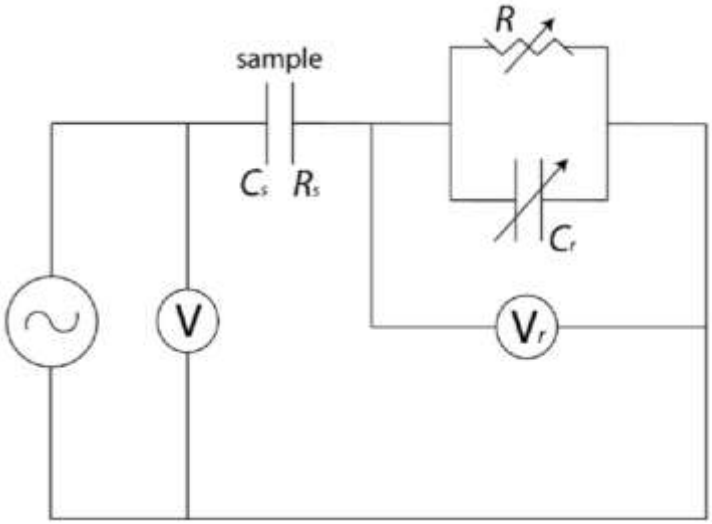

Figure 2.9 Schematic diagram of the modified Sawyer-Tower circuit for the P-E hysteresis loop measurement.

V_r measures the voltage across the reference capacitor C_r which is proportional to the polarization P of the sample according to the following relationship:

$$V_r = \frac{Q}{C_r} = \frac{A \times P}{C_r}, \tag{2.10}$$

in which Q is the charge on the reference capacitor, which is the same as the charge on the sample due to serial connection, A is the area of the electrode on the sample, and P is the polarization to be measured. The plot of polarization vs. electric filed is demonstrated as hysteresis loop with its physical meanings described in Section 1.3 (Page 3).

2.6. Piezoelectric Measurement System

The piezoelectric coefficient (d_{33}) is measured (Fig. 2.10) by a quasi-static piezoelectric meter (ZJ -6B, Institute of Acoustics, Chinese Academy of Sciences). Samples must be poled at high electric field in order to achieve the optimum alignment of the dipoles. As described in Section 1.2, the piezoelectric coefficient can be expressed as:

$$d_{33} = \frac{D_3}{X_3}, \tag{2.11}$$

where D_3 is the charge density generated on the z-direction of the sample in the unit of C/m^2; X_3represents the mechanical stress applied also in the z-direction in the unit of N/m^2.

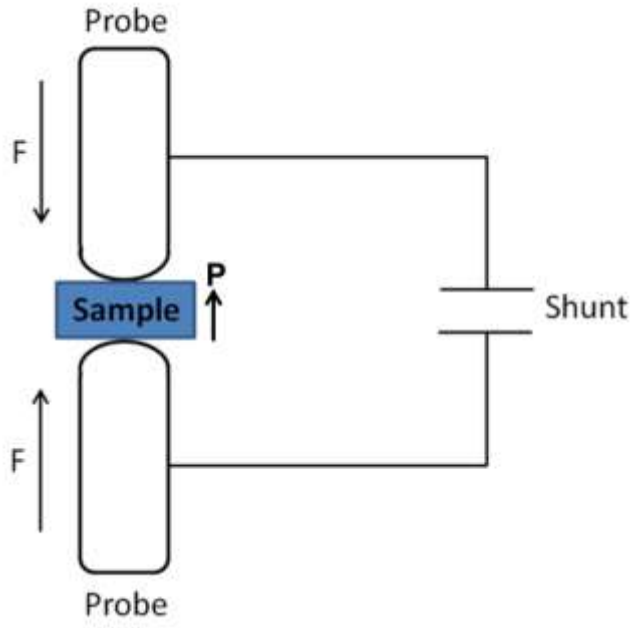

Figure 2.10 Schematic diagram for the measurement of piezoelectric coefficient by a quasi-static d_{33} meter

The electromechanical coupling factor *k* is calculated by a Solartron 1260 impedance analyzer in adjunction with a Solartron 1296 dielectric interface. The electromechanical coupling factor *k* measures the conversion efficiency between electrical energy and mechanical energy. There are different ways to calculate the *k* factor depending on the shape of the material. In most of the cases, piezoelectric ceramic and single crystals are prepared as thin disks and are poled in the direction perpendicular to the surface. When an AC field is applied to a poled piezoelectric material disc, radial vibration will occur and the planner coupling factor is expressed in the following equation:

$$k_p \cong \sqrt{\left(2.51 \times \frac{f_n - f_m}{f_n}\right) - \left(\frac{f_n - f_m}{f_n}\right)^2}, \quad (2.12)$$

where f_n is the maximum impedance frequency (or anti-resonance frequency) and f_m is the minimum impedance frequency (or resonance frequency). The disc vibrates most readily at the resonance frequency and therefore has the minimum impedance.

2.7. Scanning Electron Microscopy

Scanning electron microscopy (SEM) is a technique used in analyzing the microstructure of materials. In this work, material surface morphology visualization is carried out with Strata235 Dual beam SEM/FIB. In SEM, electron beam is excited from tungsten filament and is focused on the sample. When the incident electron beam hit the surface of sample, secondary electrons are emitted. Collecting the secondary electrons by the detector creates images of the sample surface (Fig. 2.11). In order to achieve the optimum image quality, samples are required to have conductive surface. Therefore, gold sputtering or graphite coating is usually applied to sample before SEM analysis. It is a powerful technique in analyzing ceramic material. Grains size can be measured and the growth direction can be revealed.

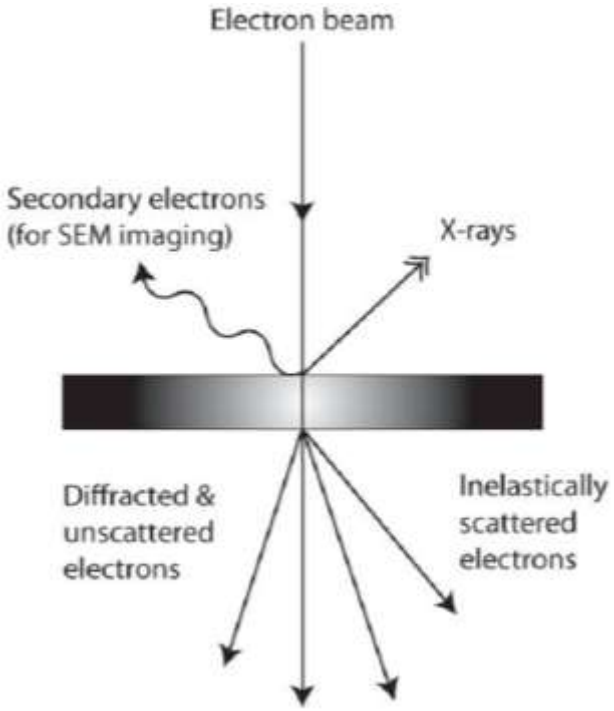

Figure 2.11 Schematic diagram of the working principle of SEM

Energy dispersive spectroscopy (EDS) is a technique used for quantitative elemental analysis. The principle of this technique is based on the fact that each element has its unique atomic structure and energy levels. For EDS experiment, as illustrated in Fig. 2.12, electron beam is focused onto the sample surface and the emission of characteristic X-rays from the sample is stimulated. Within the sample, electrons which existed in their ground state will be excited and ejected from the shell while creating an electron hole. An electron from outer higher energy shell will then fill the inner vacancy. Since the atomic energy levels are discrete, transfer of an electron from the higher energy level to the lower energy level can result in release of energy in the form of X-ray. The emitted X-rays from the sample can be detected by an energy-dispersive spectrometer. As different atom has its unique energy levels, the energy of the X-rays are also characteristic, which allows the elemental composition to be measured.

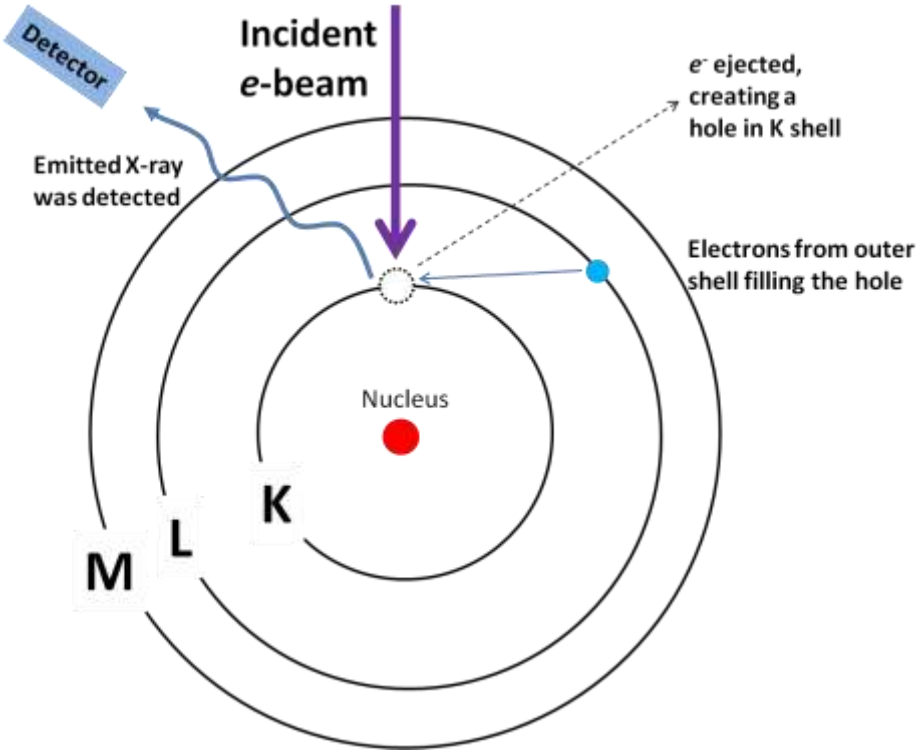

Figure 2.12 Schematic diagram demonstrating the principle of energy dispersive spectroscopy

Chapter 3: Synthesis and Characterization of Ternary $Pb(In_{1/2}Nb_{1/2})O_3$ - $Pb(Mg_{1/3}Nb_{2/3})O_3$ - $PbTiO_3$ Ferroelectric Single Crystals and Ceramics

3.1. Abstract

$xPb(In_{1/2}Nb_{1/2})O_3$-$yPb(Mg_{1/3}Nb_{2/3})O_3$-$zPbTiO_3$ (PIN-PMN-PT) single crystal with nominal composition x/y/z = 30/35/35 were grown via the flux growth method. Polarized light microscopy revealed that there is a large region of monoclinic M_C phase (~1 mm) in coexistence with rhombohedral (R) and tetragonal (T) phases in the single crystal, which is due to composition segregation. The M_C phase has three possible domain orientations which are distinguished by their unique extinction angles ($\pm\theta_M$ and 0° towards $[100]_{pc}$ axis). The phase transition from monoclinic M_C to cubic phase is at around 230 °C. Zero-field-heating dielectric measurements also reveal that the transition of rhombohedral phase into a low symmetry phase (possibly monoclinic M_A) occurs at around 80 °C. Based on the PIN-PMN-PT single crystals, a phase diagram around the morphotropic phase boundary (MPB) is proposed.

PIN-PMN-PT ceramics with compositions near the MPB region were synthesized in order to investigate the nature of the temperature-dependent phase transition of rhombohedral to monoclinic phase that was observed in the single crystal. With the increase in $PbTiO_3$ content, the phase transition sequence is from rhombohedral to monoclinic to tetragonal. Dielectric spectroscopy, along with high temperature X-ray diffraction and Rietveld refinement analysis shows the phase transition from rhombohedral (*R*3*m*) to monoclinic M_A (*Cm*) phase for PIN-PMN-PT 35/35/30 and

34/34/32. With this information, a pseudo-binary phase diagram is constructed for (1-x) $PIN_{0.5}PMN_{0.5}$-xPT system.

The low symmetry monoclinic structure found in the morphotropic phase boundary (MPB) region of ferroelectric solid solution is considered important for applications as well as for fundamental research. Conventionally, it is believed that for a thermodynamically stable phase, the electric-field/pressure/temperature-induced phase transitions should always be reversible, i.e. the structure of a crystal is mainly determined by its as-grown composition whereas field/pressure/temperature-induced strain shall be released when annealed above its Curie temperature. Here we report a novel phenomenon that after applying electric field on a PIN-PMN-PT single crystal, the original monoclinic M_C phase is transformed irreversibly into a tetragonal phase and cannot be restored to its original monoclinic phase after repeated high temperature treatments. With the help of polarized light microscopy, dielectric spectroscopy and thermal treatment under oxygen atmosphere, it is found that collective anisotropic migration of oxygen vacancies under an electric field is responsible for this irreversible phase transition phenomenon. Based on previous theoretical calculations and current experimental results[33], an oxygen-vacancy-migration model was proposed to explain this unusual behaviour.

The influence of the temperature driven rhombohedral (R) (*R*3*m*) → monoclinic (M_A) (*Cm*) phase transition on electrical properties is revealed at the end of this chapter. It is found that for single crystal, the rhombohedral domain is able to return to its original pattern after being annealed at above the rhombohedral-monoclinic phase transition temperature (T_{R-M}) but below Currie temperature (T_C). In ceramic system with similar composition, the piezoelectric constant also tends to be restored as the material is annealed at $T_{R-M}<T<T_C$. A polarization reversal model is proposed phenomenologically based on the polarization rotation theory

3.2. Introduction

$Pb(Mg_{1/3}Nb_{2/3})O_3$ (PMN) is a typical relaxor material that was first studied in 1960s[34]. However it was until 1980s that the PMN-based relaxor ferroelectric ceramics really begun to find their application as high-strain actuators and high energy capacitors due to

their high dielectric constant and piezoelectric response[35, 36].The most intensely studied PMN-based relaxor-ferroelectric material is $Pb(Mg_{1/3}Nb_{2/3})O_3$– $PbTiO_3$ (PMN-PT) in which PMN, a relaxor, forms a full solid solution with $PbTiO_3$ (PT) a typical ferroelectric,. Compositions of (1-x)PMN-xPT at $x < 0.20$ behave as a typical relaxor with a broad dielectric maxima at the phase transition temperature ($T_m < 100$ ˚C). As $PbTiO_3$ increases to $x \approx 0.28$, a ferroelectric phase is progressively induced with $T_C \geq 130$ ˚C. The best piezoelectric properties are found in the morphotropic phase boundary region (MPB) where $0.28 < x < 0.35$.

As mentioned in Chapter 1, the term MPB was first used by Jaffe *et al* to describe the boundary between the two phases in $Pb(Zr_{1-x}Ti_x)O_3$ (PZT)[37] in which the highest piezoelectric response was found. The origin of the MPB has been debated for decades. Previous work on PZT crystals suggests that the presence of MPB is a result of twinned rhombohedral and tetragonal nanodomains[38-40]. However, research on pure $PbTiO_3$ indicates that various symmetries as well as high electromechanical coupling effect can be generated by applying pressure[41]. So far, it is generally believed that the presence of MPB at room temperature requires the mixture of phases or the presence of lower symmetry phases in order to achieve a facilitated polarization rotation.

In the PMN-PT system, the end members PMN and PT possess rhombohedral and tetragonal symmetry respectively. It is discovered that within the MPB region of PMN-PT solid solution, a low symmetry monoclinic phase exists between the rhombohedral and tetragonal phases. Evidences of phase coexistence (R + M and T + M) were also found in the MPB compositions. The generation of low symmetry monoclinic phases were confirmed both in theory and in experiments. There are three subgroup of monoclinic phases, designated as M_A, M_B (*Cm*) and M_C (*Pm*)[42]. The M_A phase is considered as the bridge between rhombohedral and tetragonal phase since the spontaneous polarization of M_A phase is confined within {110} plane (Fig. 2.7). This role of bridge is also consistent with the polarization rotation theory proposed by Fu and Cohen[16]. Ye *et al* discovered the existence of the M_A phase in $0.65Pb(Mg_{1/3}Nb_{2/3})O_3$ - $0.35PbTiO_3$ system with the help of high-resolution synchrotron X-ray diffraction[15].

Monoclinic M_B phase shares the same space group (*Cm*) with monoclinic M_A. Its polarization is also confined within {110} plane but in a different direction (Fig. 2.7) and

can be treated as the bridge between rhombohedral (R) and orthorhombic (O) phase. Yao *et al*[43] reported the finding of a monoclinic M_B phase in $Pb(Zn_{1/3}Nb_{2/3})O_3$–4.5%$PbTiO_3$ (PZN-PT) single crystals by X-ray diffraction upon applying an electric field. The occurrence of the M_B phase was initially believed to be only induced by an external electric field. But Singh *et al*[44, 45] also observed stable M_B phase in PMN-PT system under ambient conditions.

The spontaneous polarization for the monoclinic M_C phase in perovskite ferroelectrics is along $\{100\}_{pc}$ plane as shown in Fig. 2.7. It acts as the bridge between orthorhombic (O) and tetragonal (T) phases. However, due to the similarity in structure and energy between orthorhombic and M_C phases, it is difficult to resolve these phases by conventional diffraction methods. Noheda *et al*[14] and Singh *et al*[46] reported their discovery of a stable Mc phase by X-ray diffraction in the MPB region of PMN-PT system, while Yoshiaki Uesu *et al*[47] reported a stable M_C phase in the PZN - 9%PT system. All the observations on M_A, M_B and M_C phases as well as the monoclinic phase related ferroelectric to ferroelectric phase transitions are currently consistent with the eighth-order expansion of the Landau-Ginsberg-Devonshire theory in Vanderbilt and Cohen's research[42]. In this chapter, detailed structural analysis on the low symmetry monoclinic phases is presented with the help of X-ray diffraction and polarized light microscopy.

In addition to the advantage in properties for single crystal material over polycrystalline materials, the diversity and feasibility of the crystal growth technique for relaxor-PT material also has its unique advantages over PZT. For PZT, the end members $PbZrO_3$ and $PbTiO_3$ are significantly different in melting temperatures. From its phase diagram[48], the temperature difference between the solidus and the liquidus lines are also very large, which leads to severe phase segregation during the crystallization process. In addition, multinucleation effects also hinders the growth of crystals due to the relatively high melting point of ZrO_2 (2715 °C). Therefore, the growth of commercially available PZT single crystals at MPB composition has not been successful so far because of the difficulty in controlling the segregation and multinucleation. In comparison, growth of relaxor-PT material such as PMN-PT, PZN-PT and PIN-PMN-PT has been widely applied for both industry and scientific research. High temperature solution (flux) growth uses PbO and B_2O_3 as solvent (flux) to lower the overall melting temperature and increase the solubility[49, 50]. Top seeded solution growth (TSSG) is a modified flux growth

method such that it introduces a seed crystal into the solution. The choice of seed can be different depending on the purpose of application. Seeds with {100} face are generally used[51]. The major advantage for the TSSG method is the additional control in crystal nucleation and propagation during the growth process. It provides a single nucleation site which can be monitored more readily than in flux growth. The Bridgeman growth method is used for production of relaxor-PT ferroelectric single crystals. Stoichiometric amounts of reactants are mixed and sealed in a Pt-crucible and melted at high temperature. The crystallization is achieved by slowly moving the crucible downward through a cooling zone. Relaxor-PT crystals, such as PMN–PT and PIN-PMN-PT are especially suitable for this technique because of their nature of congruent melting[52, 53].

Despite the high piezoelectric performance in PMN-PT or PZN-PT crystals, there still exist several major drawbacks which could potentially limit its application in electronic devices. For the PMN-PT system, the compositions in MPB region exhibit a ferroelectric rhombohedral to ferroelectric tetragonal phase transition around 80–90 ˚C which could potentially lead to the depoling of the material. The origin for such phase transition is due to the curved morphotropic phase boundary in the phase diagram separating the rhombohedral and the tetragonal areas. Previous research on PMN-PT single crystal also suggests that the presence of low symmetry monoclinic phase also plays important role in this phase transition. Another drawback of PMN-PT material is its relatively low coercive field (E_C = 2-3 kV/cm). The coercive field is the value of the threshold field required for polarization switching. A lower E_C will make the piezoelectric devices more susceptible to the environment with the presence of electric field. In order to compensate the drawbacks and to maintain the excellent piezoelectric properties, chemical modification on PMN-PT materials becomes necessary. In this work, $Pb(In_{1/2}Nb_{1/2})O_3$ (PIN) was used to tune the properties of PMN-PT system, forming $Pb(In_{1/2}Nb_{1/2})O_3$-$Pb(Mg_{1/3}Nb_{2/3})O_3$-$PbTiO_3$ (PIN-PMN-PT) ternary system. PIN is a typical relaxor ferroelectric material with T_m around 66 ˚C (at 1 kHz)[54]. It is worth to mention that PIN can also form solid solution with PT into (1-x)PIN-xPT binary system with a MPB separating the rhombohedral and tetragonal phases at x ≈ 0.37. According to previous researches, the PIN-PT ceramics with MPB composition has a high Curie temperature (T_C ≈ 320 ˚C) and a reasonable piezoelectric constant (d_{33} ≈ 400 pC/N)[54, 55]. With the

addition of PIN as the third component, the ternary PIN-PMN-PT complex perovskite system has been formed and has shown excellent ferroelectric properties. The major improvements compared to the PMN-PT system is the increased depoling temperatures in T_{RT} (90 – 120 ˚C) and T_C (160 – 320 ˚C) as well as the enhanced coercive field. The piezoelectric coefficient d_{33} can reach up to 550 pC/N for ceramics and 2200 pC/N for single crystals[56, 57]. Therefore, the excellent piezoelectric properties in PIN-PMN-PT system make it a promising candidate for a wide range of applications as electromechanical transducers and actuators.

3.3. Experiment

PIN-PMN-PT single crystals were synthesized by the high temperature solution flux growth method with the nominal composition of 30PIN-35PMN-35PT. Fine powders of PbO, In_2O_3, Nb_2O_5, MgO, and TiO_2 (>99 % purity) were used as starting materials. The metal oxides were melted at 1250 ˚C and cooled down at 1.0 ˚C/hr until the end of crystallization at 750 ˚C. Single crystal platelet were hand-polished with $(001)_{pc}$ plane to a thickness of <50 μm. Heat treatment was carried out on polished sample at 800 ˚C to release internal stress due to polishing. The PLM study was carried out on an Olympus BX 60 polarized light microscope equipped with Linkam THMS600 optical heating stage for high-temperature observations. After preliminary domain mapping by polarized light microscope, silver paste was deposited as electrodes on selected areas of the crystal for dielectric measurements which were performed using an alpha dielectric/impedance analyzer (*Novocontrol*). The electrodes were acid-washed after each dielectric measurement before new electrodes were deposited onto different areas. The crystal sample was carbon-coated to analyze the local composition using energy dispersive X-ray spectroscopy (EDX) on a Strata235 Dual beam SEM/FIB.

The PIN-PMN-PT ceramics with various compositions across the MPB region were prepared by a two-step solid state reaction method introduced by Swartz and Shrout[58]. The $InNbO_4$ and $MgMn_2O_6$ precursor phases were first synthesized from In_2O_3, Nb_2O_5 and MgO powders (purity >99%) at 1000˚C for 12 hours. This approach ensures the correct stoichiometric ratio of the B-site ions in the perovskite phase as well as suppresses the formation of the secondary phases such as $Pb_2Nb_2O_6$. In the second

step, the pre-formed precursors were mixed stoichiometrically with PbO, ground and calcined at 850 ˚C for 4 hours to obtain the powder of pure perovskite phase. An excess of 0.5-1% (mol percent) of PbO was added in this step to compensate the lead oxide evaporation at high sintering temperatures. The calcined sample was then ground into fine powder and pressed into pellets for sintering. The sintering process took place at temperatures varying from 1200 to 1260 °C for 2 to 2.5 hours, which led to dense ceramics. The dielectric constant was measured as a function of temperature from 0 to 300 ˚C at various frequencies by means of a *Novocontrol* broadband dielectric analyzer. X-ray powder diffraction was performed on a Rigaku diffractometer at room temperature. PANalytical X'Pert Pro MPD diffractometer with a curved Johansson monochromator producing Cu $K_{\alpha 1}$ (λ = 1.5405Å) radiation is also used with an Anton Paar HTK1200N furnace to heat the samples above room temperature at a rate of 0.5 ˚C/min. The Rietveld refinements were performed to analyze the crystal structure using the TOPAS-Academic software.

3.4. Results and Discussion

3.4.1. Domain Structure and Compositional Analysis in PIN-PMN-PT Single Crystals with MPB Composition

The PIN-PMN-PT 30/35/35 single crystal platelets with nominal composition of 30/35/35, were examined under polarized light microscope in three areas of different symmetries: rhombohedral (R), monoclinic (M_C), and tetragonal (T). The details will be discussed later in this section. Like in the PMN-PT system [53, 59], the PIN-PMN-PT ternary system has the same behavior of composition segregation during crystal growth[60]. The compositional segregation happens as a result of different crystallization temperature of each end member in the phase diagram. The composition segregation behavior will strongly affect the phase symmetry, domain structure and thereby piezoelectric properties [49, 53]. However, it also provides an opportunity to use this sample to map out a pseudo-binary phase diagram with respect to the increase in $PbTiO_3$ concentration by means of EDX with the contour of domains by PLM. In order to verify the composition variation, EDX measurements were performed in each of the 11 areas. It is found that in

this crystal, horizontally from position 1 to 6 [Fig. 3.1. (a)], Ti content significantly increases, whereas Mg, In, and Nb contents gradually decrease [Fig. 3.1. (b)]. In contrast, the measurement along the vertical line from position 7 to 11, show much reduced compositional fluctuation, as shown in Fig. 3.1(c). In particular, the Ti concentration almost remains constant

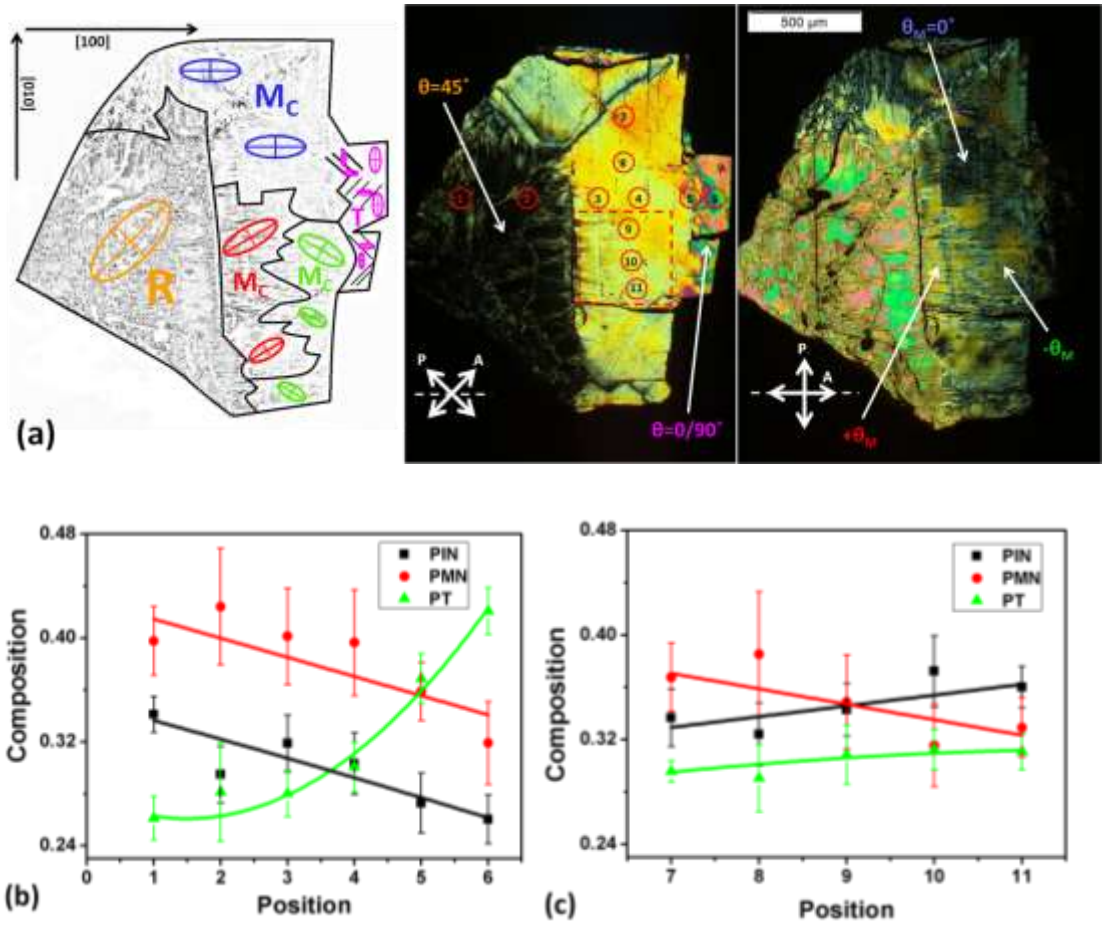

Figure 3.1 (a) Polarized light microscopy image of a $(001)_{pc}$ polished 30PIN-35PMN-35PT single crystal platelet with crossed polarizers positioned at 45° (left) and parallel (right) to the $<100>_{cub}$ crystallography axis. Composition variation analyzed using EDX are shown in (b) for positions 1 to 6 and (c) positions 7 to 11.

3.4.2. Study of Rhombohedral (R) → Monoclinic (M_A) Phase Transition

The Birefringence and extinction angle were measured simultaneously as a function of temperature using the polarized light microscope equipped with crossed polarizers for rhombohedral area between positions 1 and 2 (Fig. 3.1). It should be noted that in our experiment, only "effective birefringence" can be measured as the projection of actual birefringence on the $(001)_{pc}$ plane. The "temperature dependence of extinction angle" is shown in Fig. 3.2 (a). In the area labeled "R", upon the increase of temperature, the extinction angle remains 45° (towards the $[100]_{pc}$ axis) whereas the birefringence decreases until 80 °C. At 80 °C, both extinction angle and birefringence values drop sharply indicating a phase transition. With further increase of temperature, the extinction angle continues to decrease until the system undergoes another phase transition into the paraelectric cubic phase (~225 °C) where it becomes fully extinct in all directions under crossed polarizers. The first and the second phase transition temperatures are also consistent with the dielectric permittivity measurements on the rhombohedral area [Fig. 3.2 (b)]. The diffuse phase transition shown in the dielectric curves [Fig. 3.2 (b)] does not show any frequency dependence for the temperatures of the permittivity maxima. Thus the diffuseness of the dielectric peak does not indicate a relaxor behavior but just a diffuse phase transition possibly caused by partial B-site cation disorder.

The rhombohedral symmetry is assigned to the phase at T<80 ˚C based on its unchanged extinction angle (45 ˚) to $[100]_{cub}/[010]_{cub}$ direction. Upon heating, at T= 80 ˚C, the decrease in both extinction angle and birefringence value [Fig. 3.2 (a)] indicates that the R phase undergoes a first-order phase transition into a low symmetry phase. With the extinction angle $0<|\theta|<45$ ˚, it is possible for this phase to be monoclinic or triclinic phase. However, the analysis of the only one crystallographic orientation makes it difficult to determine the symmetry. Based on the theoretical approach [16, 61] as well as the previous experimental result on the PMN-PT system [62, 63], the rhombohedral phase with polarization oriented in the $[111]_{pc}$ direction is more likely to transform into a monoclinic M_A (*Cm*) phase with polarization lying in the $(110)_{pc}$ plane which allows the polarization to rotate away from $[111]_{pc}$ direction during the phase transition. On the other hand, to the best of our knowledge, direct transition from R to M_C phases has never been reported in any relaxor-PT solid solution systems. Therefore, the lower

symmetry phase is suggested to be monoclinic M_A phase which will be confirmed later on by further experiments on ceramics of the ternary system (Chapter 3.4.3).

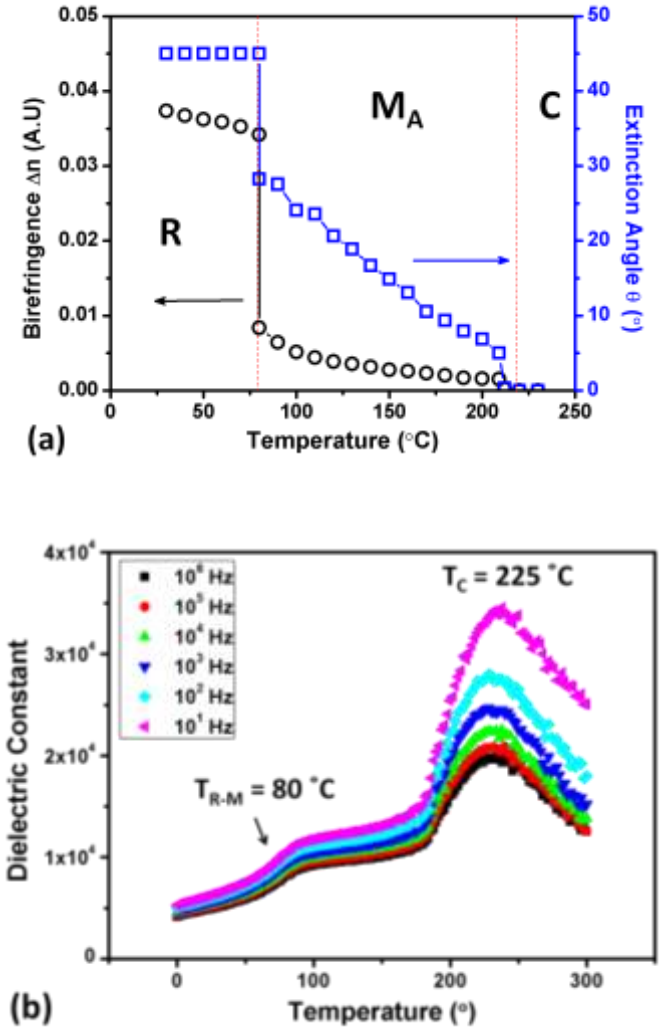

Figure 3.2 (a) Extinction angle and effective birefringence of the $(001)_{pc}$ platelet of 30PIN-35PMN-35PT single crystal measured by PLM for rhombohedral area upon heating. (b) Variation of the dielectric constant of the rhombohedral area as a function of temperature measured at different frequencies on heating

3.4.3. Study of the Ternary MPB on Ceramics

According to the study of Hosono *et al*[56], the MPB in the PIN-PMN-PT system lies a narrow region between the PIN/PMN/PT 63/0/37 and PIN/PMN/PT 0/68/32. With the information collected from the study of the single crystals, a series of solid solutions with compositions across the MPB region were prepared and systematically studied in order to resolve the MPB structure and to characterize the FE and dielectric properties. The compositions include PIN/PMN/PT = 36/36/28, 35/35/30, 34/34/32, 33/33/34, 32/32/36, 31/31/38 and 30/30/40, as shown by the black dots in Fig. 3.3, which indicate a constant ratio of PIN/PMN = 1, i.e. the pseudobinary line (1-z)($PIN_{0.5}PMN_{0.5}$)-zPT.

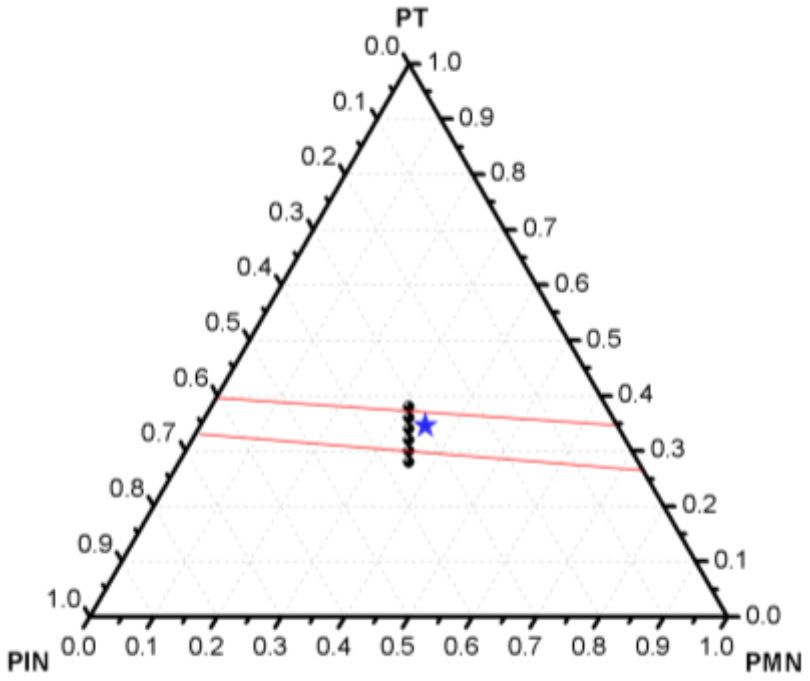

Figure 3.3 PIN-PMN-PT ternary phase diagram where red lines mark the estimated MPB region. The black dots indicate the compositions studied on the pseudobinary line (1-z)($PIN_{0.5}PMN_{0.5}$)-zPT. The blue star marks the nominal composition of the single crystal studied in Section 3.4.1.

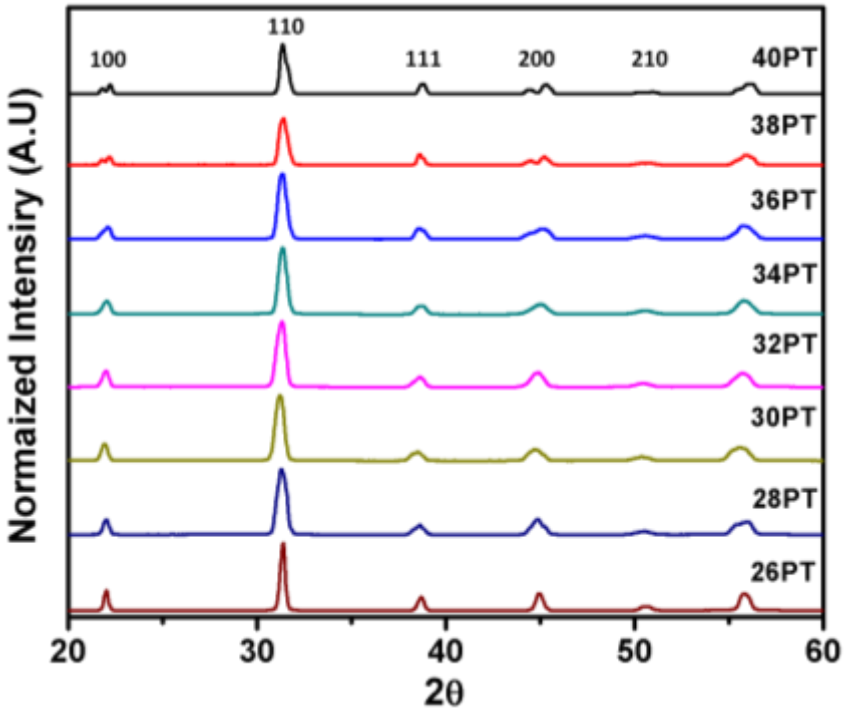

Figure 3.4 X-ray diffraction patterns for the pseudobinary (1-z)($PIN_{0.5}PMN_{0.5}$)-zPT ceramics with different PT contents at room temperature

Powder X-ray diffraction for the ceramic series (1-z)($PIN_{0.5}PMN_{0.5}$)-zPT (z = 0.28 – 0.4) was performed at room temperature on a Rigaku diffractometer using Cu K_{a1} and the diffraction patterns are shown in Fig. 3.4. All the compositions show perovksite structure without sign of any secondary phase. The evolution of the symmetry as a function of PT content can be seen as the $\{100\}_{pc}$ and $\{200\}_{pc}$ peaks transition from single peaks into multiple peaks and eventually into two peaks with 1:2 intensity ratio, the $\{111\}_{pc}$ peak also transitions from split peaks into a single peak, indicating a rhombohedral→monoclinic→tetragonal phase transition sequence. This sequence of phase transition is very similar to the PMN-PT binary system[64]. For MPB compositions (PIN-PMN-PT 35/35/30, 34/34/32, 33/33/34) where the split of $\{100\}_{pc}$ and $\{200\}_{pc}$ are observed, high resolution X-ray diffraction and Rietveld refinement were performed to resolve the possible presence of the low symmetry phases or the mixture of phases and the results are discussed later in this section (Fig. 3.6 and Fig. 3.7).

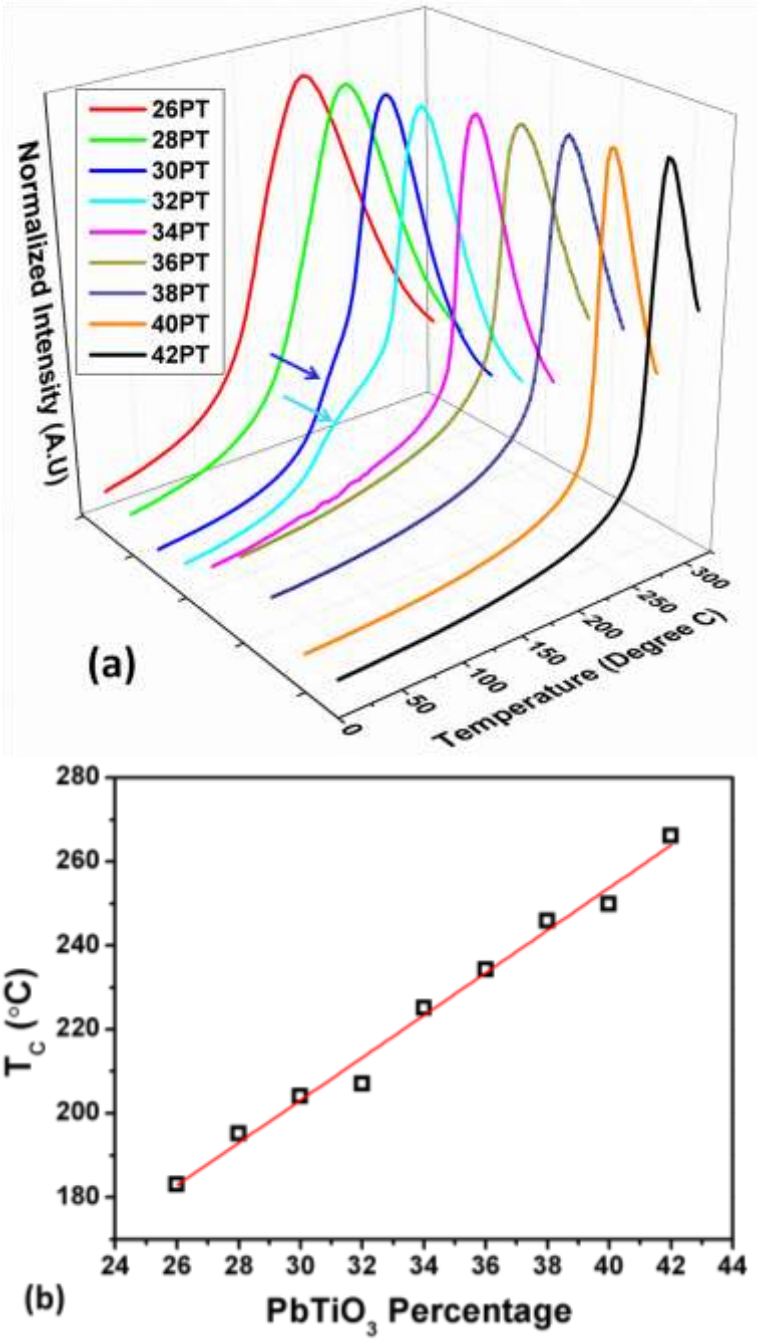

Figure 3.5 (a) Dielectric constant as a function of temperature of pseudobinary (1-z)($PIN_{0.5}PMN_{0.5}$)-zPT ceramics measured at10^5 Hz, and (b) the plot of ferroelectric Curie temperature T_C as a function of PT content.

The temperature dependence of the real part of permittivity (dielectric constant) of the PIN-PMN-PT ceramics is shown in Fig. 3.5. Only the data of 10^5 Hz are presented here since no frequency dispersion is observed. The dielectric spectra are normalized through dividing the dielectric constant values by the highest value in the corresponding curve in order to reveal the effects of composition. The major dielectric peaks indicate the ferroelectric (FE) to paraelectric phase (PE) transition at T_C. The ceramics with compositions PIN-PMN-PT 37/37/26 and 36/36/28 demonstrate a single ferroelectric (rhombohedral) to paraelectric (cubic) phase transition upon heating. The ceramics with compositions 35/35/30 and 34/34/32 undergo an additional FE – FE transition as revealed by the weak dielectric anomaly at $T < T_C$. For ceramics with PT content higher that 32%, a sharp peak of dielectric constant occurs, indicating a typical FE-PE transition. The T_C of this ceramic system shows increases with the increasing of PT percentage [Fig. 3.5 (b)]. The trend is consistent with the general expectation as $PbTiO_3$ has a much higher T_C (490 ˚C[65]) than $Pb(In_{1/2}Nb_{1/2})O_3$ (66 ˚C[54]) and $Pb(Mg_{1/3}Nb_{2/3})O_3$ (-60˚C[66]).

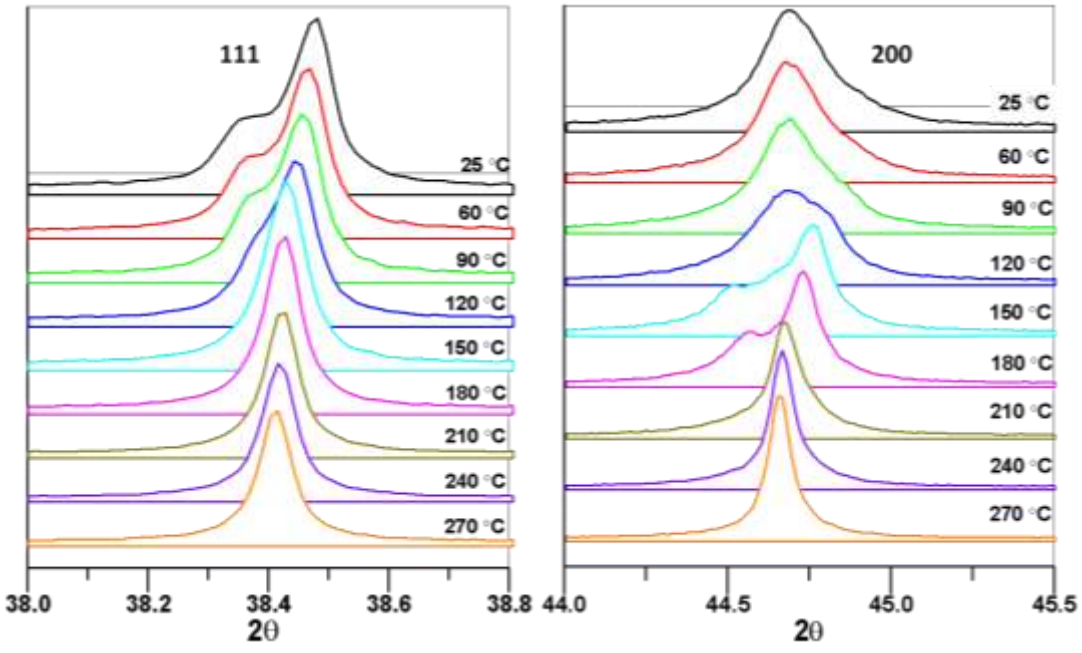

Figure 3.6 X-ray diffraction patterns of the $\{111\}_{pc}$ and $\{200\}_{pc}$ peaks of PIN-PMN-PT 35/35/30 measured at various temperatures upon heating.

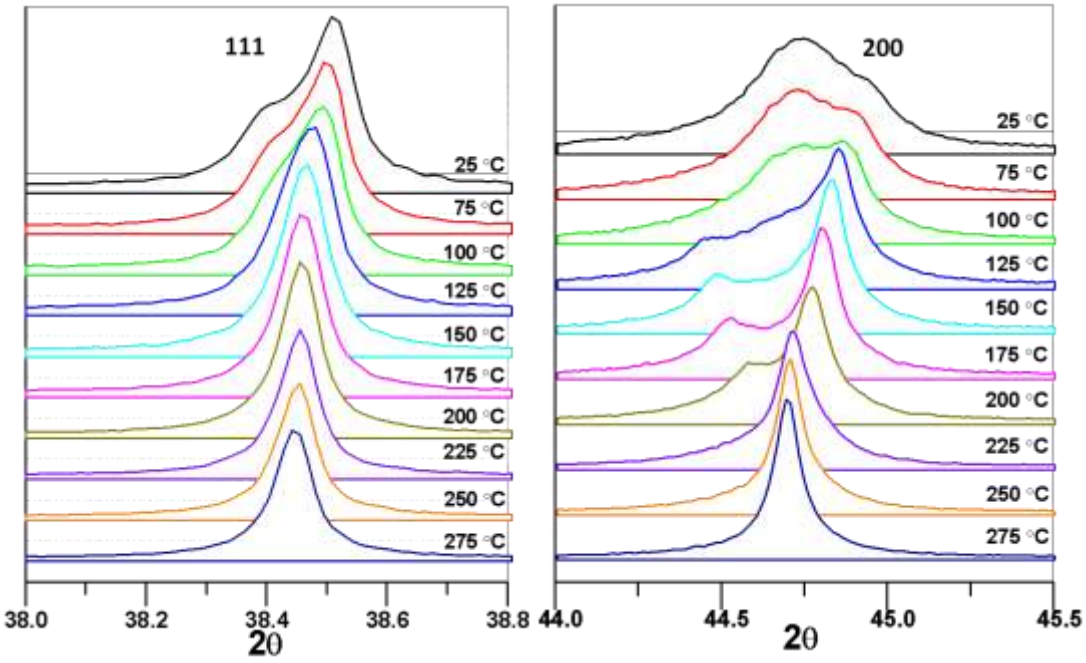

Figure 3.7 X-ray diffraction patterns of the $\{111\}_{pc}$ and $\{200\}_{pc}$ peaks of PIN-PMN-PT 34/34/32 measured at various temperatures upon heating.

In order to resolve the structure and the symmetry of the intermediate ferroelectric phase with the MPB composition of PIN-PMN-PT 35/35/30 and 34/34/32, high resolution XRD was performed on a PANalytical X'Pert Pro MPD diffractometer and the results are shown in Fig. 3.6 and Fig. 3.7, respectively. Both compositions show a mixture of a major rhombohedral phase and a minor unknown phase indicated by the skew and split of the $\{200\}_{pc}$ peak. This unknown phase is resolved to be monoclinic M_A with *Cm* space group later in this section. For PIN-PMN-PT 35/35/30 (Fig. 3.6), the splitting of the $\{111\}_{pc}$ peak gradually disappears upon heating up to150 ˚C, whereas the broadened$\{200\}_{pc}$ peak clearly split into two peaks as temperature increased above 120 ˚C, indicating the appearance of monoclinic M_A (*Cm*) phase until 210 ˚C. At higher temperature, both $\{111\}_{pc}$ and $\{200\}_{pc}$ peaks become singlet, indicating that the system enters a cubic phase. Similar phase transition behaviour is observed for PIN-PMN-PT 34/34/32 (Fig. 3.7) upon heating. It was commonly believed that this intermediate ferroelectric phase was tetragonal due to the splitting in the $\{200\}_{pc}$ peaks. However, our PLM study in Fig. 3.2 clearly shows that the rhombohedral phase in the area of MPB

composition undergoes a transition into a lower symmetry phase instead a tetragonal phase. Therefore, Rietveld refinements were performed based on the model of various low symmetry phases and mixed phases using the two diffraction patterns which lead to two possible solutions for the intermediate phase: monoclinic M_A (*Cm*) and M_C (*Pm*) symmetries. Table 3.1 compares the refinement results for the *Cm*, *Pm* and *P*4*mm* space groups for comparison. The best fit is found with the M_A phase in *Cm* space group with minimum difference between calculated pattern and experimental data. Under external influence, which could be electric field[16] or a chemical composition gradient as in our case, the polarization in rhombohedral phase can rotate from $\{111\}_{pc}$ direction to $\{001\}_{pc}$ direction via $\{110\}_{pc}$ plane which is also the plane the polarization of the M_A phase lies.

Table 3.1 Rietveld refinement results using various symmetries for the intermediate morphotropic ferroelectric phase in PIN-PMN-PT 34/34/32

Symmetry	R_{wp}	Goodness of Fit
Monoclinic M_A (*Cm*)	10.285	1.572
Monoclinic M_C (*Pm*)	11.228	1.716
Tetragonal (*P*4*mm*)	10.679	1.631

*Both R_{wp} (weighted profile R-factor) and Goodness of fit describe how well the calculated profile fit the observed data

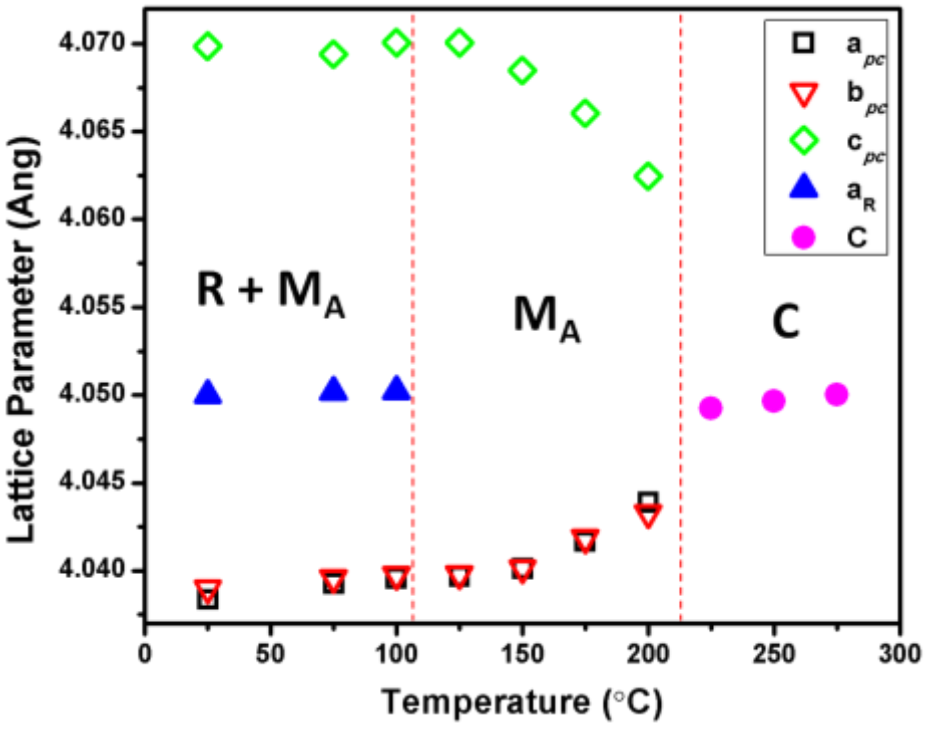

Figure 3.8 Variation of the lattice parameters calculated based on the temperature variable diffraction patterns of the PIN-PMN-PT 34/34/32 ceramic. Pseudocubic setting (pc) is used to describe the monoclinic M_A lattice

The temperature dependent lattice parameters calculated from the Rietveld refinements of the X-ray diffraction patterns are shown in Fig. 3.8. At room temperature, a mixture of rhombohedral phase with *R*3*m* symmetry and monoclinic phase with *Cm* symmetry is found to be present. The rhombohedral phase persists up to the rhombohedral→monoclinic transition temperature T_{R-M} = 100 ˚C at which it transformed into the monoclinic *Cm* phase. At T_C = 225 ˚C, the monoclinic *Cm* phase transforms into the cubic $Pm\bar{3}m$ phase, which is consistent with the dielectric measurements.

3.4.4. Verification of the Monoclinic M_C (Pm) Phase

After we verified the R→M_A phase transition, we now go back to the single crystal sample in Chapter 3.2 to verify the monoclinic M_C (*Pm*) phase observed by PLM. The middle part of the single crystal is enlarged in Fig. 3.9. It is marked as M_C phase in Fig. 3.1 (a) which is found to have three areas exhibiting different optical axis orientations at

room temperature, corresponding to the different domains of the M_C phase, as shown in Fig. 3.9 (a) (A, B and C, color coded with red, blue and green respectively). Observed on the $(001)_{pc}$ plane, area B shows parallel extinction, indicating the domain with one optical indicatrix axis perpendicular to (100) plane (blue indicatrix section). Areas A and C with $+\theta_M$ and $-\theta_M$ extinction angles, respectively, represent domains with the other optical axes lying within the $(100)_{pc}$ plane (red and green indicatrix section).

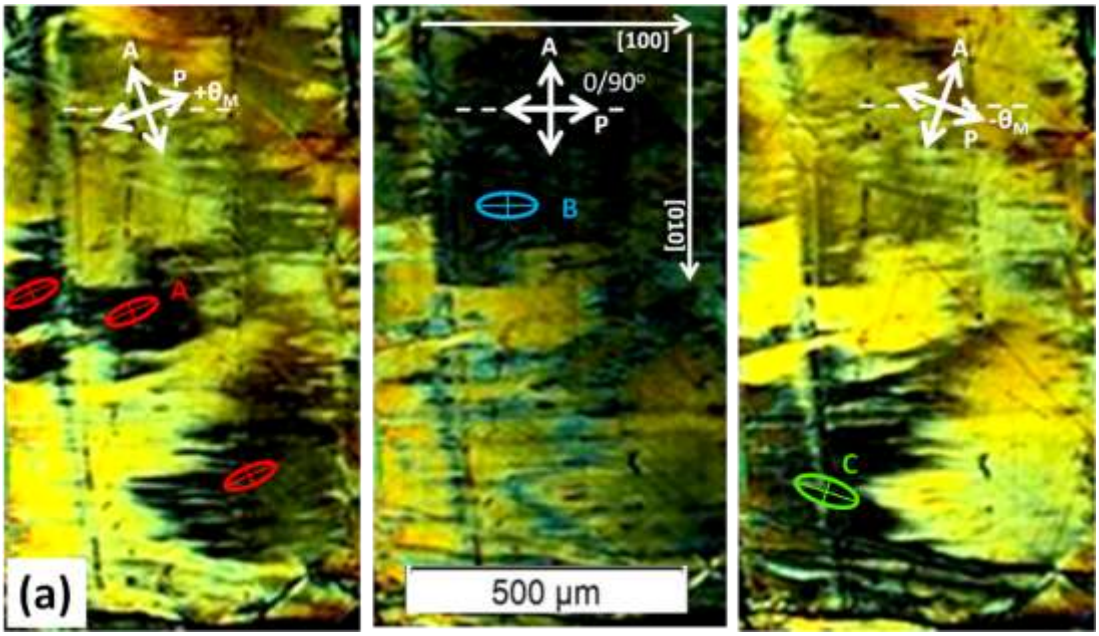

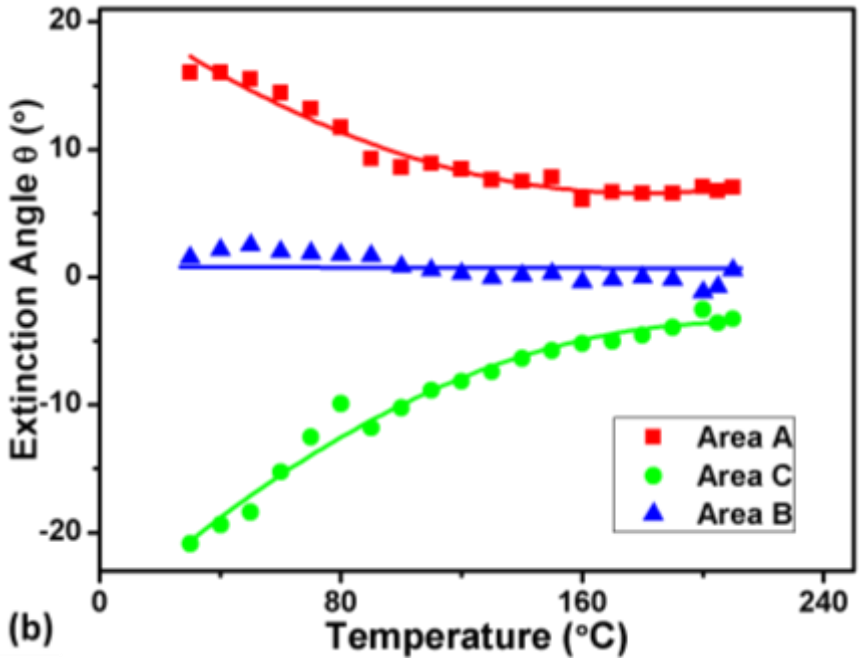

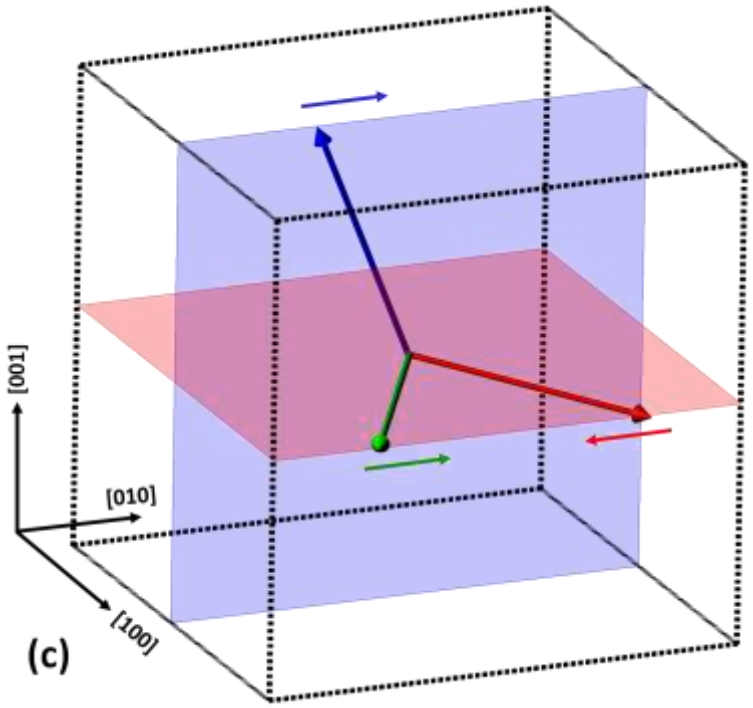

Figure 3.9 (a) Detailed PLM images of the rectangular area marked in Fig. 3.1 (a). Monoclinic M_C phase is observed in 3 areas: A, B and C with different domain orientations. Red, blue and green ellipses indicate the directions of the respective optical axes on the $(001)_{pc}$ plane. (b) Variation of extinction angle as a function of temperature for the three M_C domains. (c) Schematic diagram demonstrating the directions of polarization for the 3 domains of the M_C phase, and their rotation direction. Long arrows within the unit cell (red, green and blue) represent the directions of polarization corresponding to the domains labeled with the same color in (b). Short arrows represent the respective directions of polarization rotation.

Upon heating, the rotation of optical indicatrix is observed in all three M_C domains [Fig. 3.9 (b)]. The extinction angle at $\pm\theta_M$ in the area A and C varies with increasing temperature as shown in Fig. 3.9 (b) (the red and the green curves), indicating that their optical indicatrix lie in the $(001)_{pc}$ plane and rotate within this plane. For the domain that has its optical axis perpendicular to the $(100)_{pc}$ plane [0/90˚ extinction, Fig. 3.9 (a), area B], the optical indicatrix rotates within the $(100)_{pc}$ plane. Therefore, no change in the extinction angle for area B can be observed [Fig. 3.9 (b), blue curve].

In addition, the observation of domain structure by PLM upon heating shows that the three monoclinic M_C domains undergo the transition into the cubic phase at almost the

same Curie temperatures T_C = 230 ˚C. As shown in Fig. 3.10, upon the increase of temperature, the anisotropic birefringent FE domains transform into the isotropic PE phase as a straight line boundary crosses the crystal at around 230 ˚C. The thermodynamic stability for the monoclinic phase was confirmed by repeated annealing at 800 °C. Under such thermal treatment cycles, the sample is able to return to M_C phase with similar domain structure and extinction angles and only a slight shift in domain boundary.

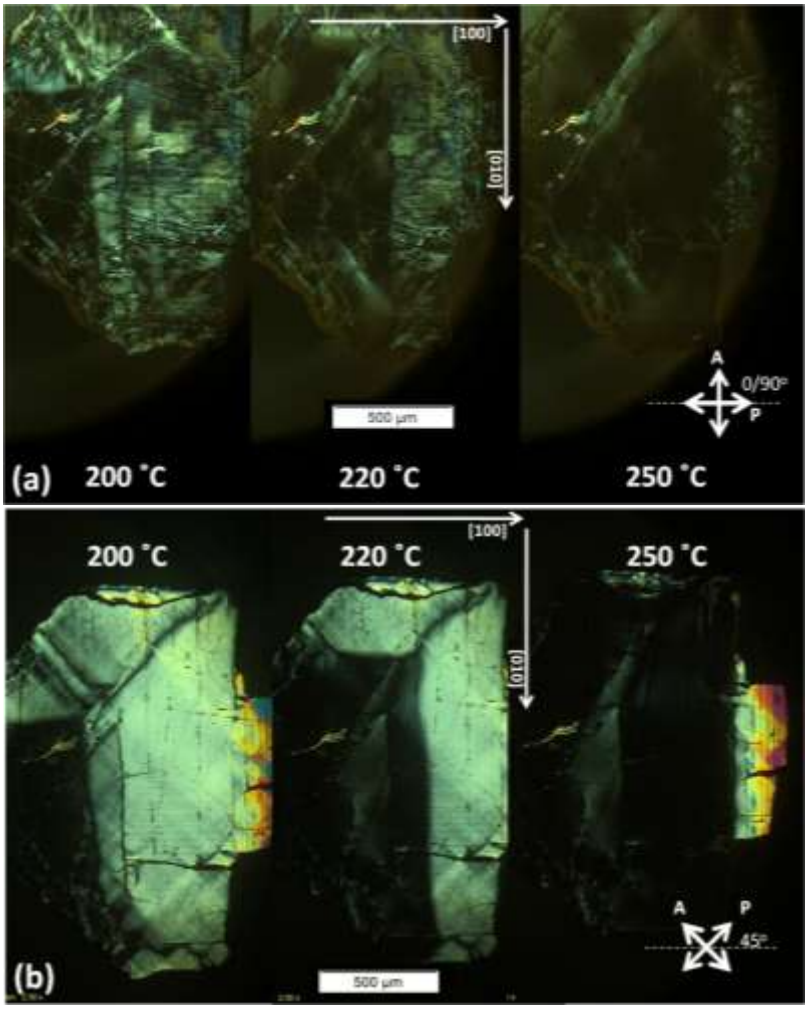

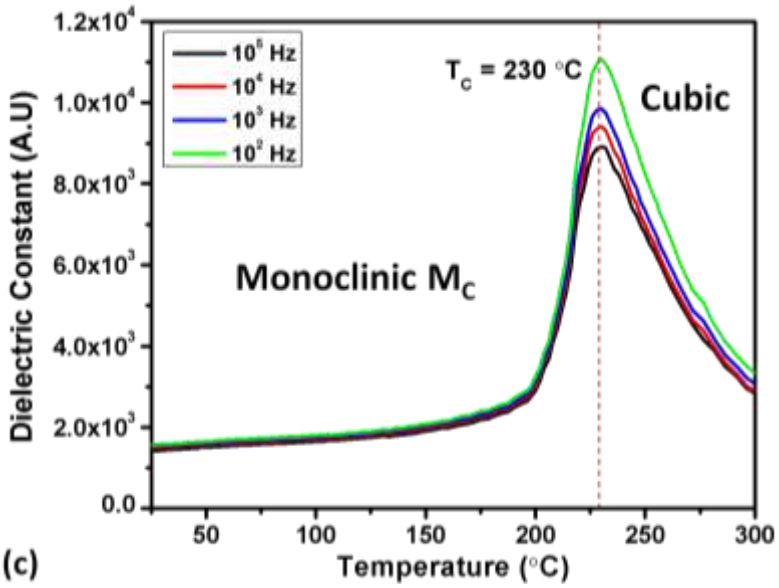

Figure 3.10 Monoclinic M_C to cubic phase transition observed on heating with the crossed polarizer/analyzer being (a) parallel/perpendicular, and (b) at 45° to the crystallographic $[100]_{pc}$ direction (c)Variation of the dielectric constant as a function of temperature (plotted in $\log_{10}$ scale) for the monoclinic area, showing the transition around T_C = 230 ˚C.

Upon heating, a direct M_C → C phase transition was observed with a clear optical anisotropic/isotropic phase boundary crossing over the crystal, indicating the first-order nature of the transition [Fig. 3.10 (a), (b)]. The dielectric measurement carried out on the M_C area of the crystal [Fig. 3.10 (c)] shows that upon heating, only one dielectric anomaly was observed, corresponding to the FE-PE phase transition at T_C. Therefore the result of dielectric measurement is consistent with the PLM observation and the M_C →C phase transition is the only transition taking place at T_C around 230 °C in the monoclinic M_C phase.

3.4.5. Phase Diagram near MPB

Based on the results obtained from single crystals as well as the R→M_A phase transition verified from ceramic system, we propose a composition-temperature phase diagram within the pseudobinary (1-z)(PINPMN)-zPT system using pseudobinary layout as shown in Fig. 3.11. For the single crystal sample, the presence of inherent Ti

compositional segregation from crystal growth suggests that the nature of the morphotropic phase boundary is very sensitive to "composition induced" effect and that lower symmetry monoclinic phases (M_A and M_C) serve as bridge in-between the end-member R and T phases. Interestingly, in the single crystal samples, the M_A phase is only observed at higher temperatures as a result of R→M_A phase transition, and no sign of M_A symmetry is found at room temperature whereas the coexistence of R and M_A phases is clearly resolved in ceramic systems by high resolution XRD. This discrepancy might result from slight compositional difference between the single crystal and ceramics. It could also be caused by intrinsic effects such as the different domain/grain structure and sizes between these two different forms of the material. Therefore, a shaded area is used in the phase diagram between the R and the M_A phases at around room temperature to indicate the character of mixed phases in that temperature – composition zone. Further experiment (with finer composition change interval) is needed to clarify the curved phase boundary separating R and M_A phases. The shape of the monoclinic regions is slightly different from the one for the PMN-PT system proposed by Singh *et al*.[44], or Shuvaeva *et al* [67], in terms of the boundary between the M_A and M_C phases. It is expected that the exact position of the M_A-M_C boundaries is hard to determine as it depend closely on the crystal growth conditions which can influence the composition and thereby the phase boundary. In addition, the lack of the observation in the clear composition-induced phase boundary between the M_C and T phases in the crystal [Fig. 3.1 (a)] may also be the result of a second-order phase transition nature, which is consistent with Vanderbilt and Cohen's phase diagram calculated from thermodynamics approach[61]. Although the M_C→T phase transition induced by composition[67], temperature[64, 68], electric field[63, 69] or stress[70] has been extensively reported in relaxor-PT binary systems, no evidence for a M_C→T phase transition has been observed in our experiments on ternary crystal or ceramics. Instead, a first-order M_C→C phase transition is observed, giving rise to a straight line up to cubic phase in the phase diagram for the M_C-T phase boundary. In terms of applications, although the piezoelectric properties of the monoclinic M_C phase are not as high as the MPB rhombohedral phase[71], its relatively high T_C and the absence of MPB FE-FE phase transition could extend the working temperature range of the electromechanical transducers.

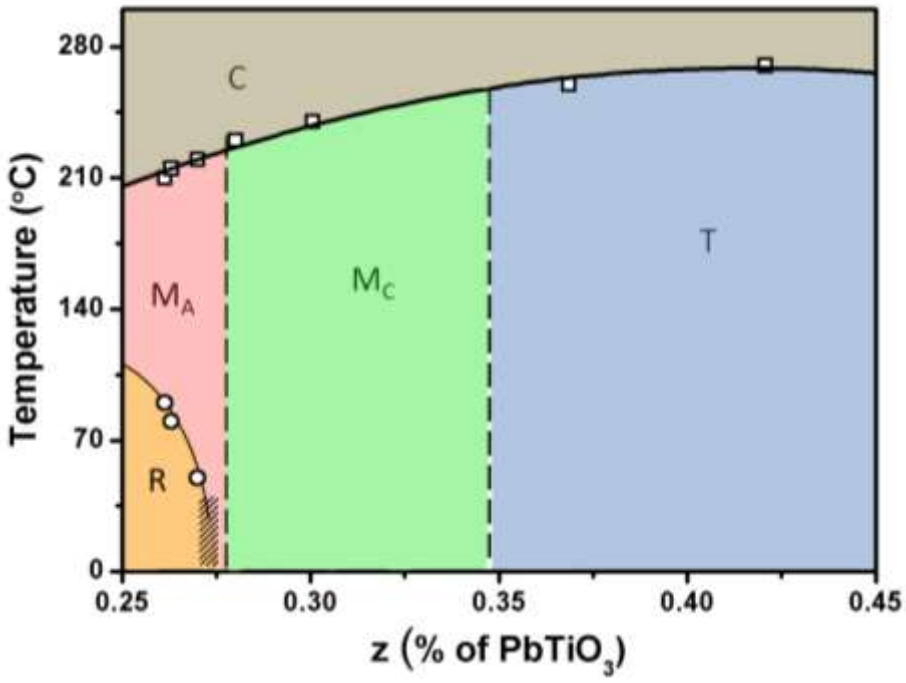

Figure 3.11 The proposed pseudo-binary phase diagram for the (1-z)(PINPMN)-zPT based on PLM measurement of single crystal, showing the symmetries of the different phases; shaded area represent the mixture of R and M_A phases; dashed lines indicate the boundaries where morphotropic phase transitions may take place.

3.4.6. Study of the irreversible Monoclinic M_C → T phase transition

Perovskite ferroelectrics have been recognized as the excellent material for piezoelectric applications. Relaxor-PT solid solution system represented by $Pb(Mg_{1/3}Nb_{2/3})O_3$-$PbTiO_3$ (PMN-PT) (Generation I) and PIN-PMN-PT (Generation II) are considered as a promising piezo-/ferroelectric materials. Single crystals of such materials have significant advantages over conventional ceramics due to their large ferroelectric domain which is responsible for high piezoelectric constant, polarization saturation and field-induced strain. Application of electric field reorients the dipoles and therefore creates a net polarization. In addition, oxygen vacancies are also commonly present in perovskite as charge carriers. Most of the research focused on its role in domain pinning effect which leads to high coercive field and mechanical quality factor[72, 73]. In this paper, it is found that oxygen vacancies can affect the crystal symmetry and domain structure under the application of an electric field. The underlying mechanism is discussed next.

Polarized light microscopy (PLM) has unique advantages in imaging the domain structure and identifying the crystal symmetry of optically anisotropic materials such as the monoclinic phase in this case. Since its discovery by Noheda *et al*. in $Pb(Zn_{1/3}Nb_{2/3})O_3$-$PbTiO_3$ (PZN-PT) solid solution system[69], monoclinic M_C (*Pm*) phase has been widely studied due to its close connection to the excellent piezoelectric properties in MPB[64]. It has also been found in $Pb(Mg_{1/3}Nb_{2/3})O_3$-$PbTiO_3$ (PMN-PT)[64, 74, 75] and $Pb(Zn_{1/3}Nb_{2/3})O_3$-$PbTiO_3$ (PZN-PT) systems[69] by diffraction and optical methods. It is believed that the presence and behavior of the M_C phase significantly plays an important role in the crystal's enhanced piezoelectric properties[71]. With its polarization capable of rotating within the $\{100\}_{pc}$ planes (pseudocubic notation is used throughout this work), the M_C phase can act as a "bridge" between the orthorhombic (O) phase (with polarization oriented in the $[011]_{pc}$ direction) and the tetragonal (T) phase (with polarization oriented along the $[001]_{pc}$ direction) phases[16]. In some literatures, the M_C phase was also described as a "metastable" phase as it can be induced as a distortion of high symmetry phases by external field or stress [69, 76-78]. From a symmetry point of view, being a subgroup of both the O (*Amm*2) and T (*P*4*mm*), the M_C (*Pm*) phase is also allowed to take second order phase transition into either the O or T phase. Vanderbilt and Cohen's theoretic phase diagram[61] built by means of high order of Devonshire theory points out that there is a triple point where M_C, T and O phases are at equilibrium. Therefore it is reasonable to believe that small perturbations in composition, temperature, electric field, pressure, etc, could break the equilibrium and lead to the phase transition between any two of these three phases. From a crystal chemistry point of view, structural defects such as oxygen vacancies are known to be inherently present in perovskite oxides compound[79]. However, their effect on the macroscopic crystal symmetry has have been poorly documented and understood. In this section, we have studied the field induced irreversible $M_C \rightarrow T$ phase transition in a ternary piezoelectric crystal and found that the presence of oxygen vacancies and their movement under electric field are the underlying mechanism for such an unusual phenomenon.

The growth and characterization of the PIN-PMN-PT 30/35/35 single crystals w were reported in Chapter 3.1. In this section, the polished $(001)_{pc}$ oriented crystal samples were annealed at 800°C for 4 hours in sealed crucibles to make sure that all the observed phases are thermodynamically stable and to release any induced internal-

stress. The monoclinic M_C phase is identified by optical crystallography and polarized light microscopy (PLM) based on its unique extinction angles determined on the domain structure [Fig. 3.9 (a)].

With the M_C domain determined, silver paste was deposited onto the area covering all three M_C domains as electrodes. A DC electric field of 20kV/cm was then applied along the $[001]_{pc}$ direction at room temperature for 5 minutes to ensure a complete domain switching. After poling, the silver paste electrodes were then washed off by acetone for optical examination by PLM. It is found that, after poling, the multidomain M_C phase transformed into a large homogeneous single domain with extinction at any angle under crossed polarizers, indicating the formation of a new phase (Fig. 3.12). From its extinction feature, it is deduced that this electric-field-induced new phase is of tetragonal symmetry with its optical axis perpendicular to the $[001]_{pc}$ plane and it appears to be a single domain. Upon heating up to the Curie temperature T_C, it is observed that the T_C in the poled area transforms into the cubic phase at almost the same temperature as the unpoled crystal. However, the boundary between the ferroelectric and paraelectric phases during the phase transition is slightly different in the poled and unpoled crystal as marked by red arrows in Fig. 3.13. In contrast to the unpoled crystal, the sharp boundary appears between the isotropic and the anisotropic phases in the poled crystal, indicating the vertical phase boundary in the poled crystal compared to the inclined phase boundary in the unpoled crystal.

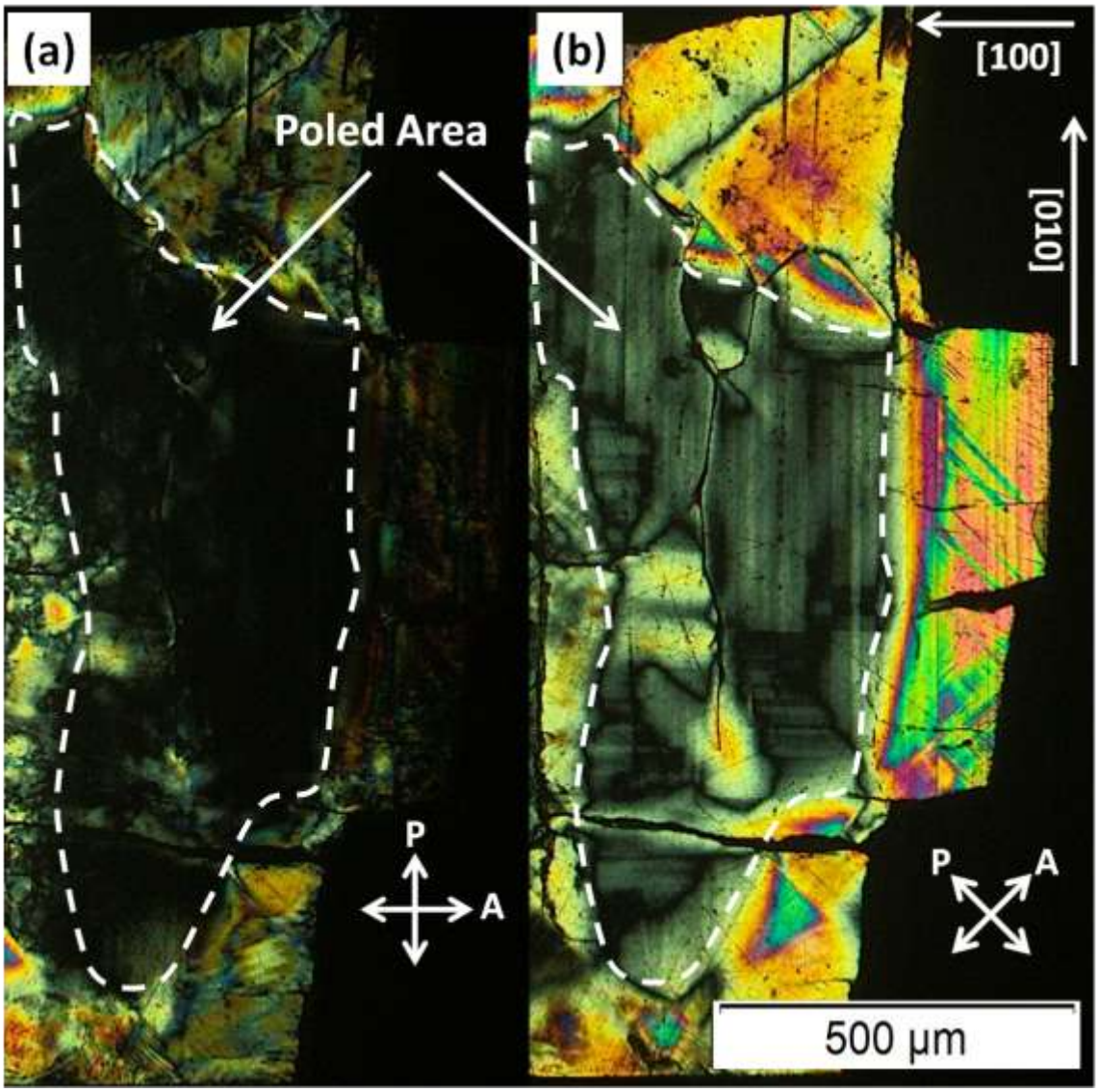

Figure 3.12 PLM images of $[001]_{pc}$ poled PIN-PMN-PT crystal with $[100]/[010]_{pc}$ orientation at (a) 0^{o} and (b) 45 ˚ to the crossed-polarizer. The vertical and horizontal stripes were found to be growth striation that does not disappear above T_C.

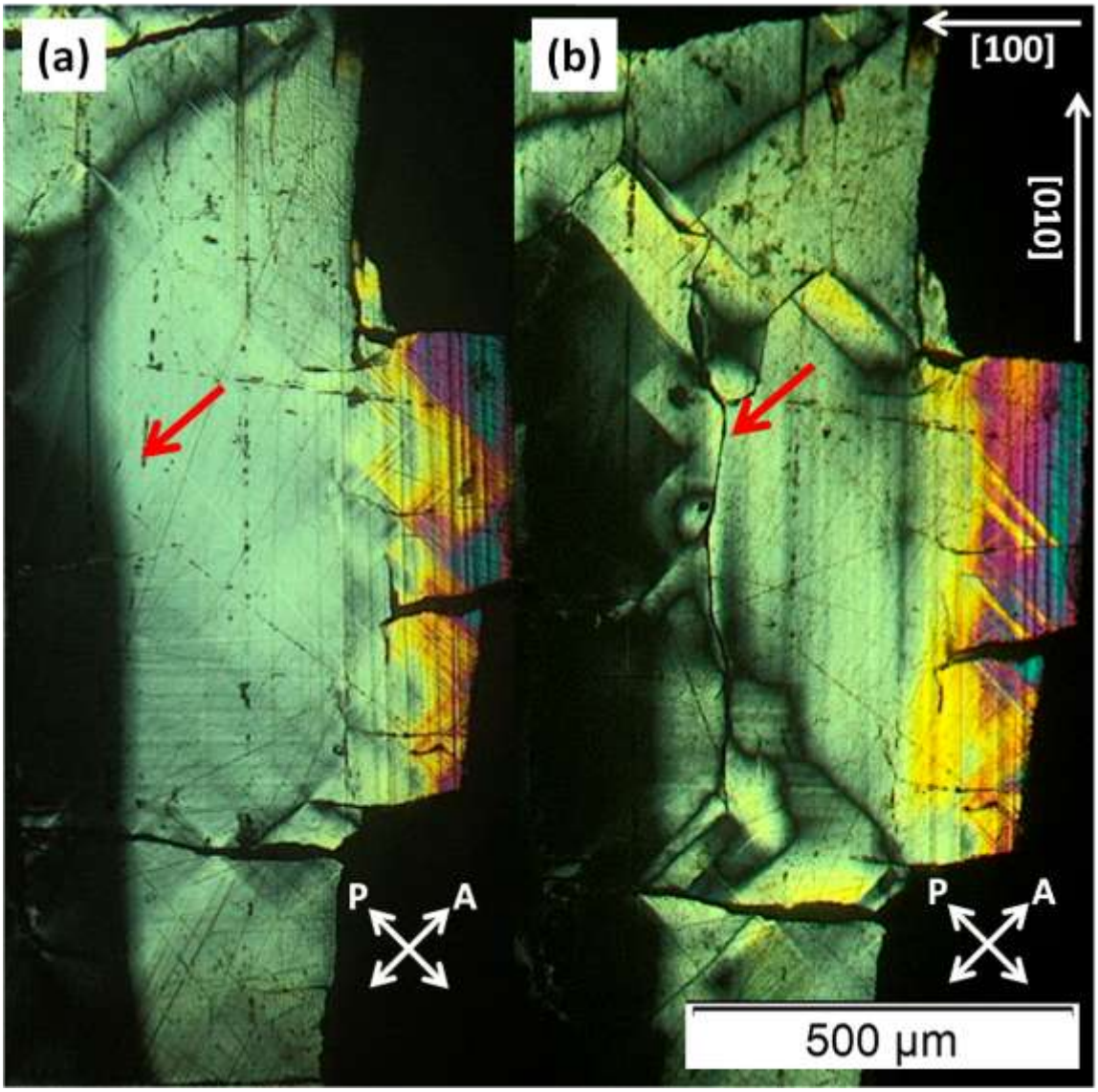

Figure 3.13 Zero-Field-Heating of the unpoled (a) and poled (b) crystal up to near T_C (220 °C). Both images are taken with crossed polarizers at 45 ˚ to the $[100]/[010]_{pc}$ directions. Red arrows point to the isotropic—anisotropic phase boundaries.

In the case of a field induced phase transition, normally after annealing the crystal above the Curie temperature T_C, the original phase would restore upon the subsequent zero field cooling down to room temperature. However, to our surprise, repeated annealing of the poled crystal in sealed alumina crucible at 800 °C does not result in full restoration of the monoclinic M_C phase. Instead, the crystal remained in tetragonal phase with clear 90

˚ domain structure as shown in Fig. 3.13 (a), indicating that such an induced tetragonal phase is thermodynamically stable and has permanently replaced the monoclinic phase. Therefore, the electric-field induced monoclinic→tetragonal phase transition is an irreversible process. To the best of our knowledge, such irreversible phase transitions are rather unusual and have not been documented clearly except for the case in which the irreversible $R \rightarrow M_A \rightarrow M_C$ phase transition was discovered in PZN-PT system under the influence of the electric field by diffraction methods[80]. Analysis of the enlarged view of the domain structure in the inset of Fig. 3.13 (a) reveals that the optical indicatrix sections between the neighbor domains lies perpendicular to each other. In addition, the domain walls are oriented 45° to the $[100]_{pc}$ and $[010]_{pc}$ directions, which is consistent with the typical layout of tetragonal 90 ˚ domains arising from mechanical and electrical compatibility confirming the tetragonal symmetry. The development of the tetragonal 90 ˚ domains with polarization lying within the $\{100\}_{pc}$ planes, as observed in Fig. 3.14 (a) (inset), can be understood from the fact that this domain configuration is aligned perpendicular to the [001] surface of the crystal after poling.

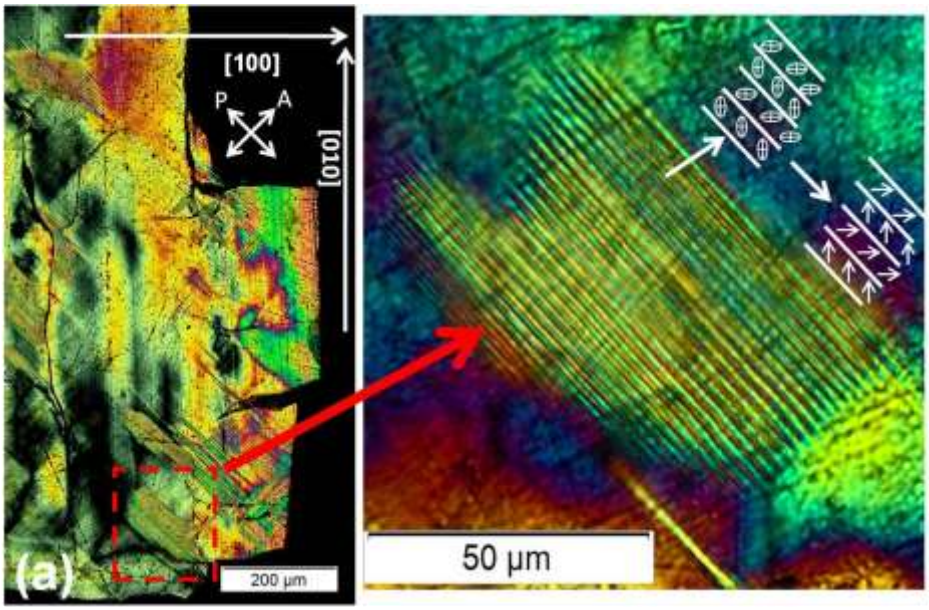

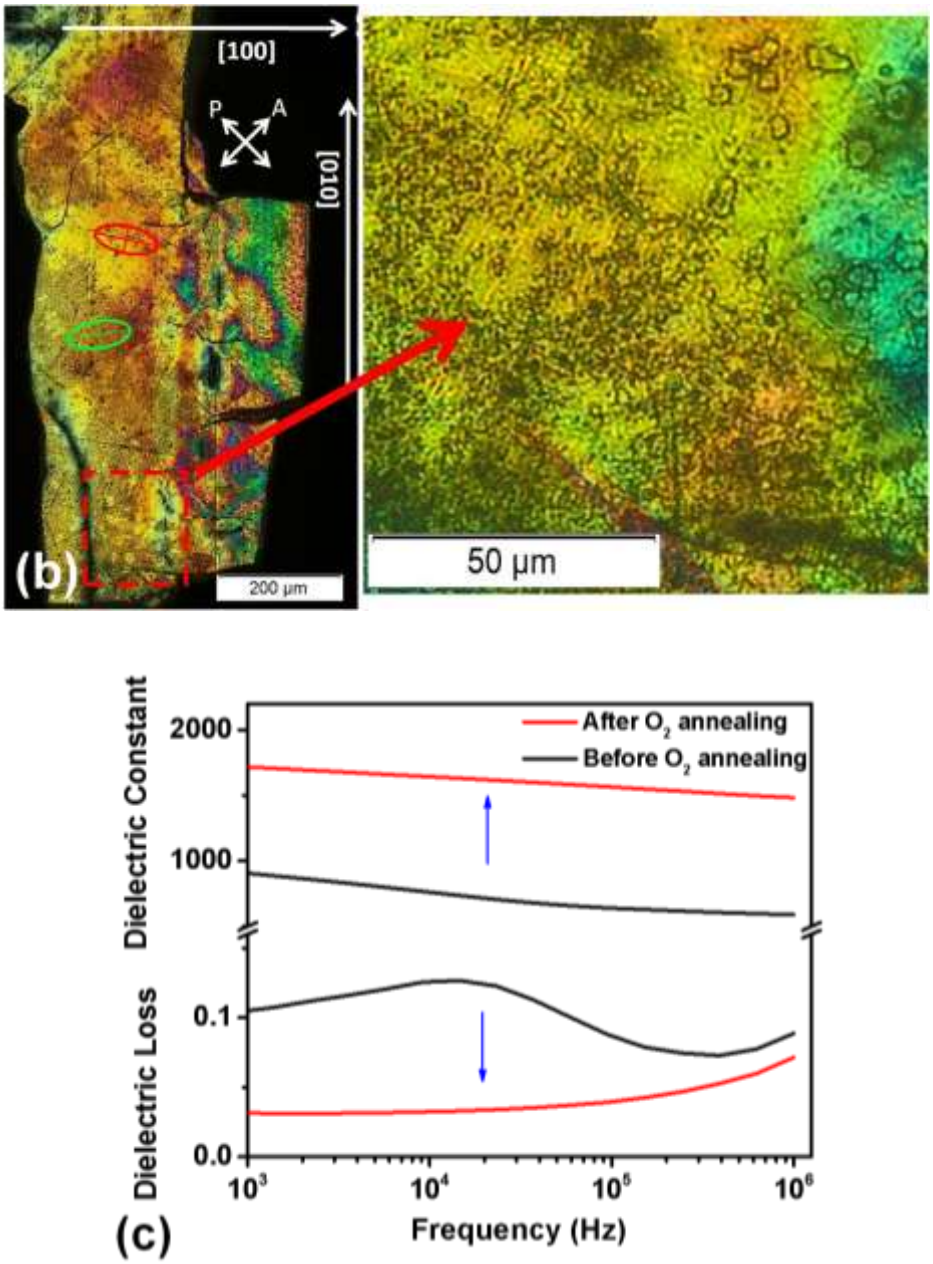

Figure 3.14 PLM image of $[001]_{pc}$ poled 30PIN-35PMN-35PT crystal at room temperature after annealing at 800 ˚C under different condition: (a) in sealed alumina crucible, and (b) in oxygen atmosphere. Enlarged views taken under first order magenta filter (540 nm) were shown on the right hand side of each picture for clearer observation. Noticeably, the typical 90° domain structure of the induced tetragonal phase in (a) has completely disappeared after thermal treatment in O_2. (c) frequency dependence of dielectric constant and loss before and after O_2 treatment.

It is known that with a large electric field applied, charge carriers such as oxygen vacancies in an oxide perovksite are able to migrate in certain directions[81]. Therefore, it is naturally suspected that such anisotropic migration might be responsible for the observed irreversible phase transition behavior. In order to verify this hypothesis on the role of oxygen vacancies, the poled crystal was annealed in O_2 atmosphere at 800 °C for 4 hours. Interestingly, after annealing, the M_C phase is found to have been restored with some variation in the extinction angles [Fig. 3.14. (b)]. The virgin crystal has 3 domains with extinction angels at 0/90 ˚, 16.5 ˚ and -20.5˚, respectively [Fig. 3.9(a)] whereas the crystal annealed in O_2 atmosphere has two domains with extinction angels 8.5 ˚ and -12 ˚, respectively [Fig. 3.14(b)]. Moreover, the dielectric properties measured before and after O_2 annealing [Fig. 3.14. (c)] shows a significant increase in the dielectric constant while at the same time a decrease in loss ($\tan\delta$) after O_2 annealing. Since the only oxygen source is O_2 gas, the mechanism of the compensation is through the direct oxidation of the vacancies:

$$Pb(Me)O_{3-x} + \frac{x}{2}O_2 \rightarrow Pb(Me)O_3\,, \qquad (3.1)$$

where Me in this case stands for the B-site cations (Mg^{2+}, In^{3+}, Nb^{5+} and Ti^{4+}) that has overall 4+ charge. These observations support our assumption that the oxygen vacancies must play an important role and their migration under the application of electric field contributes to the formation and stabilization of the induced T phase.

A detailed model is proposed to explain such mechanism. A previous experiment[33] has shown that the migration of the oxygen vacancy can happen in atomic scale. Simulation based on the first principles pseudopotential method by Park *et al*. [82] has suggested that oxygen vacancies located in the *c*-axis (V_c) of the tetragonal ferroelectric crystal ($PbTiO_3$, *P*4*mm*) have lower potential energy than the ones located in the *a*-*b* plane (V_{ab}). But they also expected that with the application of electric field, certain types of vacancies on the *a*-*b* plane should have lower potential energy instead. From phenomenological understanding, it is also reasonable to expect that the positively charged oxygen vacancies tend to move away from the *c*-axis to minimize the repulsion with the positively charged B-site cations which are displaced towards *c*-axis under the application of electric field along $[001]_{pc}$ direction. Fig. 3.15 a – d describes the poling process and the change of polarization direction from being perpendicular to $(001)_{pc}$

plane in the poled crystal into the direction lying within the $\{001\}_{pc}$ planes after thermal treatment. Before poling, the oxygen vacancies are randomly distributed and thereby do not affect the macroscopic (average) monoclinic symmetry as shown in Fig. 3.15 (a). Upon poling [Fig. 3.15 (a), (b)], the oxygen vacancy is forced to move away from the octahedral axial position (*c*-axis) to a planar position (*a*-*b* plane), while the B-site cation is shift along the same direction of the applied electric field. Annealing at 800 ˚C (above T_C) [Fig. 3.14 (c)] in a sealed crucible would normally resulted in the non-polar cubic phase with all B-site cations on their symmetrical site with zero-off center disappearance on the *c*-axis. However, due to the presence of the internal electric field created by the oxygen vacancies, some B-cations show slight off-center displacement on the *a*-*b* plane even in the apparently cubic phase above T_C. The presence of the "residual" B-cation displacement at high temperature favours the development of tetragonal 90 ˚ domain in the *a*-*b* plane upon the subsequent cooling through T_C, leading to the head-tail polarization arrangement and the stripe domain structure at room temperature, as observed in Fig. 3.13 (a) and sketched in Fig. 3.15 (d) and (e). Previous theoretical study has revealed that oxygen vacancies have the lowest potential energy when sitting on the 90˚domain walls[83, 84], which support our domain model in Fig. 3.15 (e).

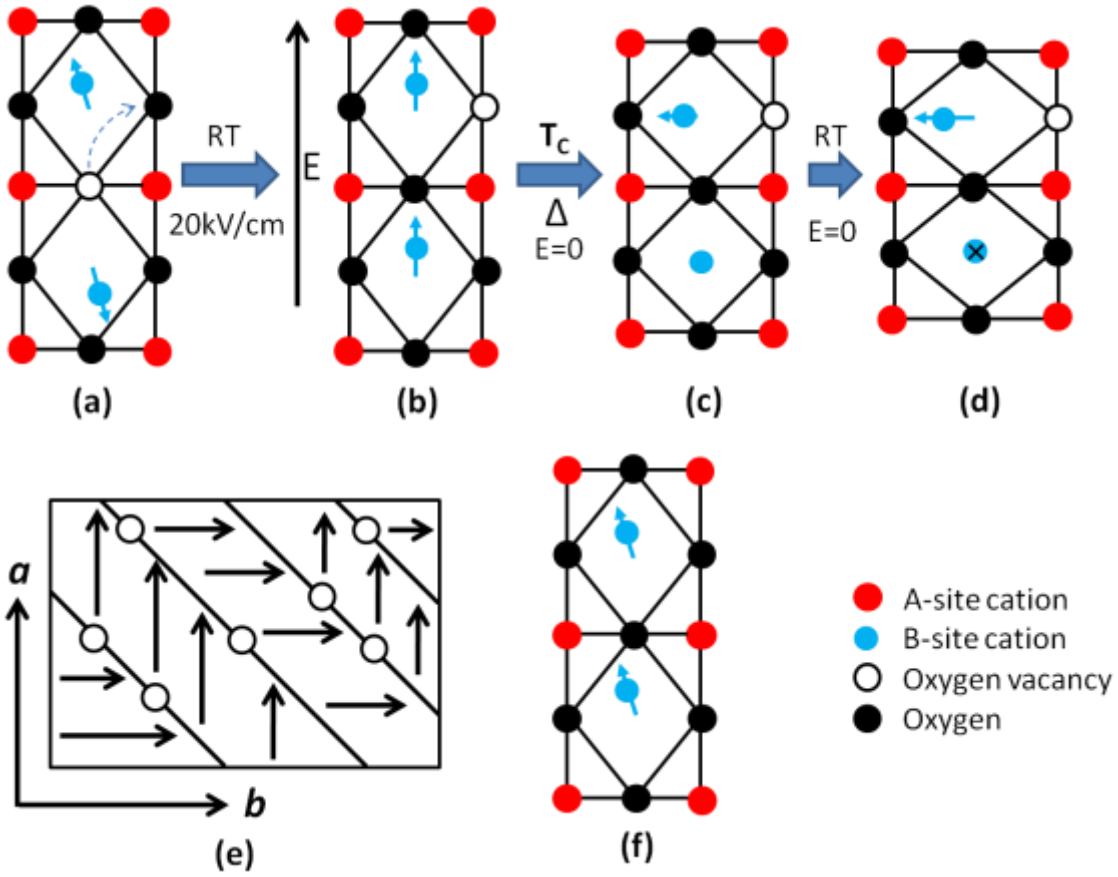

Figure 3.15 Proposed mechanism for the poling/annealing process based on the oxygen vacancy model: (a) unpoled monoclinic state, (b) single domain tetragonal phase induced by a field applied along c-axis, (c) cubic phase upon annealing at temperature above T_C, (d) reappearance of tetragonal phase upon cooling down to room temperature with 90 ˚-domains, (e) schematic pattern of the 90˚-polarization in *a*-*b* plane in the presence of oxygen vacancies, (f) monoclinic domain state after annealing in O_2-atmosphere.

In addition to the oxygen-vacancy migration model, it is also possible that the application of the electric field shifts all the oxygen vacancies to one side of the crystal platelet, creating an internal electric filed which stabilizes the monoclinic domains. Under the influence of such internal field, domains of monoclinic M_C phase resemble the tetragonal domain by having the component of the polarization vectors in [001] direction[74]. However, in order to verify the nature of the domain and its mechanism of formation, further experiment is needed.

Under either circumstance, annealing in O_2 atmosphere allows the poled crystal to uptake oxygen ions through surface, eliminating the internal electric field and the associated "residual" B-cation off-center displacement. As a result, the "memory" or the "precursor effect" of the tetragonal (or monoclinic M_C) phase is "erased" and upon the subsequent cooling through T_C, the original monoclinic domain is restored at room temperature as shown in Fig. 3.14 (b). However, the restored monoclinic domains show some difference in extinction angles from the ones of virgin crystal. It is possible that this discrepancy results from the migration of the oxygen vacancies under repeated annealing process which could result in the change in internal field and thus the direction of polarization.

In addition to the oxygen-vacancy-migration model, it is also worth discussing the possible relationship between our results and "adaptive phase" theory in this paper. Jin *et al.*[38] proposed that monoclinic phase is created by tetragonal or rhombohedral microdomains. The absence of domain structure in virgin crystal [Fig. 3.9(a)] indicates that the domain size λ_0 can actually be very small. It meets the basic assumption of adaptive phase theory that the domain wall energy γ is low due to the fact that $\lambda_0 \propto \sqrt{\gamma}$ [85]. Wang *et al.* [86] also proved that in order to achieve macroscopic monoclinic *Pm* phase, its nanodomain needs to adopt tetragonal structure. Therefore the monoclinic phase observed in our experiment is possibly the result of combination of the tetragonal nanodomain. It is expected that the random distribution of oxygen vacancy in unpoled crystal may not affect the macroscopic monoclinic symmetry. However, under the influence of electric field, collective migration of the oxygen vacancies onto *a-b* plane will establish internal field and therefore lead to large domains size. The increased domain wall energy will therefore favor the formation of macroscopic tetragonal domain over monoclinic domains. Annealing of poled crystal in O_2 atmosphere eliminated internal field by compensating these oxygen vacancies. Thus the system resumed into macroscopic symmetry as monoclinic *Pm* [Fig. 3.13 (b)].

3.4.7. Domain Memory Phenomenon and Polarization Reversal Effect

A FE→FE phase transition is often observed in the relaxor-PT systems with MPB composition below their FE→paraelectric (PE) phase transition temperature T_C. The

nature of FE→FE phase transitions are different in different systems and compositions, e.g. R→M_A phase transition at 87 ˚C for 0.67PMN-0.33PT[87] single crystal, M_C→T phase transition at around 90 ˚C for 0.69PMN-0.31PT ceramic, orthorhombic (O)→T phase transition at around 40 ˚C for 0.9PZN-0.1PT[88]. In previous studies, it was found that the piezoelectric properties generally start to degrade upon heating above this FE→FE phase transition temperature[89-91]. Therefore, the FE→FE phase transition temperature is often referred to as the "depoling temperature". This depoling effect has been a series obstacle to the application of the piezocrystals in electromechanical transducers, as it limits the temperature range of device operation and reduces the thermal stability of the properties. Therefore, there have been great efforts in designing new piezocrystals with high depoling temperatures (T_{RT}, T_C) and enhanced thermal resistance. In this work, one of the most promising ferroelectric materials[56, 57, 92, 93], PIN-PMN-PT system is studied for its depoling effect at FE→FE phase transition. Both PIN-PMN-PT single crystal and ceramics are used to demonstrate the relationship between the thermal depoling effect and the symmetries involved in the FE→FE phase transition.

The PIN-PMN-PT single crystal with nominal composition 30/35/35 examined shows rhombohedral symmetry at room temperature under polarized light microscope. With the increase of temperature, it undergoes a first order rhombohedral (*R*3*m*) → monoclinic M_A (*Cm*) phase transition at 80 ˚C (defined as T_{R-M}), followed by a monoclinic M_A (*Cm*) → cubic ($Pm\bar{3}m$) phase transition at 230 ˚C. Fig. 3.16 (a) shows the evolution of the ferroelastic/ferroelectric domains as the crystal is first heated up to 180 ˚C to pass through the R→M_A phase transition, which can be clearly observed as the reddish colored rhombohedral domains transforms into the monoclinic domains with pale color with clear domain boundary at 80 ˚C. This phase transition is also characterized by the temperature-dependent birefringence and extinction angle in Chapter 3.4.2. After dwelling at 180 ˚C for 15 minutes until the entire domain patterns become stabilized, the crystal is cooled back down to room temperature. It is found that the domain pattern does not show obvious change after going through the R→M_A→R transition cycle. This reveals a very interesting domain memory phenomenon: the rhombohedral domains are preserved at the reversible rhombohedral to monoclinic phase transition, i.e., it is resistant to the thermal depoling at T_{R-M}. However, the domain pattern is completely altered after further annealing above T_C at 240 ˚C (T_C = 230 ˚C) as shown in Fig. 3.16 (b),

indicating original R domain structure is destroyed at $T>T_C$, and a new domain pattern is reconstructed below T_C as a result of the reorientation of the spontaneous polarization and strain. Note, the new R domain pattern developed after the previous annealing cycle still exhibits the domain memory phenomenon when annealed at $T_{R-M}<T<T_C$.

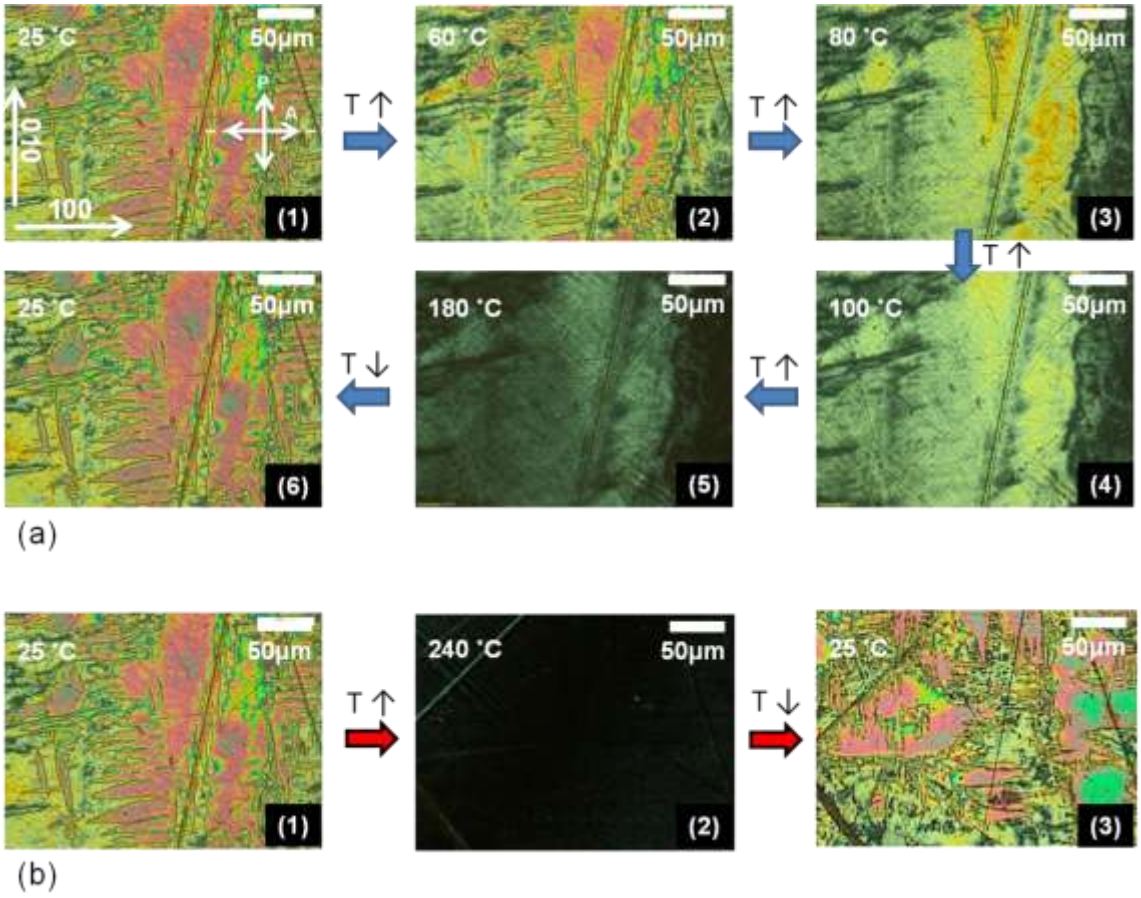

Figure 3.16 Annealing experiment carried out up to (a) T= 180 ˚C, ($T_{R-M}<T<T_C$) and to (b) T= 240 ˚C, ($T>T_C$) on a PIN-PMN-PT single crystal with R→M_A→C phase transition

To confirm the above observed domain memory effect at T_{R-M}, further experiments were carried out in the PIN-PMN-PT ceramics with similar phase transition behavior. PIN-PMN-PT ceramics with various compositions (PIN-PMN-PT: 32-32-36, 34-34-32 and 37-37-26) were prepared under the identical condition by the precursor method described

above. X-ray analysis in Chapter 3.4.2 indicated that the three ceramics possess a pure tetragonal phase, a mixture of rhombohedral and monoclinic phases, and a pure rhombohedral phase, respectively. It is also confirmed that 34PIN-34PMN-32PT undergoes a rhombohedral (*R*3*m*) → monoclinic (*Cm*) phase transition similar to the transition observed in single crystal except its T_{R-M} is at around 110 ˚C, which represents an average R→M_A phase transition temperature. This can be seen in the variations of the dielectric constant as a function of temperature shown in Fig. 3.17. Three ceramics are poled at electric fields strength 2.5 times that of their coercive fields to obtain the best piezoelectric properties followed by annealing in a delta furnace. The piezoelectric constants d_{33} (pC/N) are measured at room temperature after each heating/cooling cycle. The change in piezoelectric properties is measured by recovery percentage that is defined by the ratio of d_{33} value of thermally-cycled samples to the value of the initial freshly poled samples. The variations of the recovery percentage as a function of temperatures at which the samples are annealed are shown in Fig. 3.18. It is observed that the piezo-properties of all three samples degraded after each annealing cycle as the annealing temperature increases. Interestingly, the 34PIN-34PMN-32PT ceramic of MPB composition does not show significant degradation of d_{33} after it is annealed above its T_{R-M}. In fact, it exhibits the best degradation resistance of all the three with d_{33} starting to decrease noticeably after annealing at a temperature close to its T_C. This recovery in piezoelectric coefficient in the ceramics is consistent with the “domain- memory” phenomenon demonstrated in single crystals. Together, these phenomena point to peculiar polarization reversal process which can be described by a model proposed below.

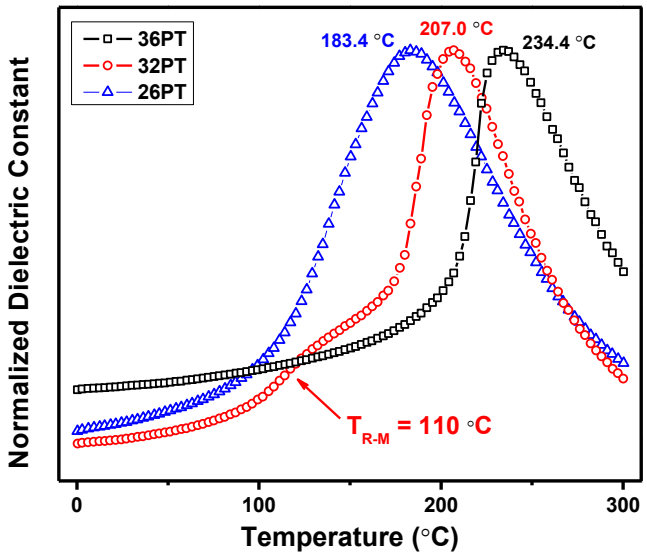

Figure 3.17 Temperature dependent dielectric spectroscopy measured at 10^5 Hz for PIN-PMN-PT 32-32-36, 34-34-32 and 37-37-26 ceramics

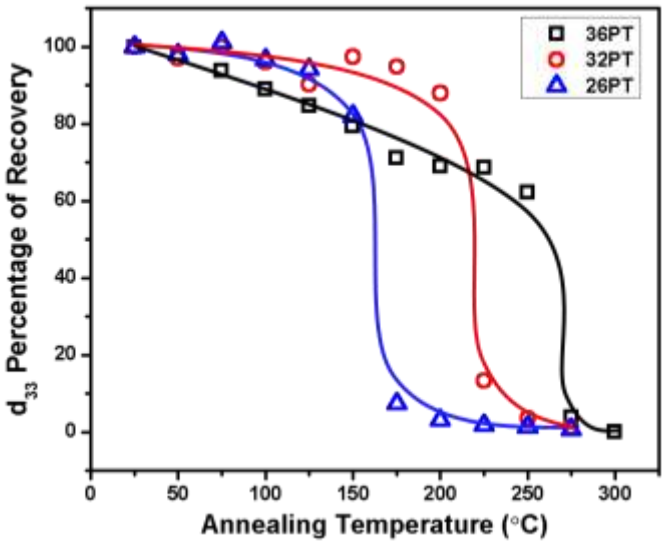

Figure 3.18 Annealing experiment for PIN-PMN-PT 32-32-36, 34-34-32 and 37-37-26 ceramics

It is known that crystals with a higher symmetry such as R, T or O phases have more restrictions in the polarization directions (8 allowed direction for R, 6 for T, 12 for O phases) than the one with a lower symmetry such as monoclinic phase (24 allowed), (polarization rotation in the $\{110\}_{pc}$ plan for M_A/M_B, and in the $\{100\}_{pc}$ for M_C). From the symmetry point of view, As is known that the M_A phase serves as a "bridging phase" between the rhombohedral (polarization oriented at $[111]_{pc}$ directions) and the tetragonal (polarization oriented at $[100]_{pc}$ directions) phases with its polarization lying in the $\{110\}_{pc}$ planes (pseudocubic setting of the unit cell is used throughout the paper). According to the polarization rotation theory[16], the polarization rotating within $\{110\}_{pc}$ plan has the lowest energy compared to other possible path. Therefore, if the system is cooled down from the intermediate monoclinic M_A phase to room temperature rhombohedral phase through T_{R-M}, the polarization components that lie in the $\{110\}_{pc}$ planes are expected to switch back to the original $\{111\}_{pc}$ direction to minimize that of potential energy, as shown in Fig. 3.19 (a). On the other hand, annealing at a temperature above T_C results in the vanishing of the spontaneous polarization and the associated piezoelectricity. When cooled through T_C down to room temperature, the crystal will develop a total different rhombohedral domain pattern [Fig. 3.16 (b).3)] compared with the one before annealing [Fig. 3.16 (b).1)].

Based on this consideration we can understand the mechanism of depoling effect observed in binary and ternary piezocrystals that results from the rhombohedral to tetragonal phase transition in the MPB region. At the first order rhombohedral → tetragonal phase transition, the polarization in the $[111]_{pc}$ direction will have three equally possible rotation path ways: $[001]_{pc}$, $[010]_{pc}$, $[100]_{pc}$ directions, forming three tetragonal domains with different polarization directions. When this multidomain tetragonal phase is cooled back down to the room temperature rhombohedral phase, the polarization in each tetragonal state will then have four equally possible rotation pathways. For example, the tetragonal unit cell with polarization in $[001]_{pc}$ direction can return to rhombohedral phase with polarization in $[111]_{pc}$, $[\bar{1}11]_{pc}$, $[1\bar{1}1]_{pc}$, and $[\bar{1}\bar{1}1]_{pc}$ directions with equal possibilities, as shown by the 4 curved arrow in Fig. 3.19 (b). Similar effect will take place for the other two tetragonal polarizations in $[010]_{pc}$ and $[100]_{pc}$ directions as well. Therefore, after going through the transition at $T_{R-T}<T<T_C$ (R→T→R sequence) and come back, the original rhombohedral polarization in $[111]_{pc}$ direction is turned into 7

possible polarization orientations ($[111]_{pc}$, $[\bar{1}11]_{pc}$, $[1\bar{1}1]_{pc}$, $[\bar{1}\bar{1}1]_{pc}$, $[11\bar{1}]_{pc}$, $[\bar{1}1\bar{1}]_{pc}$ and $[1\bar{1}\bar{1}]_{pc}$) as listed in Fig. 3.19 (b). This polarization redistribution gives rise to the depoling effect at T_{R-T}, which in turn leads to the degradation of the piezoelectric properties. The redistribution effect is also cumulative since multiple-times annealing will eventually lead to polarization randomized in all the 8 permissible rhombohedral $\{111\}_{pc}$ directions, further degrading the piezo-properties.

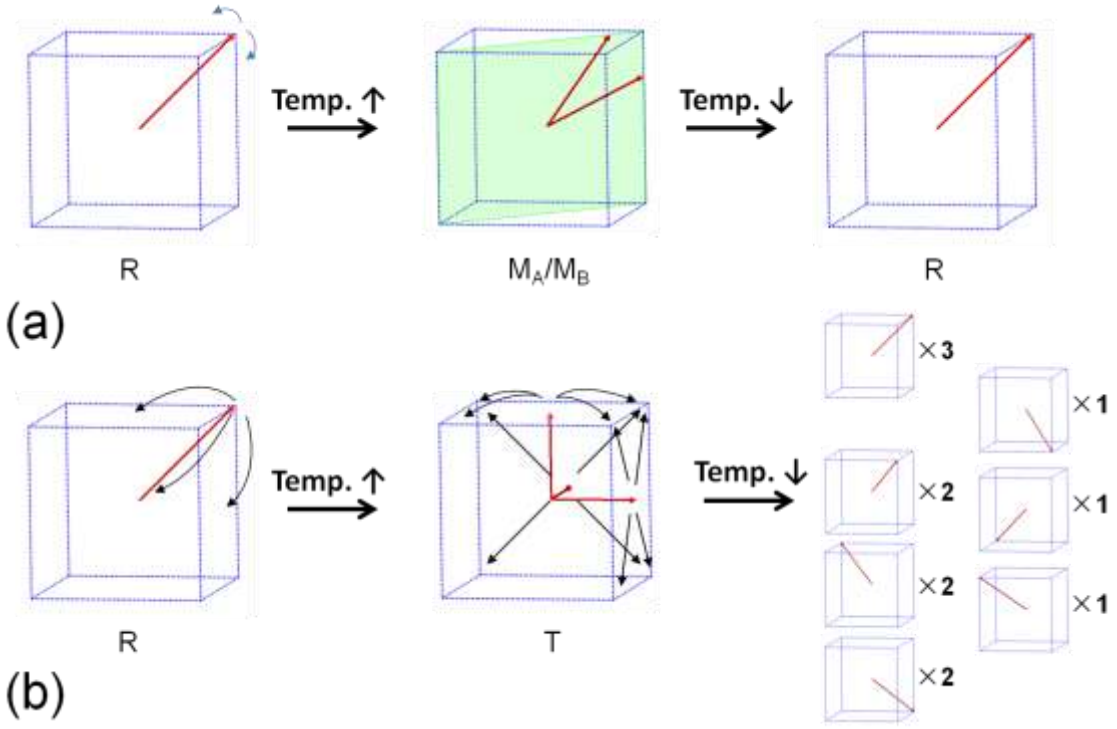

Figure 3.19 (a) A system going through rhombohedral (*R*3*m*) → monoclinic (*Cm*) phase transition will relax to its original polarization state after annealed at $T_{R-M} < T < T_C$. (b) A system going through rhombohedral (*R*3*m*) → tetragonal (*P*4*mm*) phase transition when annealed at $T_{R-T} < T < T_C$ will result in 7 different polarization states (×3, ×2 and ×1 indicate possibility for each state).

3.5. Conclusion

It is discovered that the rhombohedral, monoclinic M_C and tetragonal phases coexist in a compositionally segregated PIN-PMN-PT single crystal (nominal composition 30/35/35) at room temperature. The rhombohedral to a low symmetry phase transition takes place at 80 ˚C as evidenced by the significant change in both the extinction angle and birefringence. Ceramic samples with similar compositions across the morphotropic phase boundary were prepared and analyzed by XRD, which lead to the resolution of the symmetry of this low symmetry phase to be monoclinic M_A. The M_C phase is also observed in the same single crystal sample with all three M_C domains distinguished by their signature temperature-dependent extinction angles θ_M. A pseudo-binary phase diagram of the (1-z)(PINPMN)-zPT system with the MPB region of the ternary PIN-PMN-PT solid solution has been proposed based on the structural, optical and dielectric results of both single crystal and ceramic systems. It helps clarify the MPB phase components of the ternary system, understand the structure and properties of the high performance ternary piezocrystals.

In addition, application of an electric field on the monoclinic M_C phase of the $(001)_{pc}$ – PIN-PMN-PT crystal is found to induce a tetragonal phase of single domain state. This induced phase transition is irreversible as the tetragonal phase reappears at room temperature after heating above T_C = 230 ˚C, It is proposed that the electric field causes collective migration or hopping of oxygen vacancies onto more stable planer positions during the poling. This ordered oxygen vacancy arrangement and the associated internal field favors the development of tetragonal 90 ˚domains upon subsequent cooling through T_C. This oxygen-vacancy-migration mechanism is supported by the different domain structure observed under PLM, and the different dielectric properties measured before and after thermal treatment in O_2 atmosphere, which is found to restore the M_C phase by compensating the oxygen vacancies eliminating the vacancy-related tetragonal phase memory effect. The role of oxygen vacancies in the formation of domain structure and phase symmetry found in this work may help understanding other domain engineering and phase transition phenomenon.

The domain memory effect and the polarization reversal phenomenon associated with the R→M_A phase transition are also discovered in the PIN-PMN-PT single crystal and ceramics and are interpreted by a polarization-reversal model. This phenomenon enables certain types of ferroelectric materials to restore their polarization state and domain structure after experiencing FE→FE phase transition from a higher symmetry phase (R) to a lower symmetry phase (M_A) upon heating. A direct consequence of the polarization reversal effect and domain memory phenomenon is that the piezoelectric coefficient of the material does not undergo degradation following the R→M_A phase transition as opposed to the conventional R→T MPB transition which leads to the depoling and severe degradation of the piezo-performance. Our results, observations and interpretations provide a new guidance in the designing and selection of piezo/ferroelectric with a wider operation temperature range: the MPB composition undergoing a higher symmetry to a lower symmetry phase can exhibit the improved temperature tolerance compared with the conventional MPB compositions, becoming the material of choice for high depoling temperature and high performance piezoelectrics for a wide range of applications as electromechanical transducers.

Chapter 4: Study of $Pb(Mn_{1/2}W_{1/2})O_3$ - $Pb(M_{1/2}W_{1/2})O_3$ (M = Zn and Mn) Antiferroelectric Solid Solution

Part of this chapter are revised from the papers published 1). by Z. Ren, N. Zhangand Z.-G Ye in *Ferroelectrics* **455**, 49 (2013) and 2). by Z. Ren, N. Zhang, X. Long, and Z.-G Ye in *J. Am. Ceram. Soc.*, **97** 1700 (2014). The use of the articles are permitted by the publisher of Taylor and Francis and WILEY.

4.1. Abstract

A solid solution of $(1-x)Pb(Mg_{1/2}W_{1/2})O_3$-$xPb(Zn_{1/2}W_{1/2})O_3$ has been prepared in the form of ceramics by solid state reaction with composition x up to 30%.It is found that with the substitution of Zn^{2+} for Mg^{2+}on the B-site of the complex perovskite structure, the antiferroelectric (AFE) Curie temperature T_C of PMW increases from 40 °C (x =0) to 67 °C (x = 30%), indicating an enhancement of antiferroelectric order, while, at the same time, the phase transition becomes more diffuse due to a higher degree of chemical inhomogeneity. X-ray diffraction analysis indicates that the crystal structure adopts an orthorhombic space group (*Pmcn*) with a decrease in lattice parameter *a* but an increase in *b* and *c* as the Zn^{2+} concentration increases. The low dielectric constant (~10^2), low dielectric loss ($\tan\delta \approx 10^{-3}$), linear field-induced polarization and significantly high breakdown field (~125 kV/cm) at room temperature make this family of dielectric materials a promising candidate for ceramic insulators.

Solid solution of $(1-x)Pb(Mg_{1/2}W_{1/2})O_3$-$xPb(Mn_{1/2}W_{1/2})O_3$ ($0 \le x \le 0.5$) of perovskite structure has also been prepared by solid state reaction method with Mn^{2+} substituting for Mg^{2+}. The effects of Mn-substitution on the crystal structure, magnetic properties, grain morphology and dielectric properties are investigated by X-ray diffraction (XRD), electron paramagnetic resonance (EPR), SQUID magnetometry, scanning electron microscopy

(SEM) and dielectric spectroscopy. At room temperature, the solid solution system undergoes a phase transition from *Pmcn* to $\boldsymbol{Fm\bar{3}m}$ with the increase of Mn concentration. The EPR and SQUID measurements confirm that Mn ion exists in a high spin state (S=5/2) with a 2+ oxidation state. The grain size is significantly enlarged, which can be attributed to the effects of a transient liquid phase present during the sintering process. The Curie temperature (T_C) slightly increases with the substitution of Mg^{2+} for Mn^{2+} up to x=0.2, followed by a significant decrease with x≥0.25. The study of the Mn-substitution for Mg provides insights into the role of Mn-ion in Pb-based perovskite system.

4.2. Introduction

Pb-based perovskite crystals are one of the most important members in electric materials for their piezoelectric[94] and magnetic properties[95, 96]. Among all the complex perovskite systems, compounds of $Pb(B_{1/2}B'_{1/2})O_3$ have been studied for decades for their interesting structure and electrical properties. In $Pb(B_{1/2}B'_{1/2})O_3$, the degree of structural ordering depends sensitively on the differences in the charges and radii of B and B' cations. $Pb(Mg_{1/2}W_{1/2})O_3$ (PMW) was first synthesized in 1959[18] and is known to have an ordered structure with orthorhombic centrosymmetric space group *Pmcn*[20]. The antiferroelectricity was revealed by the antiparallel displacements of Pb^{2+} ions in the $[100]_{pc}$ and $[010]_{pc}$ directions in the cubic perovskite framework.

On the other hand, $Pb(Zn_{1/2}W_{1/2})O_3$ (PZW), predicted to be antiferroelectric[97], was reported to exist in the perovskite phase only by high pressure synthesis[98]. It is partially due to the fact that Zn^{2+} with a fully filled 3*d* orbital reduces its ionic feature[99] which is important in destabilizing the perovskite structure. Study of local density states of the $Bi(Zn,Ti)O_3$-$PbTiO_3$ system[100] also indicates the existence of strong hybridization between Zn^{2+}'s 4s and 4p orbitals and oxygen's 2p orbitals, which allows short Zn-O covalent bonds. The off-center displacement of Zn^{2+} due to the Zn-O bonding could also be a reason that prevents the formation of PZW in perovskite structure at ambient pressure.

In phase pure $Pb(B^{2+}B'^{6+})O_3$ systems, due to the large difference in charges, the ordering between B and B' ions is very difficult to be disrupted. Therefore, $Pb(B^{2+}B'^{6+})O_3$ systems are difficult to form solid solutions with other perovskite compounds with a high solubility. However, the high degree of order of $Pb(Mg_{1/2}W_{1/2})O_3$ makes it possible to stabilize $Pb(Zn_{1/2}W_{1/2})O_3$ in the perovskite structure by substituting Zn^{2+} for Mg^{2+} to form the $(1-x)Pb(Mg_{1/2}W_{1/2})O_3$-$xPb(Zn_{1/2}W_{1/2})O_3$ solid solution. In this work, such a new solid solution has been synthesized and its dielectric properties characterized.

Pb-based perovskite materials form an important class of functional materials for its interesting electric[94] and magnetic properties[95, 96]. For Pb-based piezo-/ferroelectric perovskites, Mn has been widely used as an acceptor type dopant to enhance the coercive field (E_C) and the mechanical quality factor (Q_m)[10, 101]. However, Mn-doping concentration is generally too low to systematically study the behavior of Mn ion in these materials or to reveal the bonding environment and its influence on the crystal structure and thereby the properties. On the other hand, due to the multi-valence property of Mn-ion[102], it is difficult to incorporate Mn-ion in Pb-based perovskites at high concentration. Therefore, isovalent substitution method becomes relevant in order to obtain single phase Pb-based perovskites containing a high Mn concentration. Complex perovskite $Pb(Mg_{1/2}W_{1/2})O_3$[18,20] was considered as one of the best candidates for such studies. Compared with $Pb(Mg_{1/2}W_{1/2})O_3$, single phase $Pb(Mn_{1/2}W_{1/2})O_3$ compound has not been synthesized in pure perovskite structure by conventional solid state reaction method. To the best of our knowledge, the only successful synthesis of $Pb(Mn_{1/2}W_{1/2})O_3$ perovskite under ambient pressure was achieved in an Ar stream[103, 104] where $Pb(Mn_{1/2}W_{1/2})O_3$ crystallizes in the space group *Pnma* possessing $2_1/n$ $2_1/m$ $2_1/a$ symmetry elements which is equivalent to *Pmcn* with $2_1/m$ $2_1/c$ $2_1/n$ symmetry elements. On the other hand, this high degree of order makes it possible to stabilize $Pb(Mn_{1/2}W_{1/2})O_3$ in the perovskite structure by the substitution of Mn^{2+} for Mg^{2+} to form the $(1-x)Pb(Mg_{1/2}W_{1/2})O_3$-$xPb(Mn_{1/2}W_{1/2})O_3$ solid solution. This new solid solution has been synthesized with a high solubility up to x=0.5. The crystal structure, magnetic and dielectric properties have been systematically characterized by a variety of techniques to study the effects of Mn^{2+}-substitution for Mg^{2+} on the local structure and properties of the antiferroelectric $Pb(Mg_{1/2}W_{1/2})O_3$.

4.3. Experiment

The solid solution of (1-x)Pb($Mg_{1/2}W_{1/2}$)O_3-xPb($M_{1/2}W_{1/2}$)O_3(M = Zn and Mn) were prepared by a two-step solid state reaction method. Prior to reaction with PbO, $MgWO_4$, $ZnWO_4$and $MnWO_4$ precursor phases were synthesized at 1000 °C for 12 hours with 5% excess of MgO added for the purpose of suppressing the formation of a secondary phase (Pb_2WO_5). It is also noticed that, in order to form a pure perovskite phase, an excess of 0.5-1% PbO was needed to compensate the lead oxide evaporation at high sintering temperatures. In the second step, the pre-formed precursors and PbO were mixed, ground and calcined at 850 °C for 4 hours to obtain a pure perovskite phase. The calcined samples were then ground into fine powder and pressed into pellet to be sintered. The sintering process took place at temperature varying from 1100 to 850 °C for 2 - 2.5 hours to obtain dense ceramics. X-ray powder diffraction was performed on BrukerD8 diffractometer, using Cu Kα radiation (λ = 1.5405 Å) to determine the crystal structure. The temperature dependence of the dielectric permittivity of the ceramics was measured using a *Novocontrol* broadband dielectric spectrometer from -50 to 200 °C at various frequencies. The polarization - electric field relationship was displayed with an RT-66 ferroelectric test system (Radian Technology).Magnetization measurements were performed using a Quantum Design MPMS-XL-7S SQUID magnetometer. Electron paramagnetic resonance spectra were collected at X-band (9.3−9.4 GHz) using a Bruker EMXplus spectrometer with a Premium X microwave bridge and HS resonator. The visualization of ceramic grains was done with a Strata235 Dual beam SEM/FIB.

4.4. Results and discussion

4.4.1. Study of antiferroelectric (1-x)Pb($Mg_{1/2}W_{1/2}$)O_3-xPb($Zn_{1/2}W_{1/2}$)O_3 (PMW-PZW) as dielectric ceramics

Fig. 4.1 shows the X-ray diffraction patterns of samples prepared. It can be seen that the (1-x)Pb($Mg_{1/2}W_{1/2}$)O_3-xPb($Zn_{1/2}W_{1/2}$)O_3 solid solution with x = 0% to 30% was synthesized in pure perovskite phase in the form of ceramics at different sintering temperatures. During the synthesis, it was realized that the sintering temperature of the ceramics decreases as x increases, as shown in Fig. 4.2. This is reasonable since

$Pb(Zn_{1/2}W_{1/2})O_3$ exhibits a low stability and tends to decompose to form Pb_2WO_5 and ZnO at high temperatures instead of forming the perovskite structure. The optimum sintering temperatures were determined by the phase purity and the maximum density of the ceramics. With x=0%, 10% and 20%, the samples calcined at 850 °C and sintered at temperatures above 1000 °C were phase pure. With x=30%, the samples needed to be calcined at 780 °C and sintered at 850 °C in order to obtain the pure perovskite phase. Ceramics with x=30% sintered at 860 to 975 °C showed no sign of melting but the Pb_2WO_5 phase could be clearly observed in the XRD pattern (Fig. 4.1). For x>30%, no pure perovskite phase could be formed, but instead, a noticeable amount of Pb_2WO_5 was present (Fig. 4.1) as a result of decomposition. In addition, the pellets prepared at high sintering temperatures were not dense ceramics any more. This decomposition phenomenon was also reported in previous attempt to synthesize PZW[105]. The superlattice peak such as (1/2, 1/2, 1/2) peak, was also observed from x=0 to 30%, indicating the strong ordering between B-site (Mg^{2+}, Zn^{2+}) and B'-site (W^{6+}) ions.

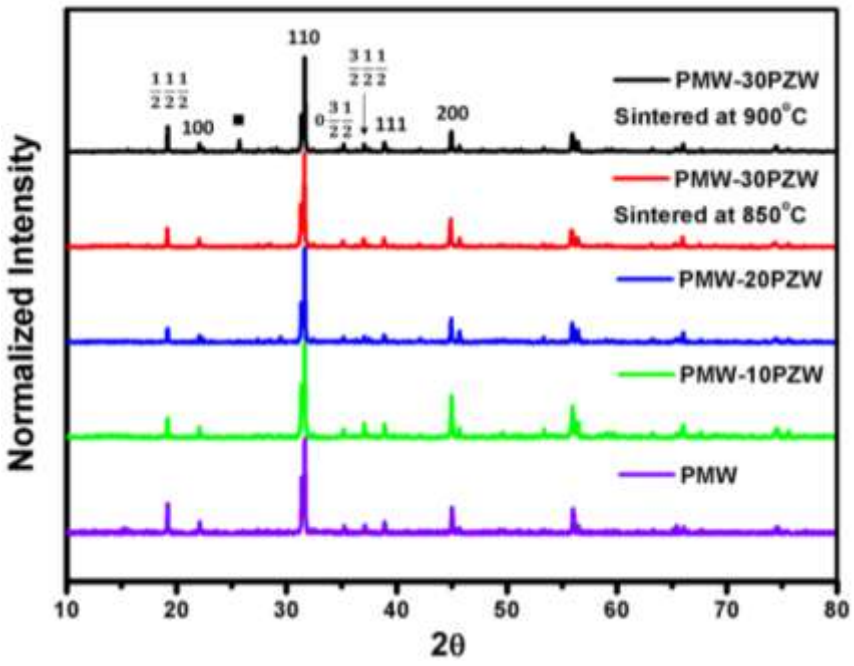

Figure 4.1 XRD patterns of the (1-x)PMW-xPZW (x=0, 10, 20 and 30%) ceramics; Peaks are indexed by pseudocubic framework; The secondary phase of Pb_2WO_5 was marked by a solid square

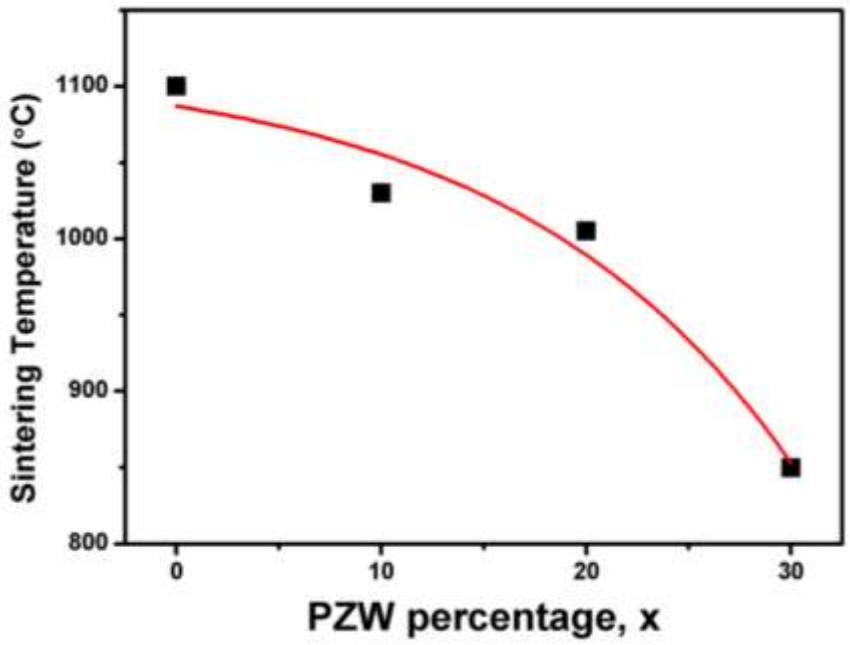

Figure 4.2 Plot of optimum sintering temperature as a function of composition for the (1-x)PMW-xPbZW ceramics

Analysis of the X-ray diffraction patterns indicated that the solid state system adopts the orthorhombic *Pmcn* structure and the crystal structure varies as a function of component in the following way: lattice parameter *a* decreases while *b* and *c* increase with the increase amount of Zn^{2+} (Fig. 4.3). The unit cell volume increases with increasing x, which is consistent with the crystal chemistry prediction since Zn^{2+} has a larger ionic radius(0.74 Å) than Mg^{2+} (0.72 Å)[1].

The polarization (P) - electric field (E) measurements of the (1-x)PMW-xPZW solid solution (Fig. 4.4) show that the P(E) relationship is rather linear. Measurement for PMW-30PZW was not conducted due to its poor sample quality and high leakage current. The small remanent polarization (~ 0.1 μC/cm^2) could arise from electric-field-induced polarization, but the maximum induced polarization is still relatively low (~ 1 μC/cm^2). No double hysteresis loop could be displayed at a field up to 125 kV/cm, suggesting that the field for AFE polarization switching is very high and material behaves like dielectric even though it has an antiferroelectric structure.

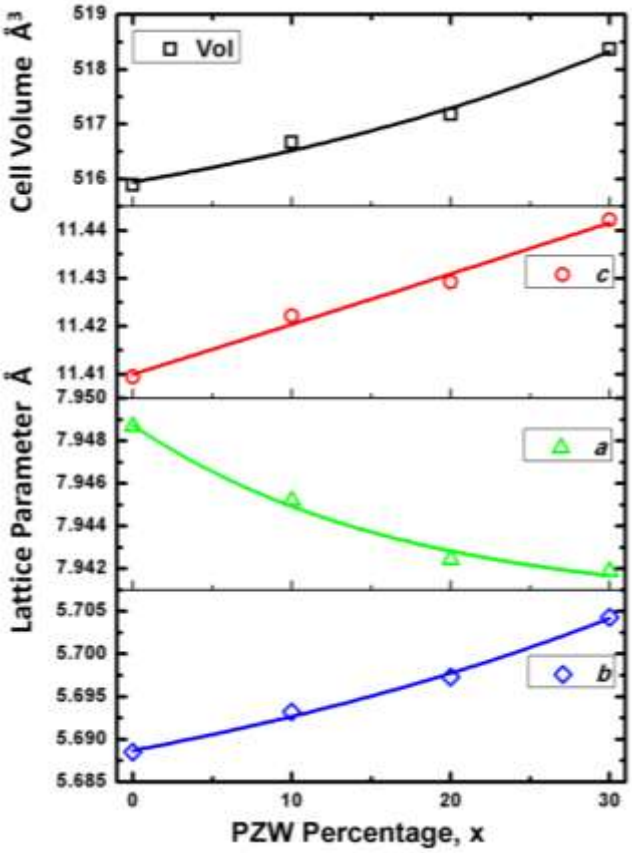

Figure 4.3 Variations of the lattice parameter a, b, c and unit cell volume (in the orthorhombic *Pmcn* space group) as a function of the composition x for the (1-x)PMW–xPZW solid solution

The temperature dependence of the real part of relative permittivity (or dielectric constant) and the dielectric loss of the PMW-xPZW ceramics measured at various frequencies are shown in Fig. 4.5. The phase transition from antiferroelectric to paraelectric phase took place upon heating at the Curie temperature T_C, as evidenced by the sharp peaks or anomalies in the dielectric curves. The room temperature dielectric constant value is typically around 100. No frequency dispersion of the phase transition temperature T_C was observed, indicating the lack of relaxor behavior. With the increase of the substitution rate of PZW for PMW, T_C increases from 40.8 ˚C (x =0) to 67.9 ˚C (x = 30%), indicating an enhancement of antiferroelectric order in the solid solution system. At the same time, the phase transition becomes more diffuse with increasing x, which is caused by an increased disparity in local phase transition

temperature as a result of increase in chemical heterogeneity. It is also noticed that there exist some anomalies in the plot of dielectric loss for PMW-10PZW, PMW-20PZW and PMW-30PZW below their T_Cs. Repeating the measurements with same samples resulted in the appearance of these anomalies at different magnitude and temperature. In addition, such abnormal behavior was not observed in the plot of dielectric constant vs. temperature. Therefore it is believed that the anomalies are due to the variation of sample quality as well as the instrumental noise in measuring the imaginary part of the permittivity instead of the effect of phase transition.

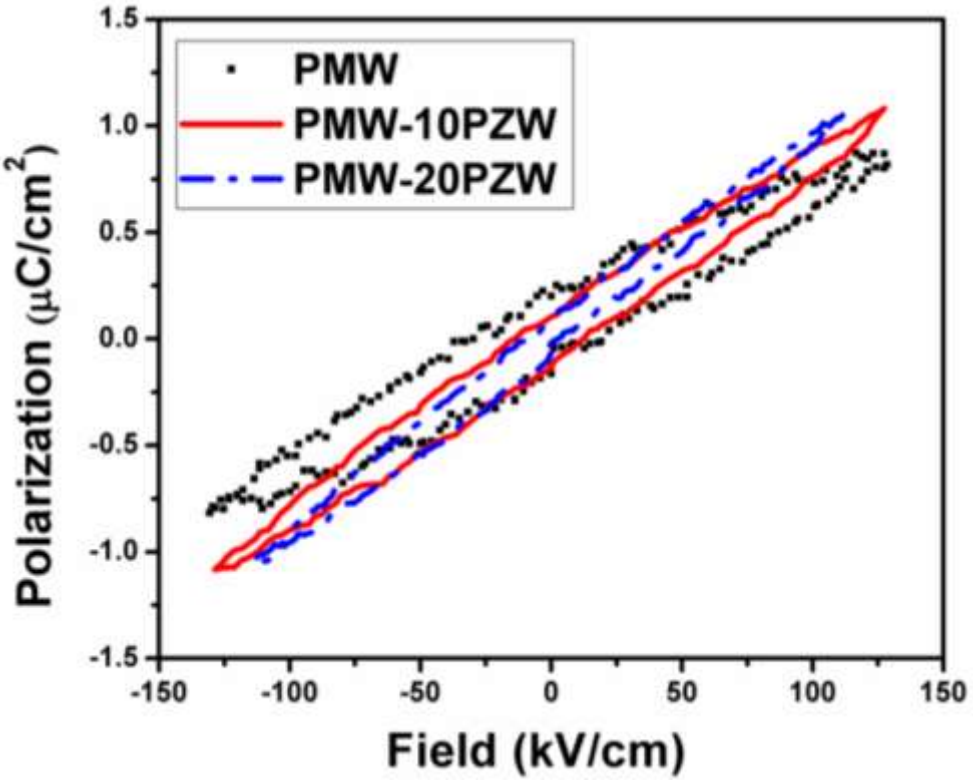

Figure 4.4 Polarization - electric field relations of the PMW-10PZW and PMW-20PZW ceramics

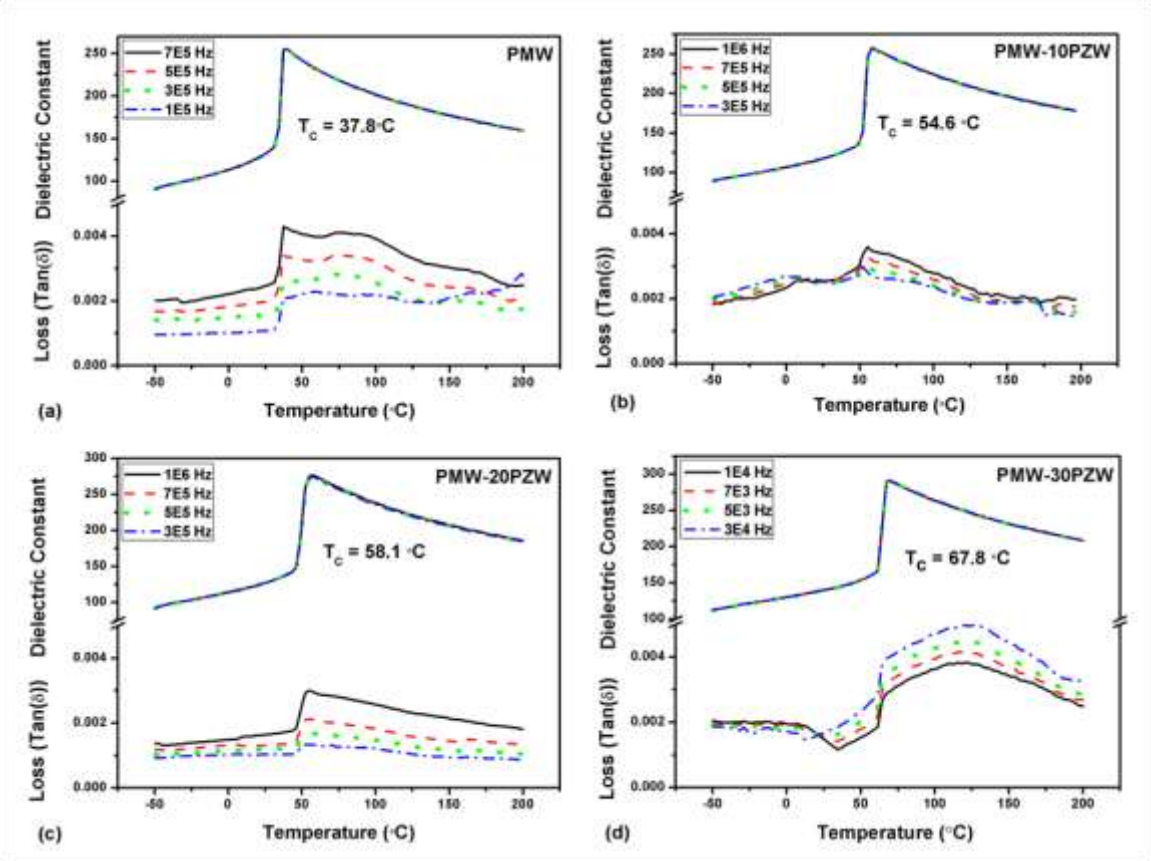

Figure 4.5 Variations of the dielectric constant (ε') and loss tangent (tan δ) of the (1-x)PMW-xPZW ceramics (x=0, 10, 20, 30%) as a function of temperature measured at various frequencies

The increase in T_C could be related to the change in the tolerance factor of the perovskite ABO_3 structure,

$$t = \frac{r_A + r_O}{\sqrt{2}(r_B + r_O)} \quad (4.1)$$

,

wherer_A, r_B, and r_O are the radii of the A(XII), B(VI) and O(VI) ions, respectively. The tolerance factor *t* generally indicates the stability of the perovskite structure (with 1 for a perfect cubic structure). A general trend has been noticed that an increase in the phase transition temperature of antiferro-/ferroelectric perovskites is usually accompanied with

a decrease in the *t* value[106]. Therefore, with *t* = 0.992 for PMW and 0.987 for PZW, the increase of T_C with a higher level of PZW is consistent with such a trend.

4.4.2. Effect of Mn in (1-x)Pb($Mg_{1/2}W_{1/2}$)O_3-xPb($Mn_{1/2}W_{1/2}$)O_3 (PMW-PMnW) solid solution

The XRD patterns of the (1-x)Pb($Mg_{1/2}W_{1/2}$)O_3-xPb($Mn_{1/2}W_{1/2}$)O_3 solid solution are shown in Fig. 4.6 (a). The refinements of the major diffraction peaks indicate that the solid solution system crystallizes in a single phase perovskite structure with orthorhombic *Pmcn* symmetry for 0≤x≤0.2. No sign of secondary phases is found in this compositional range. The antiferroelectric nature was revealed by the antiparallel displacements of Pb^{2+} ions in [100] or [010] directions in the double-perovskite pseudocubic (*pc*) setting [Fig. 4.7 (a)]. The presence of the $(031)_{pc}$ and $(231)_{pc}$ peaks observed with 0≤x≤0.2 indicates the ordering created by the Pb-displacements[107]. At 0.25≤x≤0.3, splitting of the $(400)_{pc}$ peak can be clearly observed, suggesting a mixture of phases. The Rietveld refinement confirms that the mixed phases include *Pmcn* and $Fm\bar{3}m$. With the increase of x, the relative intensity of the $(031)_{pc}$ and $(231)_{pc}$ peaks decreases and eventually vanishes at x=0.4. Variation of the Pb^{2+}-displacement along the *y* and *z*-direction are calculated from the Rietveld refinements and their variation as a function of composition are shown in Fig. 4.6 (c) to represent the evolution of antiferroelectric structure. The displacement along the x-direction is not shown here as there is no significant change. The Pb^{2+}-displacements decreases as x increases and eventually vanishing at x=0.4, indicating that the antiferroelectricity is diminished with the increase of x and disappears at x=0.4. At x≥0.4, the $(311)_{pc}$ and $(400)_{pc}$ peaks become singlet, suggesting that the unit-cell symmetry changes into a single phase cubic $Fm\bar{3}m$, as shown in Fig. 4.7 (b), confirming the disappearance of the AFE. In Fig. 4.6 (a), the "left shoulder" of the $(400)_{pc}$ peak in x=0.5 is the result of a secondary $PbWO_4$ phase, indicating that the solubility limit is reached. Fig. 4.6 (b) shows the calculated lattice parameters as a function of Mn concentration x. The orthorhombic lattice is condensed into double-perovskite pseudocubic (*pc*) framework for better visualization by the following equations: $a_{pc} = a_o$; $b_{pc} = \sqrt{b_o^2 + (\frac{c_o}{2})^2}$. Noteworthily, this pseudocubic structure condensed from orthorhombic structure is in fact pseudotetragonal with $b_{pc} > a_{pc}$. Both lattice parameters a_{pc} and b_{pc} for the antiferroelectric phase increase with the increasing amount of Mn-substitution up to

x=0.3. As an analogue to the conventional *c/a* ratio for tetragonality, the ratio of a_p/b_p is used here to represent the tetragonality of the condensed pseudocubic/tetragonal unit cell. It is plotted as a function of composition in the inset of Fig. 4.6 (b). The increase of tetragonality from 0.9865 for x=0 to 0.9892 for x=0.3 suggests that in antiferroelectric phase, pseudocubic unit cell becomes less compressed with the increase of Mn substitution. This phenomenon is further interpreted by the analysis of EPR results on. The lattice parameter ***a'*** for the $Fm\bar{3}m$ phase also increases with increasing Mn content from x≥0.25 on. The coexistence of *Pmcn* and $Fm\bar{3}m$ phases as well as the abrupt change of lattice parameters at x≥0.25, suggests a first-order phase transition induced by the Mn-substitution.

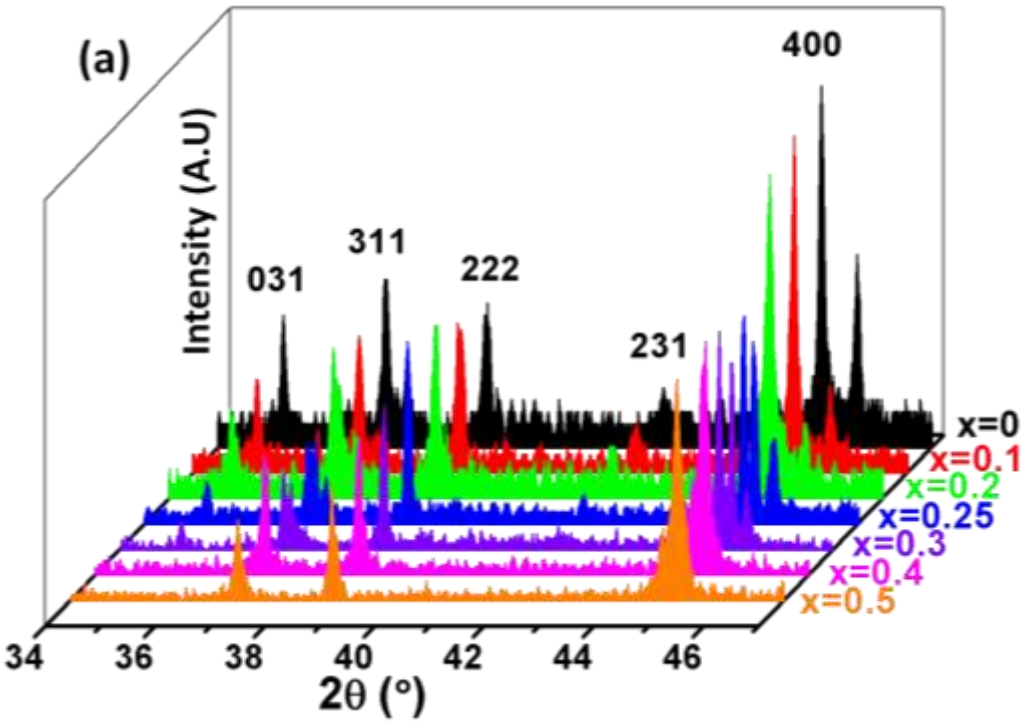

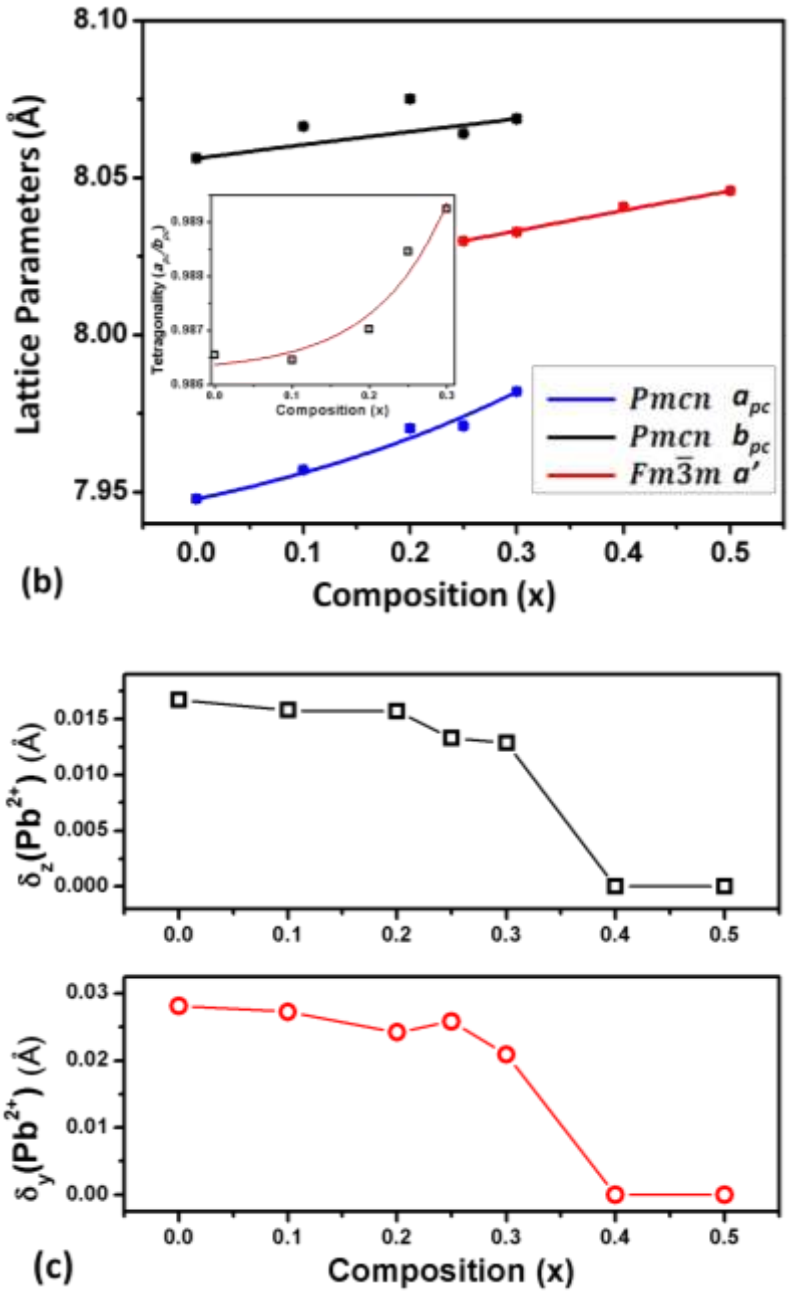

Figure 4.6 (a) XRD patterns of the (1-x)Pb($Mg_{1/2}W_{1/2}$)O_3–xPb($Mn_{1/2}W_{1/2}$)O_3 compounds. Peaks are labeled in double-provskite pseudocubic setting. (b) Plots of the lattice parameters vs. composition. The orthorhombic unit cell was converted into double-perovskite pseudocubic via: $a_{pc} = a_o$; $b_{pc} = \sqrt{\boldsymbol{b_o^2} + (\frac{c_o}{2})^2}$. The tetragonality ($a_{pc}/b_{pc}$) for 0≤x≤0.3 is shown as inset. (c)Variations of the Pb^{2+}-displacements in the y (bottom, red curve) and z (top, black curve) directions as a function of composition x.

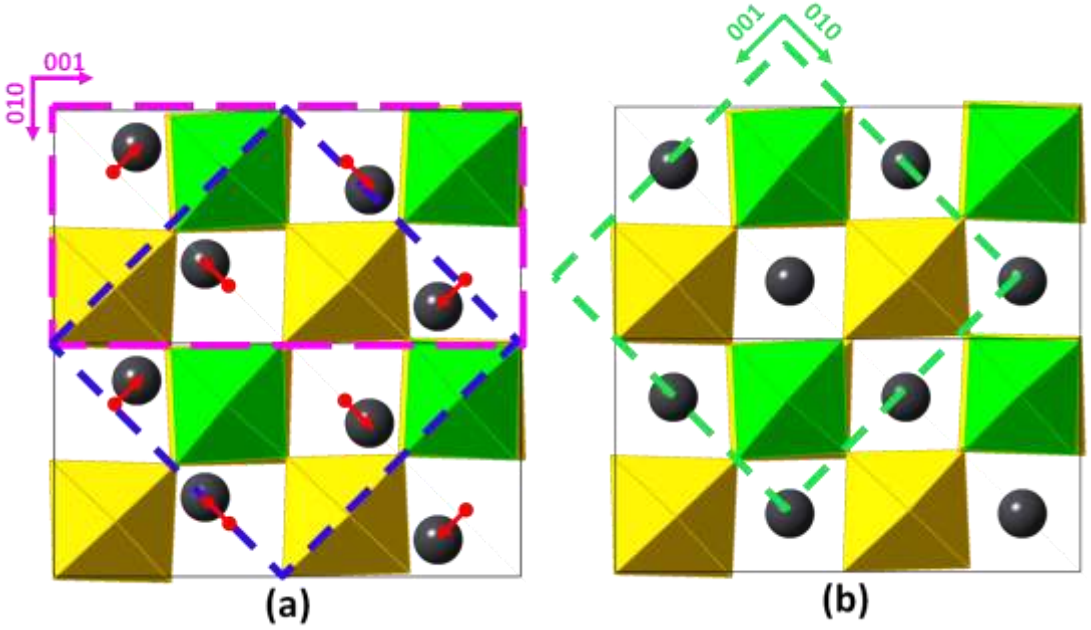

Figure 4.7 Schematic drawing of (1-x)Pb($Mg_{1/2}W_{1/2}$)O_3–xPb($Mn_{1/2}W_{1/2}$)O_3 unit cells with (a) 0≤x≤0.2 with *Pmcn* symmetry and (b) x≥0.4 with $\boldsymbol{Fm\bar{3}m}$ symmetry from (100) plane. W^{6+} and Mg^{2+}/Mn^{2+} ions are within green and yellow octahedrons respectively. Pb displacement was exaggerated with its direction indicated by red arrow. Red square represents the (100) single-perovskite-pseudocubic plan (in ABO_3 setting); Purple square represents orthorhombic (100) plane; Blue square represents $\boldsymbol{Fm\bar{3}m}$ double-perovskite-pseudocubic (100) plane (in $A_2B_2O_6$ setting)**.**

Fig. 4.8 shows the EPR spectra of (1-x)Pb($Mg_{1/2}W_{1/2}$)O_3–xPb($Mn_{1/2}W_{1/2}$)O_3 (x = 0.1 and 0.2) collected at room temperature. In each case a similar spectrum is observed with intensity centered around g = 2. This is consistent with high-spin Mn^{2+} (S = 5/2) centers, which in derivative-mode X-band EPR spectra typically shows a dominant M_S = ½ ↔ −½ transition. Further confirmation that these spectra arise from manganese centers is shown by hyperfine structure from the ^{55}Mn nucleus (I = 5/2, 100%) which gives a partially-resolved 6-line splitting. As shown in the insets of Fig. 4.8, these splittings can be seen clearly in the second derivatives of the spectra. In each case the spectra were simulated with the MATLAB-based simulation package EasySpin[108]. In each case, the spectra were simulated using numerical diagonalization of the full Hamiltonian matrix, however, the resulting parameters for a tetragonal symmetry system with S = 5/2 and I =

5/2 can be interpreted usefully in terms of the spin Hamiltonian using second-order perturbation theory, as follows[109]:

$$H = \mu_B B \hat{g} S + \mathrm{D}\left[S_z^2 - \frac{1}{3}S\,(S+1)\right] + \mathrm{I}\hat{A}\,, \qquad (4.2)$$

The first term in Equation (4.2) is the Zeeman interaction with the g factor in tensor form. μ_B is the Bohr magneton, and B is the applied magnetic field. The second term represents the fine structure where D is the axial zero-field splitting parameter which reflects the local structural distortion around the Mn^{2+} center. The third term is the hyperfine interaction between the unpaired electrons and the ^{55}Mn nucleus defined by the hyperfine interaction tensor, A. As shown in Fig. 4.8 the experimental spectra can be well simulated by including two components. The first (green curve in Fig. 4.8), with spin-Hamiltonian parameters shown in Table 4.1, is a comparatively narrow spectrum that can be simulated with uniaxial EPR parameters corresponding to the tetragonal symmetry of the local environment of the Mn^{2+} ions. The resolved hyperfine splitting of 90×10^{-4} cm^{-1} is consistent with previous reports of Mn^{2+} crystalline environments[110, 111]. Furthermore, although the relatively low resolution of the spectrum and absence of data from other spin manifolds make it difficult to accurately determine D, it is clear that zero-field splitting is relatively small.[110, 112] This suggests that the Mn^{2+} centres exhibit a low structural distortion and low off-center displacement, which is consistent with the XRD result. In addition to the signal described above, the EPR spectra also show a contribution from a broad, essentially isotropic spectral component (blue curve in Fig. 4.8). This was simulated with g = 2.0 and linewidth = 850 Gauss and added, with an appropriate weighting, to the resolved Mn^{2+} signal to give the final summed simulation (red curves in Fig. 4.8). The ratios of the resolved anisotropic:isotropic signal are similar at both Mn^{2+} concentrations: 0.65:1 for x=0.1 and 0.55:1 for x=0.2. These two types of spectral features have also been reported previously in the EPR studies of Mn^{2+} in MnO doped $Pb(Mg_{1/3}Nb_{2/3})O_3$[110]. Further EPR experiments at various temperatures is required to investigate the lattice dynamic properties. In general, the EPR parameters for x = 0.1 and x = 0.2 are identical (Table 4.1) except for their weighting factors. This demonstrates that although the overall lattice parameters and crystal symmetry evolve dramatically with different Mn-substitution levels, the bonding environment of the Mn-center is not significantly influenced.

Table 4.1 Anisotropic Spin-Hamiltonian parameters of Mn^{2+} ions in (1-x)$Pb(Mg_{1/2}W_{1/2})O_3$–x$Pb(Mn_{1/2}W_{1/2})O_3$ (x=0.1 and 0.2) (* in the unit of 10^{-4} cm^{-1}, linewidth in Gauss)

$g_{\perp}$	$g_{\parallel}$	$A^*_{\perp}$	$A^*_{\parallel}$	D^*	Linewidth$_{\perp}$	Linewidth$_{\parallel}$
1.99	1.95	8	90	51	100	440

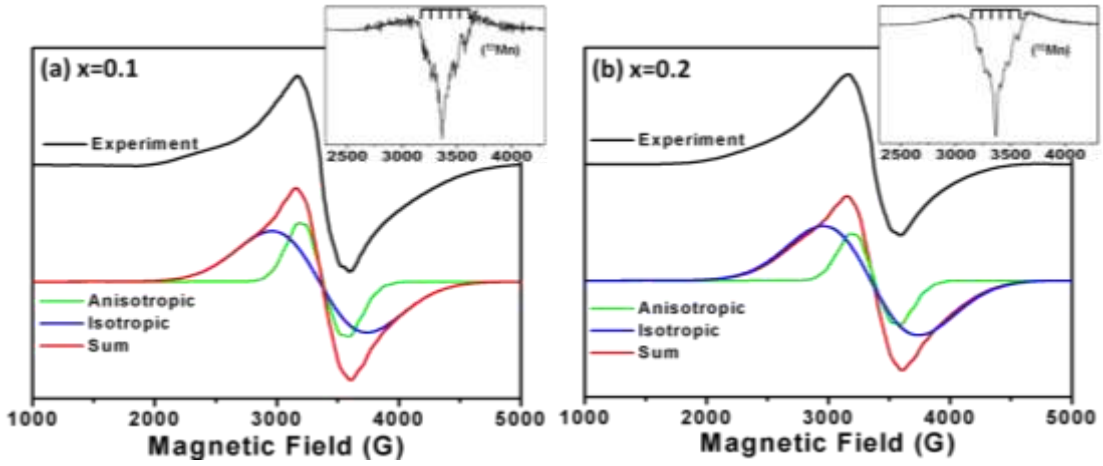

Figure 4.8 First derivative of EPR spectra for (a) x = 0.1 and (b) x = 0.2. Insets show the second derivative of the spectra with hyperfine peaks resolved. Simulations are carried out using axial symmetry and shown as the red lines, which are deconvoluted into anisotropic (blue) and isotropic (green) contributions.

The magnetic properties induced by the Mn^{2+} ion were measured by SQUID and the results are shown in Fig. 4.9. At high temperature, the χT value for 0.9$Pb(Mg_{1/2}W_{1/2})O_3$–0.1$Pb(Mn_{1/2}W_{1/2})O_3$ is around 4.15 $\mathrm{emu \cdot K \cdot mol^{-1}}$, which is consistent with the expected value for a high-spin S=5/2 Mn(II) centre. The sharp drop of χT below 20 K is possibly due to the combined effects of zero-field splitting and antiferromagnetic ordering of a Mn(II) center[113]. The fitting of the magnetic susceptibility to the Curie-Weiss law (plotted as red curve in Fig. 4.9):

$$\frac{1}{\chi} = \frac{T-\theta}{C}, \qquad (4.3)$$

gives rise to a Curie constant C = 4.176 $\mathrm{emu \cdot K \cdot mol^{-1}}$ and a paramagnetic Curie temperature θ = -2.33K, indicating a mainly paramagnetic behavior with possible existence of antiferromagnetic interaction. The effective paramagnetic moment calculated from the Curie constant is 5.78 μB/f.u. which is close to the value expected from the spin-only moment of Mn^{2+} ion (5.9 μB/f.u.). No ferromagnetic behavior is observed in the magnetization-field measurements carried out at 5 K, which just shows a single non-linear curve (Inset, Fig. 4.9). This confirms that the Mn^{2+} ion mainly exits in a paramagnetic state with possible antiferromagnetic interaction. As shown in Fig. 4.7, there exists strong 1:1 ordering between the Mn^{2+}/Mg^{2+} and W^{6+} ions. In addition, since Mn^{2+} is the only ion that has unpaired electrons in partially filled *d*-orbitals, no magnetic exchange interaction is expected from Mn^{2+}—O^{2-}—W^{6+} chains. Therefore, it is possible that the weak antiferromagnetic coupling originates from the local chemically disordered region or at the grain boundaries, where the formation of Mn^{2+}—O^{2}—Mn^{2+} chains leads to antiferromagnetic superexchange[114].

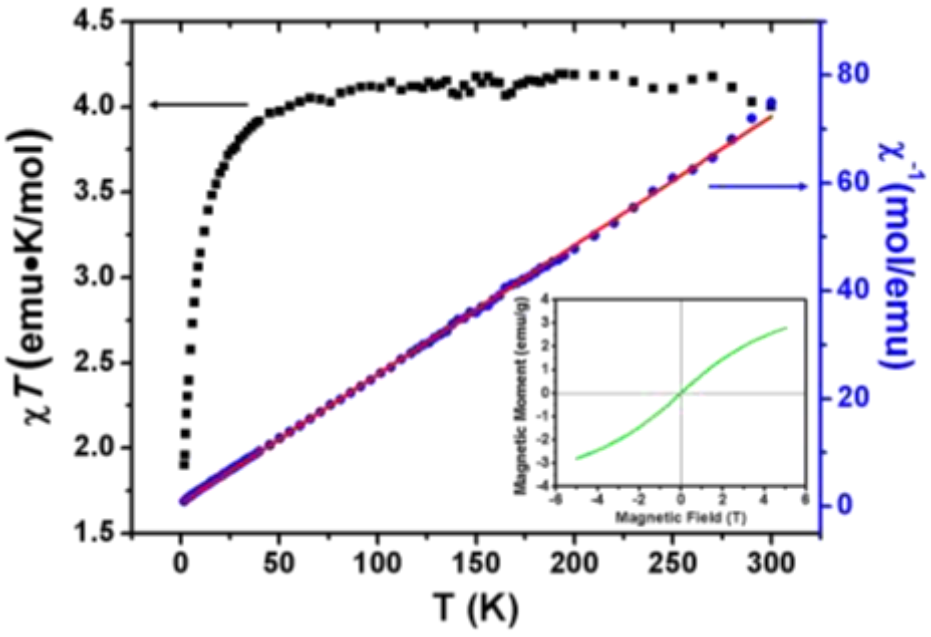

Figure 4.9 Temperature dependences of χT and 1/χ for $0.9Pb(Mg_{1/2}W_{1/2})O_3$–$0.1Pb(Mn_{1/2}W_{1/2})O_3$. Red line represents the linear fit of 1/χ vs. T to the Curie Weiss law. Magnetic hysteresis measurement for the same sample at 5K is shown as the inset.

Fig. 4.10 shows the fracture micrographs of the (1-x)$Pb(Mg_{1/2}W_{1/2})O_3$–x$Pb(Mn_{1/2}W_{1/2})O_3$ ceramics of various compositions imaged by SEM. The ceramics with x = 0, 0.1 and 0.2 are selected based on their tolerance to high sintering temperature. These three ceramics prepared under the identical sintering conditions (1100 ˚C for 2 hours) exhibit a significant increase in grain size with the addition of $Pb(Mn_{1/2}W_{1/2})O_3$, from < 1 μm in pure $Pb(Mg_{1/2}W_{1/2})O_3$ to ~10 μm in 0.8$Pb(Mg_{1/2}W_{1/2})O_3$–0.2$Pb(Mn_{1/2}W_{1/2})O_3$. The enhanced grain growth is possibly caused by a transient liquid phase formed from some intermediate phases with relatively low melting points such as Pb_2WO_5 (m.p. 935 ˚C) and $PbWO_4$ (m.p. 1123 ˚C), in addition to the reagents such as PbO (m.p. 888 ˚C)[115]. The mixture of these compounds creates a liquid phase through eutectic reactions, favoring the grain growth[116, 117]. The existence of a liquid phase was also observed in other solid solution systems that contain Pb- and W-based compounds, such as in $Pb(Zn_{1/2}W_{1/2})O_3$-$Pb(Zr_{0.5}Ti_{0.5})O_3$[118], $Pb(Mg_{1/2}W_{1/2})O_3$-$PbTiO_3$[119] and $Pb(Fe_{2/3}W_{1/3})O_3$[120]. Our recent report[121, 122] also demonstrate the beneficial effects on the sintering of Pb-W compounds such as the 0.99$PbZrO_3$-0.01$Pb(Mg_{1/2}W_{1/2})O_3$, 0.99$PbZrO_3$-0.01$Pb(Zn_{1/2}W_{1/2})O_3$ and $PbZrO_3$-$Pb(Mn_{1/2}W_{1/2})O_3$ ceramics, which were prepared under the similar conditions. It is worth mentioning that although previous attempt at the synthesis of $Pb(Mn_{1/2}W_{1/2})O_3$ by conventional solid state reaction in Ar stream led to positive results, in our experiment, no trace of perovksite phase can be obtained under the same conditions except the presence of Ar stream. Therefore, the role of Ar atmosphere in the formation of perovskite structure seems to be critical, but still unclear. Nevertheless, it can be expected that the low chemical stability of $Pb(Mn_{1/2}W_{1/2})O_3$ facilitates the formation of the transient liquid phases. Analysis of XRD patterns also supports this argument as $PbWO_4$ phase starts to appear at x=0.5, indicating the solubility limit being reached.

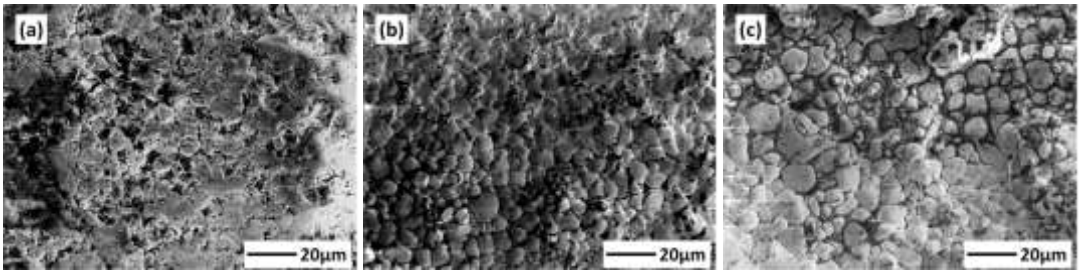

Figure 4.10 SEM images of the (1-x)Pb($Mg_{1/2}W_{1/2}$)O_3–xPb($Mn_{1/2}W_{1/2}$)O_3 ceramics with (a) x=0, (b) x= 0.1 and (c) x=0.2, sintered at 1000 ˚C for 2 hours

The variation of the dielectric constant (ε') as a function of temperature for the (1-x)Pb($Mg_{1/2}W_{1/2}$)O_3–xPb($Mn_{1/2}W_{1/2}$)O_3 ceramics measured at 10^5 Hz is shown in Fig. 4.11 (a). Only the data of 10^5 Hz are presented here since no frequency dispersion is observed. The dielectric constants values are normalized by zeroing the minimal value (i.e. at -50 ˚C) in each curve in order to emphasize the effects of composition. In all the compositions studied, an antiferroelectric (AFE) to paraelectric (PE) phase transition takes place upon heating as revealed by the peaks in the dielectric curves. It is interesting to note the trend for the variation of the AFE-PE phase transition temperature T_C. T_C first increases from 40.2 ˚C for x=0 to 46.5 ˚C for x=0.2, but then drastically decreases to 31.5 ˚C for x=0.25 where the cubic $Fm\bar{3}m$ phase starts to appear. It continues to decrease to 30.3 ˚C for x=0.3 and to 16.5 ˚C for x=0.4. For x=0.4, as T_C (16.5 ˚C) is already below room temperature, the XRD pattern for this composition recorded at room temperature indeed shows a cubic $Fm\bar{3}m$ structure (Fig. 4.6). The phase transition for x=0.5 becomes diffused so that no accurate T_C value can be obtained. Based on the XRD data and dielectric measurements, a phase diagram is proposed for (1-x)Pb($Mg_{1/2}W_{1/2}$)O_3-xPb($Mn_{1/2}W_{1/2}$)O_3 as shown in Fig. 4.11 (b) where a curved phase boundary is drawn between the AFE and PE phases for 0≤x≤0.5, showing the composition-induced transition from the AFE to the PE phase at x ≈ 0.35 at room temperature. The decrease of T_C with increasing Mn^{2+} concentration for x≥0.2 indicate a decrease of antiferroelectricvity which is consistent with the decrease of Pb^{2+} displacement [Fig. 4.6 (c)]. However, with x increasing from 0 to 0.2, T_C slightly increases despite the fact that Pb^{2+} displacement remains constant (or decreases slightly). The detailed mechanism for this increase is still unclear.

Note that, our results show some discrepancies with the previous work by Barbur *et al*. on the synthesis and characterization of the same solid solution[123, 124]. In their experiments, calcinations were carried out directly with a mixture of PbO, H_2WO_4, $Mg(NO_3)_2 \cdot 6H_2O$ and $MnCO_3$ reagents instead of by the precursor method. They claimed that solid solution system remained in the AFE orthorhombic phase up to $x \geq 0.5$. However, no XRD structural analysis was presented to support this claim. Whereas in the present work, a composition-induced phase transition from the AFE orthorhombic to the PE cubic phase is found to take place at $x \approx 0.35$ at room temperature and a phase boundary is between the AFE and PE phases. In addition, an opposite trend of T_C as a function of composition x was also observed. In their experiments, the T_C increased linearly with the increase of x whereas in our study the T_C slightly increases from x=0 to 0.2 and decreases from x>0.2. Such significant discrepancies may be attributed to the different preparation methods used in the present work in which the formation of $MgWO_4$ and $MnWO_4$ precursors favors the ordering between B-site (Mg^{2+}/Mn^{2+}) and B'-site (W^{6+}) ions in the perovskite structure whereas the direct calcinations of powder mixture tends to create chemical disorder between B/B'-site ions and to generate secondary phases such as Pb_2WO_5 or $PbWO_4$. It is worth to mention that in our previous study on Mn^{2+}-doped PIN-PMN-PT ferroelectric solid solutions, T_C for FE→PE phase transition also shows a decreasing trend with the increase of Mn-doping concentration[125]. It seems that Mn^{2+} ion tends to reduce the Pb-displacement in either ferroelectric or antiferroelectric systems and favors cubic structure in Pb-based perovskites.

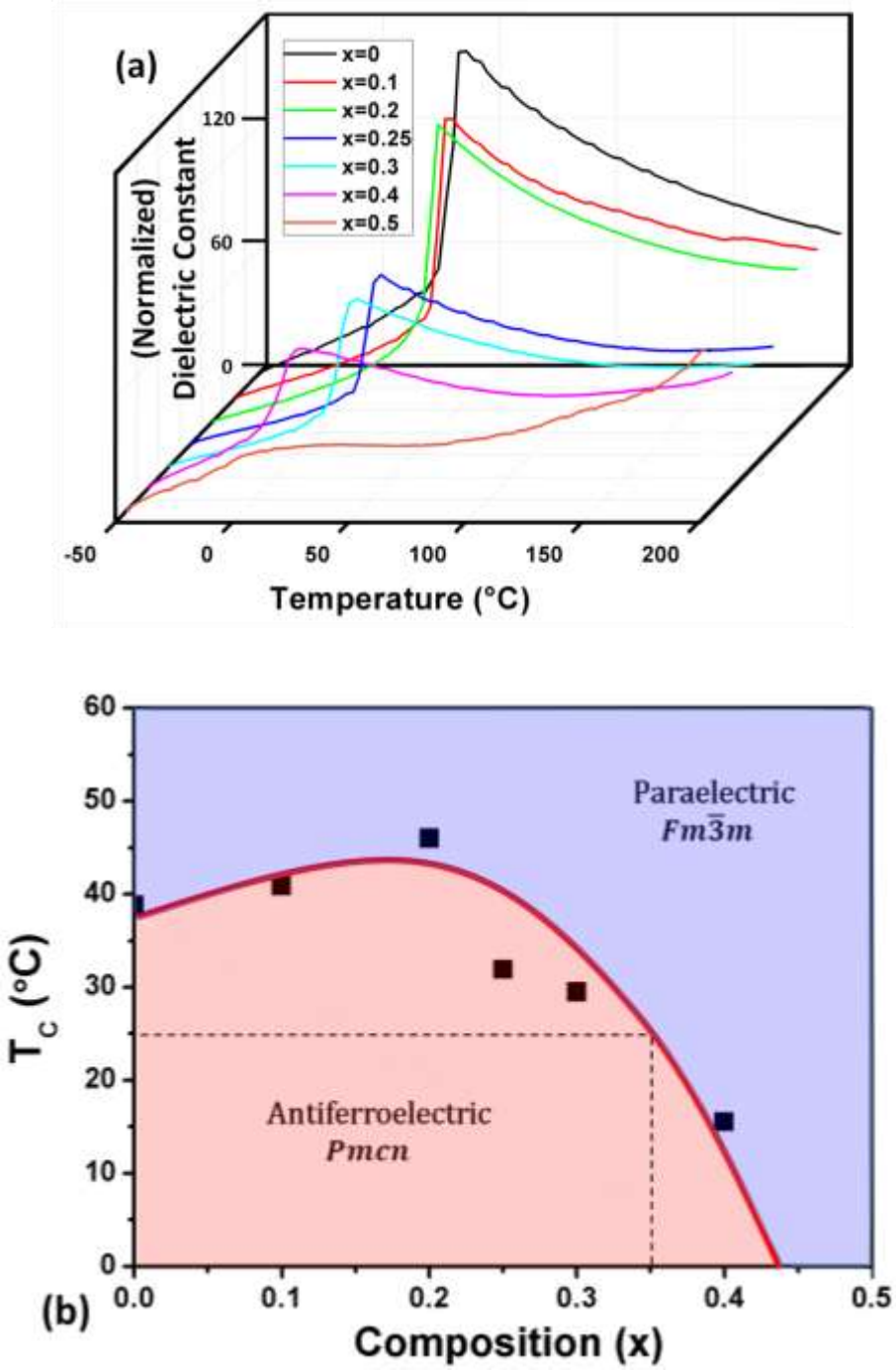

Figure 4.11 (a) Temperature dependence of dielectric constant (ε') of the (1-x)Pb($Mg_{1/2}W_{1/2}$)O_3–xPb($Mn_{1/2}W_{1/2}$)O_3 ceramics measured at 10^5 Hz. (b) Partial phase diagram for this solid solution system established based on the XRD data and dielectric measurements, (red curve is for eye-guide). The dashed lines indicate the composition-induced *Pmcn* → $Fm\bar{3}m$ phase transition occurring at x≈0.35 at room temperature

4.5. Conclusion

New antiferroelectric solid solutions of (1-x)$Pb(Mg_{1/2}W_{1/2})O_3$ - x$Pb(M_{1/2}W_{1/2})O_3$ (M = Zn and Mn) were successfully synthesized by solid state reaction in the form of ceramics, which were sintered at relatively low temperatures. The solubility of $Pb(Zn_{1/2}W_{1/2})O_3$ into the PMW perovskite structure reaches 30% in the solid solution. The antiferroelectric to paraelectric phase transition was revealed by dielectric anomalies at T_C which increases as with increasing PZW concentration, from 40.8 ˚C (x = 0) to 67.9 ˚C (x = 30%), indicting an enhancement of the antiferroelectric order as a result of the PZW substitution for PMW. Polarization - field variation exhibits a nearly linear relation with a very weak hysteresis up to a high electric field of 125 kV/cm, indicating a high dielectric strength. The antiferroelectric PMW-PZW ceramics with low processing temperature, low dielectric constant, low dielectric loss and high dielectric strength at room temperature make it potentially useful as ceramic insulators.

The solid solution of complex perovskite (1-x)$Pb(Mg_{1/2}W_{1/2})O_3$ - x$Pb(Mn_{1/2}W_{1/2})O_3$ has also been synthesized by a precursor-based 2-step solid-state reaction method. XRD measurements at room temperature confirm that the system crystallizes in an orthorhombic *Pmcn* antiferroelectric phase with a low concentration of Mn^{2+} (x≤0.35) and undergoes a phase transition from the $Pmcn$ to a cubic $Fm\bar{3}m$ phase where x is increased to 0.35. The displacements of Pb^{2+} ion along both the *y*-and *z*-direction decreases, indicating a reduced antiferroelectricity with the increase of x. EPR spectroscopy shows that Mn adopts 2+ oxidation state with high-spin (S = 5/2), which is confirmed by magnetic measurement by SQUID. The simulation and analysis of the EPR spectrum indicates that the Mn^{2+} ion is in the center of a slightly distorted oxygen octahedron with tetragonal symmetry. The grain size of the solid solution ceramics is significantly enlarged by the formation of transient eutectic liquid phases arising from the Pb/W-based oxides. Dielectric measurement reveals the T_C of AFE-PE phase transition first increases slightly with increasing x until x=0.2, then decreases significantly at x>0.2. The decrease of T_C at x>0.2 is interpreted as a weakening of the AFE order, which is caused by the reduced Pb^{2+}-displacements whereas the cause of the increase in T_C at x≤0.2 is still unclear. Based on the T_C values from the dielectric measurements, a partial phase diagram of the solid solution is proposed which delimits the orthorhombic

antiferroelectric *Pmcn* phase from the cubic paraelectric $Fm\bar{3}m$ phase. It also shows the composition induced *Pmcn* → $Fm\bar{3}m$ phase transition, consistent with the structural analysis by XRD. Combined wtih our previous study on Mn-doped PIN-PMN-PT ferroelectric solid solution, this work provides a deeper insight for the behavior of Mn^{2+} ion in Pb-based perovskites and a guideline for the design of Mn^{2+}-containing anti/ferroelectric functional material in the future.

Chapter 5: Study of $PbZrO_3$-$Pb(Mn_{1/2}W_{1/2})O_3$ Soft Antiferroelectric Ceramic System

Part of this chapter is revised from the paper published by Z. Ren, N. Zhang, L.-W. Su, H. Wu, and Z.-G Ye Ye in *J. Appl. Phys.* **116**, 024103 (2014). The use of the article is permitted by the publisher of *American Institute of Physics*

5.1. Abstract

A new solid solution of complex perovksite structure, (1-x)$PbZrO_3$-x$Pb(Mn_{1/2}W_{1/2})O_3$(PZ-xPMnW, with x = 0 - 0.1), is prepared by the solid state reaction method. Its crystal structure, dielectric properties and antiferroelectricity are investigated. It is found that the crystal structure of the solid solution remains in the orthorhombic *Pbam* symmetry with $x \leq 0.1$. The induced polarization (P_{Ind}) is enhanced, whereas the critical field (E_{Cr}) is decreased, with increasing PMnW concentration, indicating the softening of antiferroelectricity in PZ. The Curie temperature (T_C) is also decreased with the substitution of PMnW for PZ. The grain size is significantly enlarged, which could be attributed to the presence of a transient liquid phase during the sintering process. Measurements of the magnetization by means of SQUID confirm that the Mn ion exists in a high spin state with a 2+ oxidation state. The softening of antiferroelectric order and the improvement in induced polarization make the PZ-PMnW ceramics an interesting material system for such applications as energy storage devices.

5.2. Introduction

Antiferroelectricity was first predicted by Kittel in 1951. It is similar to ferroelectricity whereas the spontaneous electric dipole lies in antiparallel directions. As a result, no net polarization is displayed within antiferroelectric material. $PbZrO_3$ is one of the most

widely studied antiferroelectric materials, in which the antiferroelectricity originates from the spontaneous antiparallel displacement of Pb^{2+} ions. At room temperature $PbZrO_3$ adopts an orthorhombic structure with *Pbam* symmetry[21, 25]. The antiparallel displacement of Pb^{2+} ions vanishes at above Curie temperature (236 °C[22, 126]), changing the symmetry of $PbZrO_3$ into $Pm\bar{3}m$. When $PbZrO_3$ is subject to the electric field, the antiparallel dipoles are switched to the same direction, displaying the double hysteretic behavior as a result of electric-field-induced antiferroelectric (AFE) - ferroelectric (FE) phase transition[6]. Previous experiments on $PbZrO_3$-based antiferroelectric materials also found that the electric field will align the displacement of Pb^{2+} ions in the same direction and therefore constitutes a structural phase transition from orthorhombic/tetragonal into rhombohedral symmetry[127, 128, 129, 130]. With nature of AFE←→FE phase transition, $PbZrO_3$-basedantiferroelectric materials provide potential engineering applications in digital displacement transducers, charge storage device and high strain actuators[12, 131, 132].

However, pure $PbZrO_3$ has a very high threshold field for AFE→FE phase transition which will lead to dielectric breakdown before the phase transition takes place. In order to observe the field-induced AFE-FE phase transition phenomenon before dielectric breakdown occurs, chemical modification is required to reduce the critical field for polarization switching to take place. It was shown that the most effective way of lowering the critical field is by doping/substituting Zr^{4+} with La^{3+}, Ti^{4+}, Nb^{5+}, Sn^{4+} and Hf^{4+}[12, 28, 128, 131, 132] ions in $PbZrO_3$. La^{3+} doping experiment conducted by Brodeur[133] was demonstrated to be an effective way to enhance the room temperature permittivity, maximum induced polarization and the ceramic density. Nb^{5+}-doping in $PbZrO_3$ can generate intrinsic Pb-vacancies which will stabilize the ferroelectric intermediate phase[134]. Substitution of Zr^{4+} with Sn^{4+} can lead to the increase of antiferroelectric Curie temperature and decrease of AFE→FE threshold field[12, 130, 135].

In this chapter, a novel approach was chosen to achieve the softening of antiferroelectric material by partially substitute $Pb(Mn_{1/2}W_{1/2})O_3$ for $PbZrO_3$ to form (1-x)$PbZrO_3$-x$Pb(Mn_{1/2}W_{1/2})O_3$ solid solution. Single phase $Pb(Mn_{1/2}W_{1/2})O_3$ has not been synthesized in the perovskite structure by conventional solid state reaction method. It was reported that $Pb(Mn_{1/2}W_{1/2})O_3$ with perovskite phase has only been synthesized under Ar atmosphere[103, 104]. The $Pb(Mn_{1/2}W_{1/2})O_3$ has the same symmetry as $Pb(Mg_{1/2}W_{1/2})O_3$[18]

with the space group *Pmcn*[20] (the $2_1/m$ $2_1/c$ $2_1/n$ symmetry elements in *Pmcn* is equivalent to the $2_1/n$ $2_1/m$ $2_1/a$ symmetry elements in *Pnma*[103]) with the substitution of Mn^{2+} ion into the position of Mg^{2+} ion. For $Pb(Mg_{1/2}W_{1/2})O_3$ or $Pb(Mn_{1/2}W_{1/2})O_3$, the Pb^{2+} ions displace towards $[100]_{pc}$ and $[010]_{pc}$ (pseudocubic setting) direction compared $PbZrO_3$ in which Pb^{2+} ions shift towards $[110]_{pc}$ direction. The solid solution of (1-x)$PbZrO_3$- x$Pb(Mg_{1/2}W_{1/2})O_3$ was synthesized and characterized by Vittayakorn*et al*.[136]. In their experiment, a ferroelectric phase was induced by the addition of $Pb(Mg_{1/2}W_{1/2})O_3$ up to x = 0.1. In addition, Antiferroelectric-Ferroelectric-Paraelectric phase transition sequence was observed in the composition range from x=0.02 to 0.1. According to the study of Viehland*et al.*[137], the dipole frustration originated from the competition between ferroelectric and antiferroelectric ordering can be the cause of incommensurate modulation. This incommensurate structure is strongly related to the softening of antiferroelectricity in the material as the field-induced ferroelectric phase can be stabilized. Therefore, most previous studies[27, 131, 132, 138, 139] are focused on the substitution of Zr^{4+} with Ti^{4+} because $PbTiO_3$is known to be highly ferroelectrically active in perovskite structure[37, 140]. In this paper, an alternative approach was taken by substituting $Pb(Mn_{1/2}W_{1/2})O_3$ for $PbZrO_3$ to form the solid solution of $PbZrO_3$-$Pb(Mn_{1/2}W_{1/2})O_3$. With the large difference in oxidation state and ionic size between B-site (Mn^{2+} 0.83Å)and B'-site (W^{6+} 0.6Å)ions[1], it is highly possible that the local B/B'-site ordering can be retained within the solid solution. Therefore, it is reasonable to expect that $Pb(Mn_{1/2}W_{1/2})O_3$ shall play a similar role to$Pb(Mg_{1/2}W_{1/2})O_3$ as the source of dipole frustration when forming solid solutions with $PbZrO_3$.

5.3. Experiment

The solid solution of (1-x)$PbZrO_3$ - x$Pb(Mn_{1/2}W_{1/2})O_3$(PZ-PMnW) with x up to 10% was prepared by a two-step solid state reaction method introduced by Swartz and Shrout[58]. The $MnWO_4$ precursor phase was first synthesized from WO_3 and $MnCO_3$ powder (purity >99%) at 1000 ˚C for 12 hours. This approach ensures that 1:1 ordering between Mn^{2+} and W^{6+} in the perovskite phase suppresses the formation of secondary phases such as $PbWO_4$ or Pb_2WO_5. In the second step, the pre-formed precursor was mixed stoichiometrically with PbO and ZrO_2, ground and calcined at 850 ˚C for 4 hours to obtain the powder of pure perovskite phase. An excess of 0.5-1% (mol percent) of PbO

was added in this step to compensate the lead oxide evaporation at high sintering temperatures. The calcined samples were then ground into fine powder and pressed into pellets for sintering. The sintering process took place at temperatures varying from 1200 to 1260 °C for 2 to 2.5 hours, which led to dense ceramics. X-ray powder diffraction was performed by Bruker D8 diffractometer, with Cu Kα1 radiation (λ = 1.5405 Å) to examine the phase purity and to determine the crystal structure. The temperature dependence of the dielectric permittivity of the ceramics was measured on a *Novocontrol* broadband dielectric analyzer from 0 to 300 °C at varying frequencies. The polarization-electric field relationship was displayed by an RT-66 ferroelectric test system (Radian Technology). The ceramic surface morphology was imaged with a Strata235 Dual Beam SEM. Magnetic measurements were performed using a Quantum Design MPMS-XL-7S SQUID magnetometer.

5.4. Result and Discussion

5.4.1. Electrical properties in antiferroelectric phase

The X-ray diffraction pattern of the PZ-PMW solid solution is shown in Fig. 5.1 (a). The refinements of the major diffraction peaks indicate that the solid solution system crystallizes in a single phase orthorhombic $Pbam$ symmetry for 0≤x≤0.1. No sign of *Pmcn* symmetry is found in the entire composition range. Due to the similarity of the ionic radii of Zr^{4+}(0.72Å), Mn^{2+}(0.83Å) and W^{6+}(0.6Å)[1], it is reasonable to expect that the Mn^{2+} and W^{6+} ions have substituted the Zr^{4+} ion on the B-site in the solid solution. For a better visualization of the superlattice, the orthorhombic $\sqrt{2}\,a \times 2\sqrt{2}a \times 2a$ lattice is converted into the pseudocubic $a \times a \times a$ lattice setting (a = cell dimension of paraelectric cubic phase) by the following matrix:

$$(h_o \quad k_o \quad l_o)\begin{pmatrix} 1/2 & -1/2 & 0 \\ 1/4 & 1/4 & 0 \\ 0 & 0 & 1/2 \end{pmatrix} = (h_{pc} \quad k_{pc} \quad l_{pc}), \tag{5.1}$$

It has been shown that the Pb^{2+} displacements in the antiferroelectric phase of $PbZrO_3$ are associated with wave vector q_{Σ} = (1/4 1/4 0) in unit of 2π/a[13, 23].Therefore, by examining the evolution of Σ-type (1/4 1/4 0) reflection or P-type (1/4 1/4 1/2) reflection

(since $q_P = q_\Sigma + q_R$), the degree of ordering for Pb^{2+} ions can be estimated. Fig. 1(b) shows selected superlattice reflections presented in a normalized x-ray diffraction pattern. The intensity of $\frac{1}{4}(hkl)$ peaks shows a decreasing trend as x increases, indicating that the antiparallel Pb^{2+}-ordering is disrupted. Such a phenomenon is consistent with our speculation on dipole frustration model.

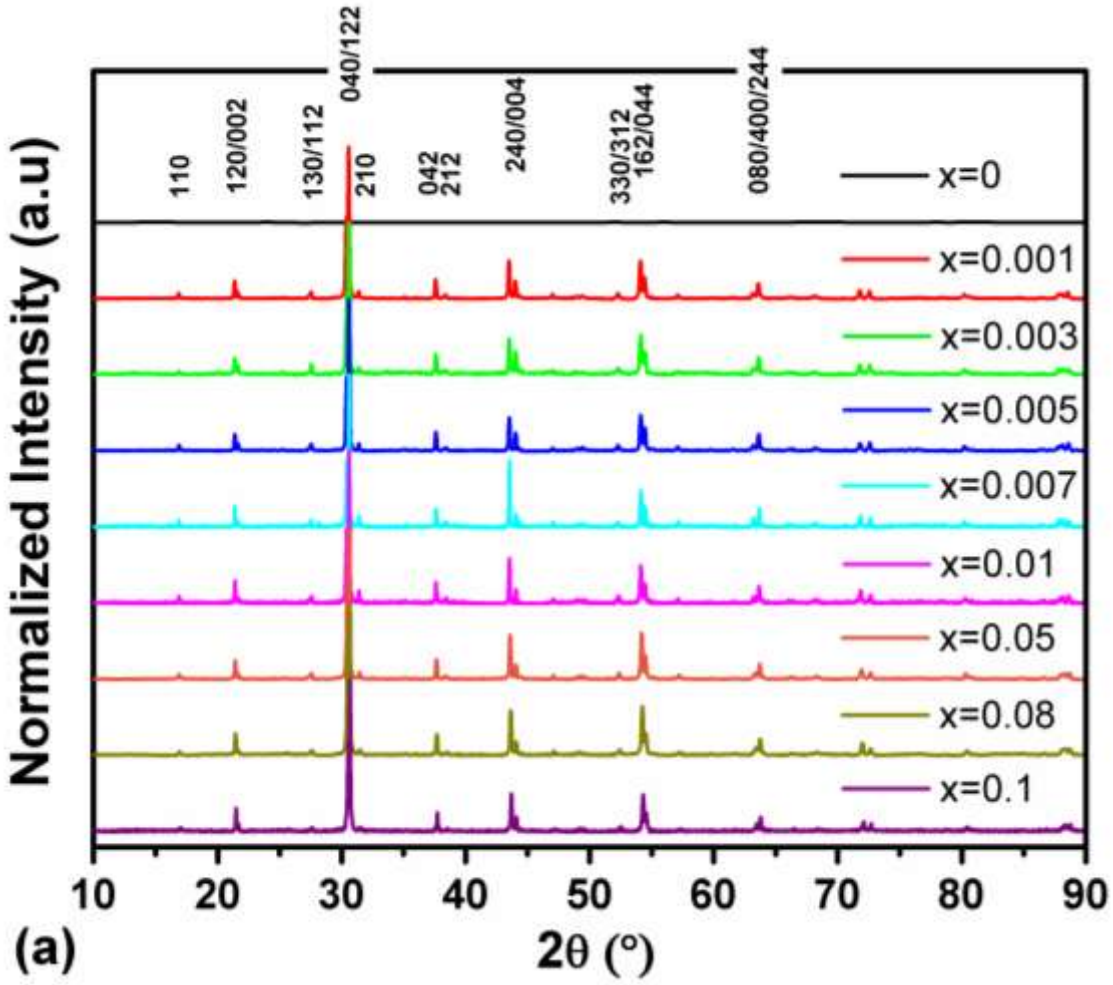

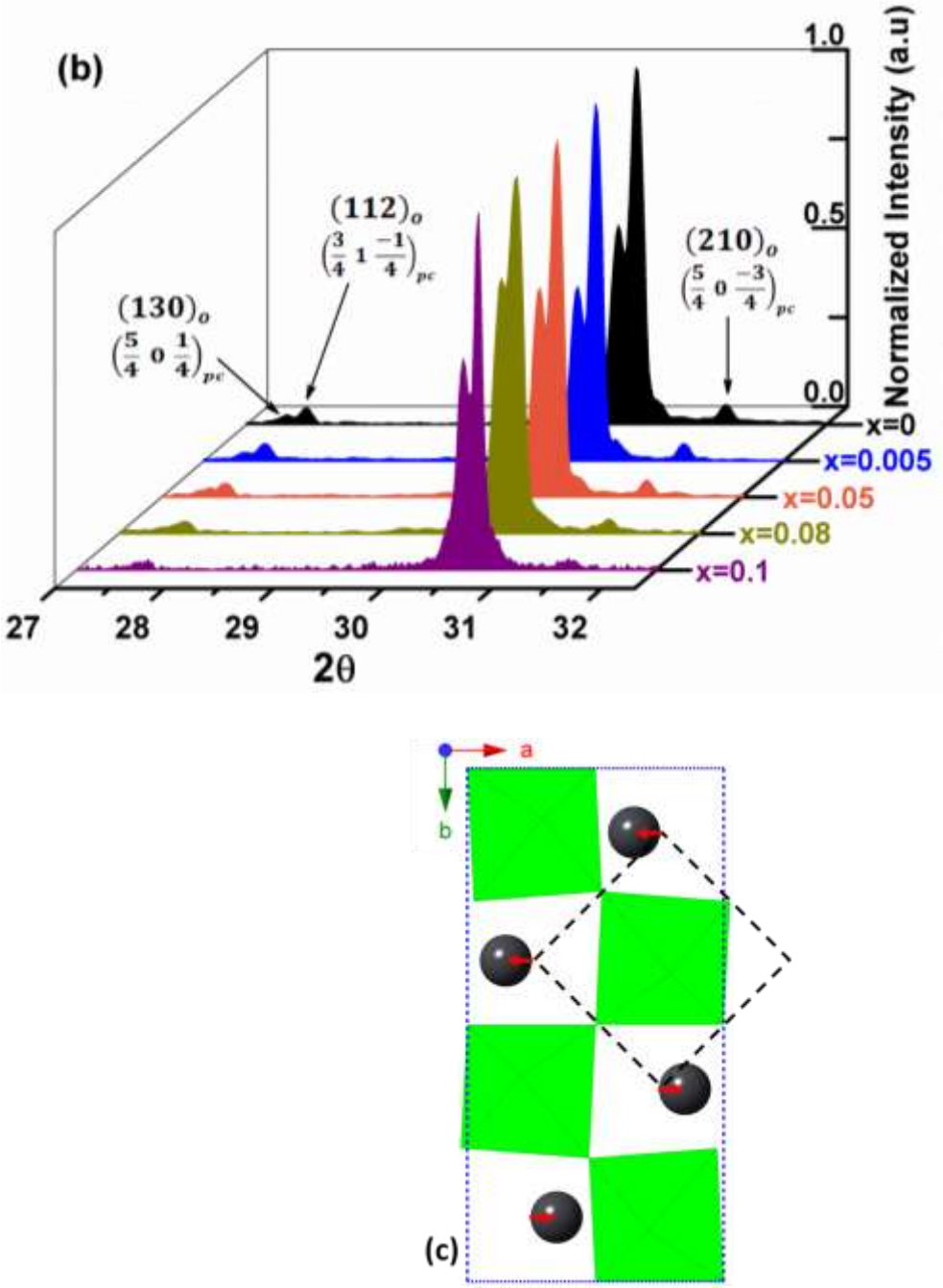

Figure 5.1 (a) XRD pattern of (1-x)$PbZrO_3$–x$Pb(Mn_{1/2}W_{1/2})O_3$. Peaks are labeled in orthorhombic setting. (b) Enlarged view of some $\frac{1}{4}$(h k l) superlattice peaks for selected compositions in both orthorhombic (o) and pseudocubic (pc) settings (c) Schematic drawing of the orthorhombic (dashed blue) and pseudocubic (dashed black) unit cells with the direction of Pb^{2+} displacement indicated by red arrows**.**

Fig. 5.2 shows the surface micrographs of the PZ-PMW ceramics of various compositions imaged by SEM. The ceramics prepared under the same sintering conditions (1260 ˚C for 2 hours) exhibit a significant increase in grain size with the addition of $Pb(Mn_{1/2}W_{1/2})O_3$, from <1 μm in pure PZ to ~10 μm in PZ-0.1PMW. The enhanced grain growth is possibly caused by a transient liquid phase formed from some intermediate phases with low melting points such as Pb_2WO_5 (m.p. 935 ˚C) and $PbWO_4$ (m.p. 1123 ˚C), in addition to the reagents such as PbO (m.p. 888 ˚C)[115].The mixture of these compounds could create a liquid phase through the eutectic reactions, which enhances the grain growth and thereby increases the ceramic density[116, 117]. The existence of the liquid phase was also observed in other solid solution systems that contain Pb- and W-based compound, such as in the $Pb(Zn_{1/2}W_{1/2})O_3$-$Pb(Zr_{0.5}Ti_{0.5})O_3$[118],$Pb(Mg_{1/2}W_{1/2})O_3$-$PbTiO_3$[119] and $Pb(Fe_{2/3}W_{1/3})O_3$[120] systems. Our recent work also demonstrate the beneficial effect of Pb-W compound in $0.99PbZrO_3$-$0.01Pb(Mg_{1/2}W_{1/2})O_3$ and $0.99PbZrO_3$-$0.01Pb(Zn_{1/2}W_{1/2})O_3$ ceramics, which were prepared under the same conditions: grain size of both ceramics increases significantly compared with the $PbZrO_3$ ceramic.

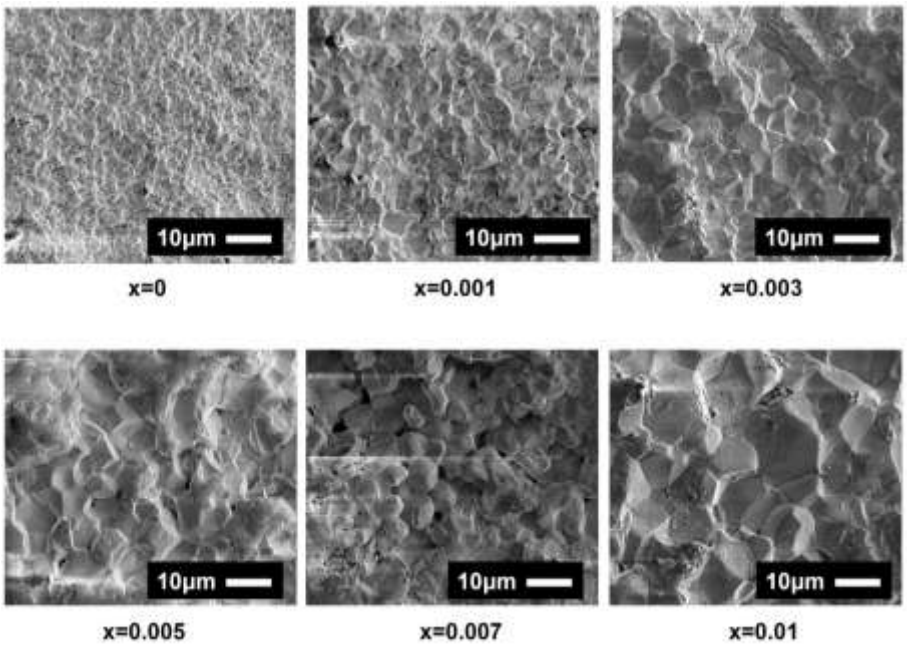

Figure 5.2 SEM images of $(1-x)PbZrO_3$-$xPb(Mn_{1/2}W_{1/2})O_3$ ceramics with 0≤x≤0.01 sintered at 1000 ˚C for 2 hours

The variations of polarization as a function of bipolar electric fields for the series of ceramics were measured at 150 ˚C, as shown in Fig. 5.3 (a). At room temperature, an external field up to 100 kV/cm was not enough to switch the dipoles. Therefore, it was necessary to heat the sample in order to induce the AFE-FE phase transition. The double hysteresis loops displayed in Fig. 5.3 (a) confirm the antiferroelectric property of the (1-x)$PbZrO_3$–x$Pb(Mn_{1/2}W_{1/2})O_3$ solid solution. The critical field E_{Cr} was assessed based on the average of the AFE-FE transition fields (E_{A-F}) and the FE-AFE transition fields (E_{F-A}) and its variation as a function of composition is shown in Fig. 5.3 (b). It can be seen that E_{Cr} is significantly reduced with the increase of PMW concentration, suggesting the enhanced stabilization of the metastable ferroelectric phase in the presence of $Pb(Mn_{1/2}W_{1/2})O_3$. In addition, the maximum induced polarization (P_{Ind}) is also enhanced with the increasing substitution level of $Pb(Mn_{1/2}W_{1/2})O_3$. It is generally believed that the thicker 180˚ domain walls formed in chemically modified $PbZrO_3$ antiferroelectrics are responsible for facilitating the dipole switching compared with the prototype $PbZrO_3$ phase which has only two layers of $[110]_{pc}$ in the 180 domain walls[130]. It was also illustrated in previous research that the mechanism behind the change in E_{Cr} for antiferroelectric material can be strongly related to the subgrain level hierarchical microstructure[26]. Therefore, in order to obtain more direct structural mechanism underlying the lowering of E_{Cr} and the enhancement in P_{Ind}, detailed information on nanoscale 90˚/180˚ domain structure shall be obtained by high-resolution transmission electron microscopy (HRTEM) in the future.

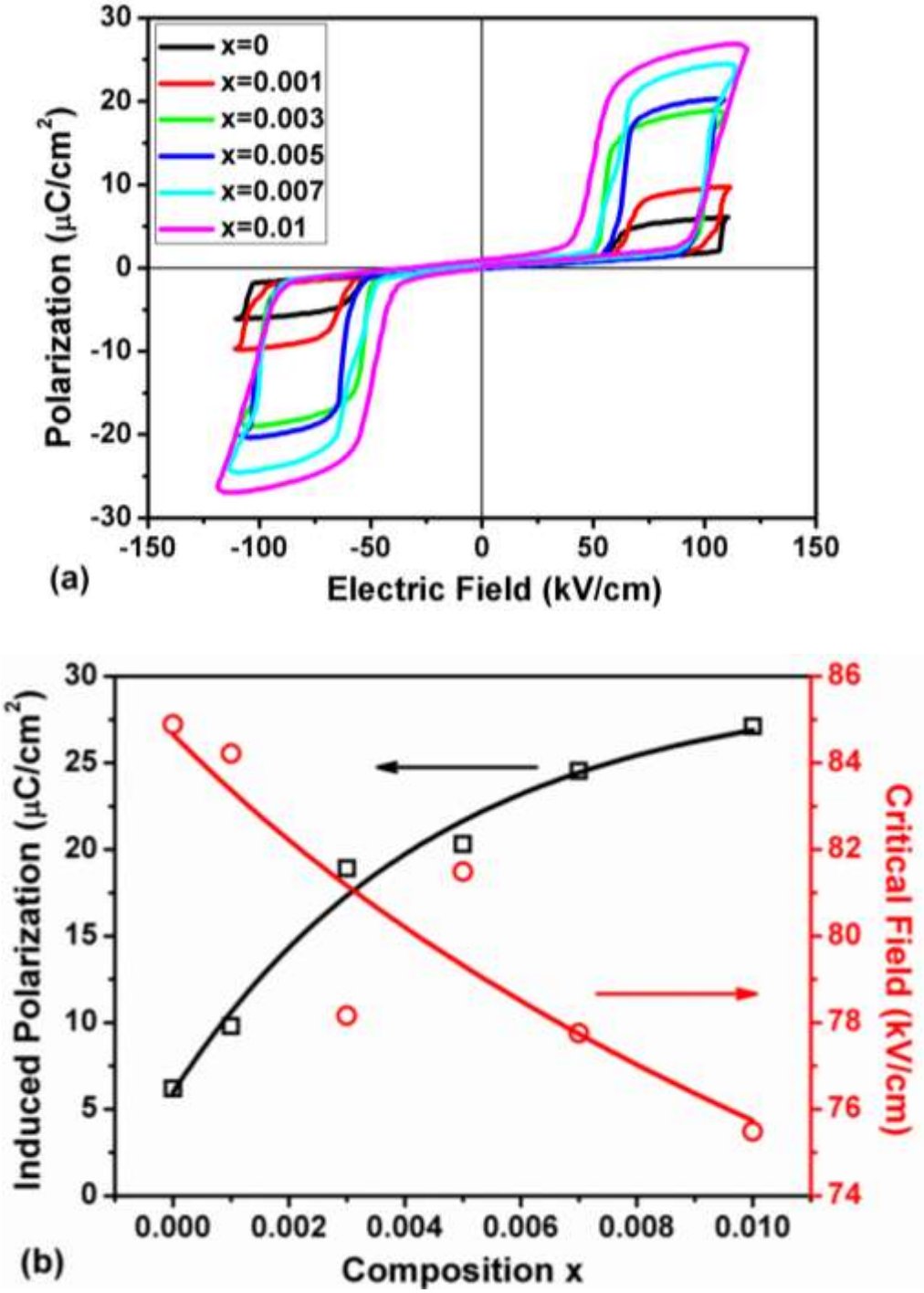

Figure 5.3 (a) Polarization-electric field relation for the (1-x)$PbZrO_3$-x$Pb(Mn_{1/2}W_{1/2})O_3$ system with x = 0 - 0.01 measured at 150 ˚C. (b) Variations of the critical field and induced polarization as the function of composition

The magnetic properties induced by the Mn^{2+} were measured by SQUID and the results are shown in Fig. 5.4 (a). At high temperature, the χT value for $0.09PbZrO_3$-$0.01Pb(Mn_{1/2}W_{1/2})O_3$ is approximately 4.19 emu K mol^{-1}, which is consistent with a high-spin S=5/2 Mn(II) centre.The sharp drop of χT value below 20 K is possibly due to the combination of zero-field-splitting and antiferromagnetic effect[113]. The fitting to the Cuie-Weiss law [red curve in Fig. 5.4 (a)]

$$\frac{1}{\chi} = \frac{T-\theta}{C}, \tag{5.2}$$

gives rise to C = 4.184 emu K mol^{-1} , θ = -1.07K, indicating a mainly paramagnetic behavior with possible existence of antiferromagnetic interaction. The effective paramagnetic moment calculated from the Curie constant is 5.78 μB/f.u. which is close to the expected value from the spin-only Mn^{2+}(5.9 μB/f.u.). No ferromagnetic behavior can be detected by the magnetization-field measurements carried out at 5 K, which shows a single non-linear curve. This confirms that the Mn^{2+} ion in such system exits in a paramagnetic state, with possibly weak antiferromagnetic coupling with its neighbors (Zr^{4+} or W^{6+} with empty *d*-orbital)

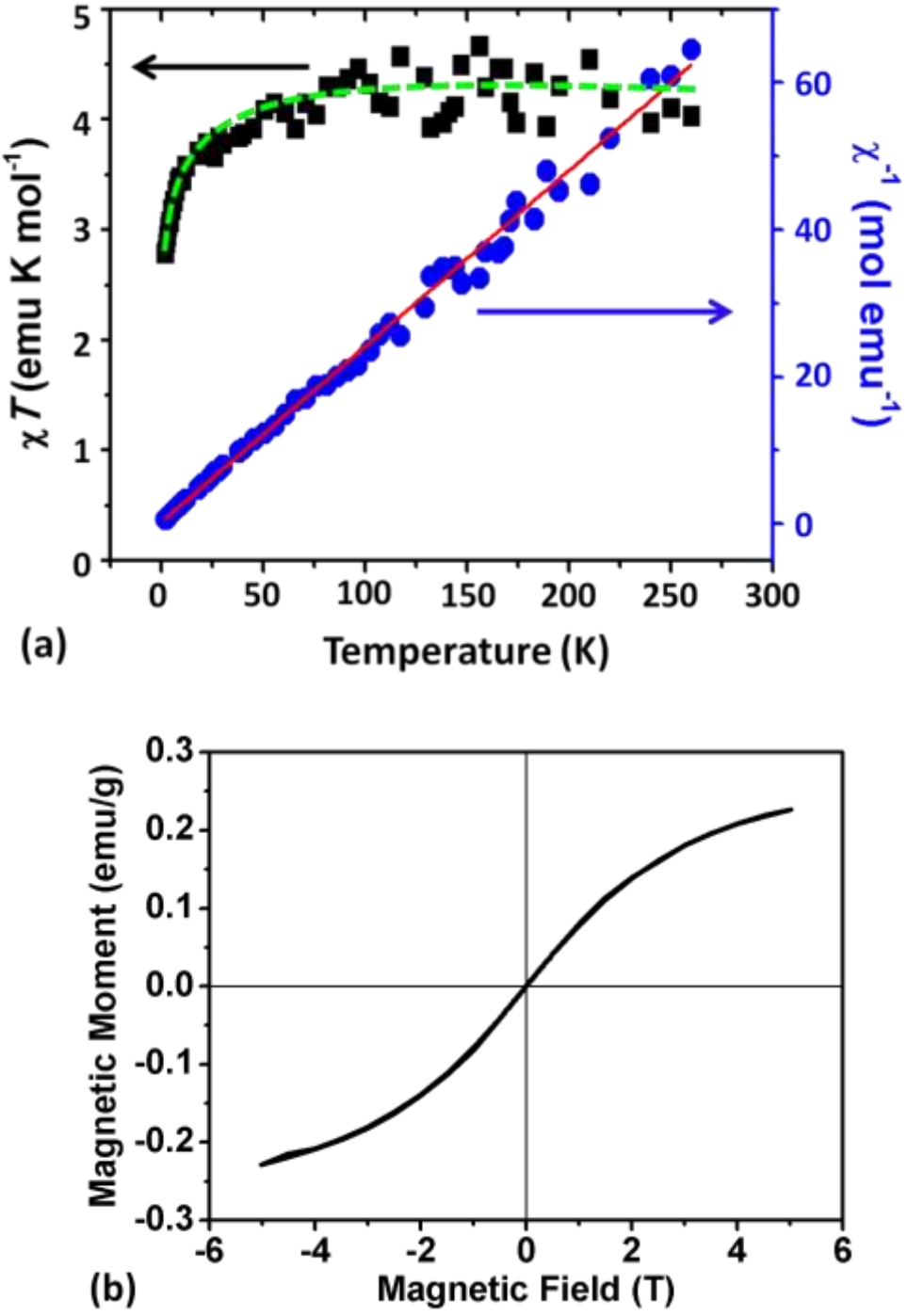

Figure 5.4 (a) Temperature dependences of χT and 1/χ for 0.99$PbZrO_3$-0.01Pb($Mn_{1/2}W_{1/2}$)O_3. (b) Variation of magnetic moment as a function of magnetic field for the same sample measured at 5K.

The variation of the dielectric constant (ε') as a function of temperature for the (1-x)$PbZrO_3$–x$Pb(Mn_{1/2}W_{1/2})O_3$ ceramics is shown in Fig. 5.5 (a). Only the data of 10^5 Hz are presented since no frequency dispersion was observed. The values of dielectric constant are normalized in Fig. 5.5 (a) in order to reveal the effects of composition. For $0 \leq x \leq 0.08$, the AFE to PE phase transition is clearly seen by the sharp dielectric peak at T_C, similar to $PbZrO_3$[126]. For $x \geq 0.01$, an additional dielectric anomaly is observed (as marked by arrows in Fig. 5.5) at temperature slightly below the transition temperature T_C. This can be attributed to an AFE to FE phase transition, indicating the presence of a ferroelectric intermediate phase, as was observed in some other $PbZrO_3$-based antiferroelectrics[126, 136, 141, 142]. It can also be clearly observed that both the AFE-PE (T_C) and AFE-FE phase transition temperatures decrease with increasing x, i.e., T_C decreases from 222.5 ˚C in $PbZrO_3$ to 212.0 ˚C in x = 0.01, to 185.5 ˚C in x = 0.05, and to 161.1 ˚C in x = 0.08. A similar trend was observed in the $PbZrO_3$–$Pb(Mg_{1/2}W_{1/2})O_3$ system[136]. According to a recent study on W-doped $PbZrO_3$[143], T_C decreases dramatically with the increase of W-doping level. Therefore, it is possible that the drop in T_C in the $PbZrO_3$–$Pb(M_{1/2}W_{1/2})O_3$ solid solution systems (M = Mg^{2+} or Mn^{2+}) is due to the combined effects of tungsten-substitution and dipole frustration. More detailed studies on the intermediate ferroelectric phase are underway.

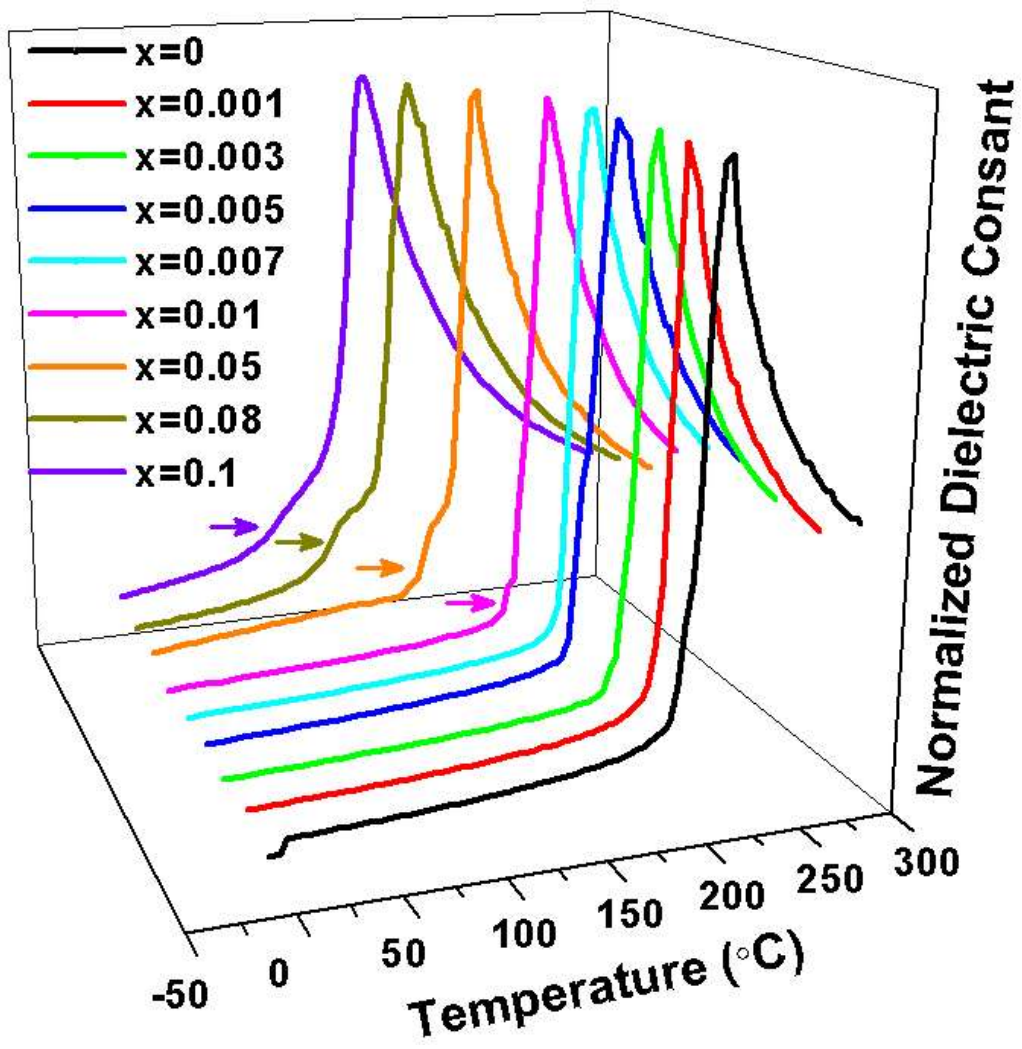

Figure 5.5 Temperature dependent dielectric constant (ε') of the (1-x)$PbZrO_3$–x$Pb(Mn_{1/2}W_{1/2})O_3$ ceramics measured at 10^5 Hz.

5.4.2. Study of ferroelectric intermediate phase

This part of the work focuses on the study of the structure and properties of the ferroelectric intermediate phase. The variation of the dielectric constant (ε') as a function of temperature for the (1-x)PZ–xPMnW solid solution is shown in Fig. 5.6. Only the data at 10^5 Hz are presented here since no frequency dispersion is observed. For x = 0 and 0.001, a typical AFE to PE phase transition is observed with a sharp peak in the dielectric constant at T_C. With increasing PMnW concentration, the T_C value of the solid

solution decreases with increasing concentration of PMnW, from 233 ˚C in $PbZrO_3$ (x = 0) to 230 ˚C in x = 0.001, to 223 ˚C in x=0.01, to 196 ˚C in x = 0.05, and to 157 ˚C in x = 0.1. This suggests that the addition of $Pb(Mn_{1/2}W_{1/2})O_3$ has disrupted the short-range dipolar ordering in $PbZrO_3$, making the AFE phase less stable and thereby reducing its T_C. For x = 0.01, 0.05 and 0.1, a weak dielectric anomaly appears at a temperature T_{A-F} below the Curie temperature T_C. In previous studies on $PbZrO_3$-based AFE materials, a similar dielectric anomaly was found and considered as the onset of an intermediate FE phase based on domain structure, crystal symmetry and P-E loops[126, 136, 141, 142]. It can be clearly observed that T_C and T_{A-F} decrease but ε_{max} increases with increasing x. The mechanism for the changes in T_C and ε_{max} can be attributed to multiple resources. On one hand, the study on W-doped $PbZrO_3$[143] shows dramatic decrease of T_C and increase of ε_{max} at higher W-doping level. In addition, the system starts to behave as a normal ferroelectrics when W-doping reaches 5%. On the other hand, study of the Mn-substitution effect on $(Pb_{0.832}Ba_{0.138}La_{0.02})(Zr_{0.7}Ti_{0.05}Sn_{0.25})O_3$ ceramic[144] shows the opposite effect with significant enhancement in antiferroelectricity, increasing T_C and decreasing ε_{max}. In our work, since the precursor method was used to ensure the 1:1 ratio between Mn^{2+} and W^{6+} ions at B/B'-site, one shall not consider the role of Mn^{2+} or W^{6+} ion individually but rather the macroscopic effect of $Pb(Mn_{1/2}W_{1/2})O_3$ as a whole in this system. It is known that the origin of ferroelectricity is the "softening" of some transverse optical (TO) modes at the center of the Brillouin zone. Such behavior relies strongly on long-range Columbic forces. By contrast, antiferroelectricity originates from the freezing of a TO mode at the boundary of the Brillouin zone and mostly depends on the short-range coupling interactions between neighboring dipoles. Therefore, the appearance of ferroelectric phase can be attributed to the cancellation of short-range interactions by long-range forces. According to the study of Cochran *et al.*[145], The transverse optical (TO) soft-mode frequency can be expressed as:

$$\omega_{\mathrm{TO}}^2 = \left(\frac{1}{\mu}\right)[(\mathrm{SRF}) - (\mathrm{LRF}) + \gamma\mathrm{T}] \,, \tag{5.3}$$

where μ is the reduced mass, SRF and LRF stand for the short-range forces and long-range Columbic forces, respectively, and γT is the perturbation of the harmonic approximation from the anharmonic contribution. In addition, the Lyddane-Sachs-Teller

(LST)[146] equation demonstrates the correlation between the dielectric constant and the mode frequency as follows:

$$\frac{\varepsilon}{\varepsilon_\infty} = \prod_i \left[\frac{(\omega_{LO})_i^2}{(\omega_{TO})_i^2}\right], \tag{5.4}$$

where ε_∞ is the visible range dielectric constant, ω_{LO} and ω_{TO} are the longitudinal and transverse optic phonon frequencies for various modes. Since the longitudinal optical mode does not go "soft" with temperature change, the weakening of SRF (or strengthening of LRF) will reduce the value of ω_{TO}, leading to a significant increase in dielectric constant at the phase transition temperature with only a small amount of PMnW substitution, as shown in Fig. 5.6. Therefore, our dielectric results confirm that, consistent with Cochran's formula and the LST model, the short-range dipole interactions in pure $PbZrO_3$ have been disrupted by the substitution of $Pb(Mn_{1/2}W_{1/2})O_3$, which favors long-range dipole ordering in the PZ-PMnW solid solution.

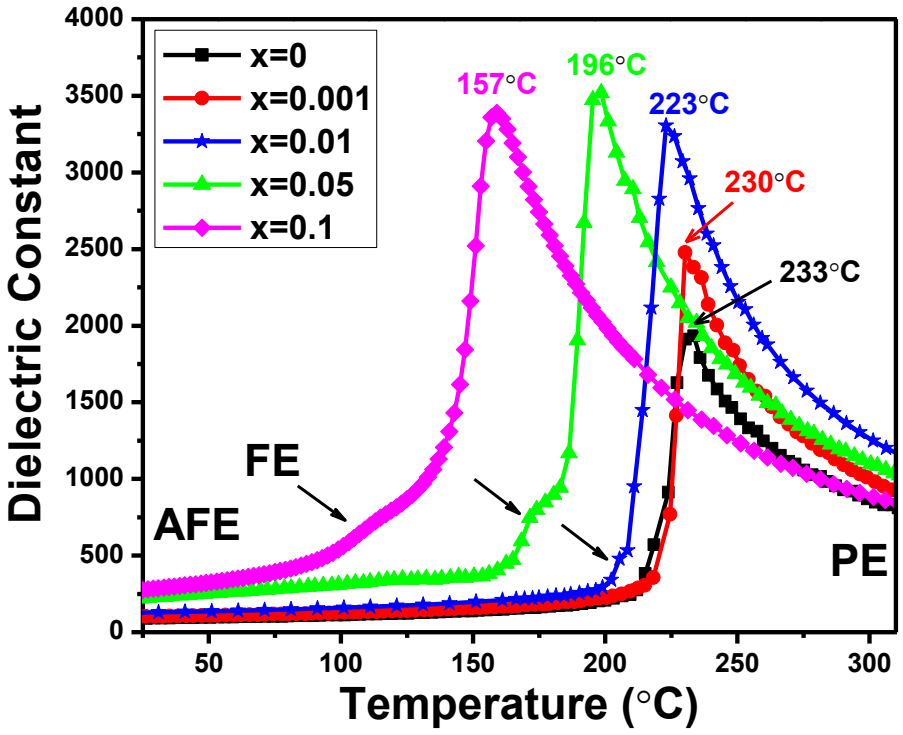

Figure 5.6 Variation of dielectric constant of (1-x)$PbZrO_3$–x$Pb(Mn_{1/2}W_{1/2})O_3$ as a function of temperature measured at 10^5 Hz frequency upon heating, with x=0, 0.001, 0.01, 0.05 and 0.1. The temperatures of the AFE – FE transition, T_{A-F}, and of the AFE/FE – PE transition, T_C, are indicated by arrows.

In the (1-x)PZ-xPMnW system, Mn^{2+} is a transition metal ion with partially filled *d*-orbitals (in high spin d^5 configuration) as demonstrated in Chapter 5.41. A high content of $Pb(Mn_{1/2}W_{1/2})O_3$ will naturally lead to increased conductivity. Therefore, ceramics of relatively low PMnW content (x=0.01) were chosen to investigate the electrical properties of the solid solution. The polarization-electric field relationship of 0.99$PbZrO_3$-0.01$Pb(Mn_{1/2}W_{1/2})O_3$ measured at selected temperatures is shown in Fig. 5.7. Below 150 ˚C, an external field up to 100 kV/cm is not high enough to switch the AFE dipoles, and therefore the P-E curve shows a near-linear dependence, reminiscent of a normal dielectric behavior [Fig. 5.7 (a)]. Above 150 ˚C, double hysteresis P-E loops start to appear, revealing the AFE nature of the solid solution, as shown in Fig. 5.7 (b). From 205 ˚C to 225 ˚C ($T > T_{A-F}$), P-E loops exhibit a distorted hysteretic shape with the appearance of a small remanent polarization (P_r) of 1.0 - 2.6 μC/cm^2 [Fig. 5.7(c)]. However, no clean ferroelectric hysteresis loop is obtained, indicating that the intermediate phase is of FE nature but it coexists with a significant amount of the AFE phase. Above T_C, another type of double hysteresis loop appears at 225 ˚C with a large induced polarization up to 22 μC/cm^2 (at E = 30 kV/cm) and a small P_r (0.7 μC/cm^2) [Fig. 5.7 (d)]. This kind of double hysteresis loop at $T \geq T_C$ is believed to arise from a first order FE to PE phase transition[147]. With further increase of temperature to above T_C (225 ˚C), a higher external electric field (E > 30 kV/cm) is required to display the double hysteresis loop, which is also consistent with the previously reported phenomenon associated with the first order phase transition[147, 148]. The values of the maximum induced polarization (P_{ind}) taken from the measured P-E loops are plotted as a function of temperature in Fig. 5.8 for x = 0.01. It can be seen that P_{Ind} increases with increasing temperature and peaks at T_{A-F}. The P_{ind} value then decreases in the temperature range where the AFE and FE phases coexist. Upon further heating close to T_C, P_{ind} increases sharply before dropping again above T_C. This variation allows us to assign the nature of various phases as a function of T for 0.99$PbZrO_3$-0.01$Pb(Mn_{1/2}W_{1/2})O_3$, which includes

the AFE up to T_{A-F}, a mixture of the AFE and FE phases in the intermediate region between T_{A-F} and T_C and the PE phase above T_C.

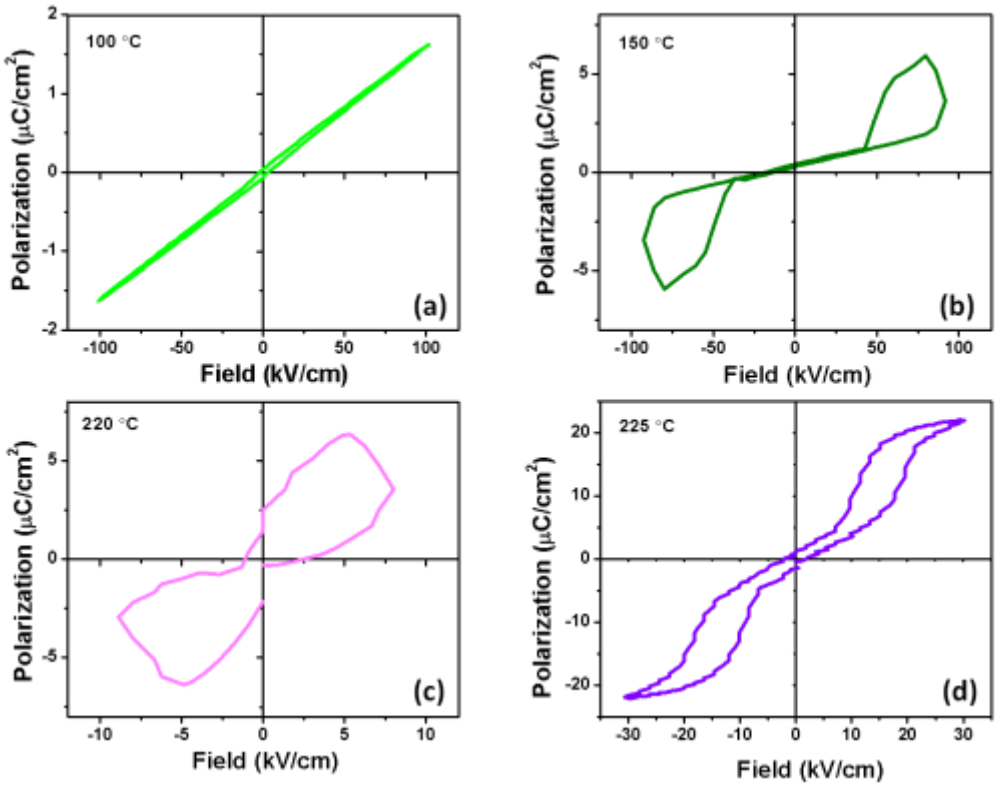

Figure 5.7 Polarization – electric field relations for the $0.99PbZrO_3$-$0.01Pb(Mn_{1/2}W_{1/2})O_3$ ceramic sample displayed at selected temperatures

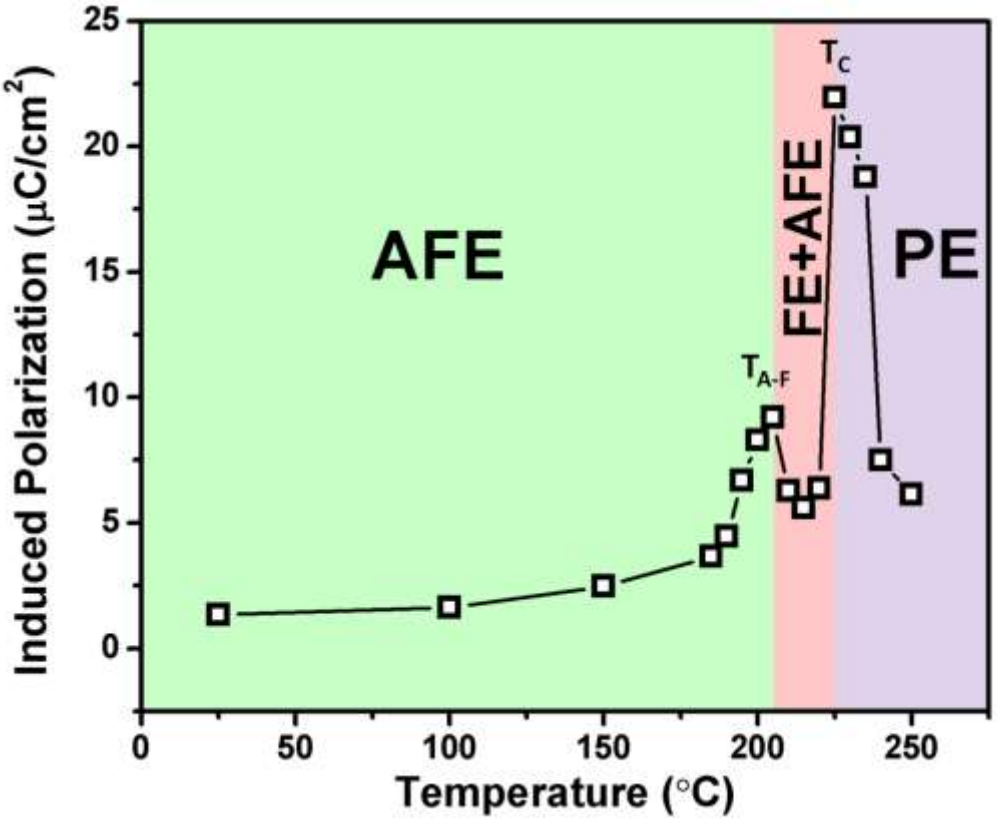

Figure 5.8 Variation of the induced polarization as a function of temperature for the $0.99PbZrO_3$-$0.01Pb(Mn_{1/2}W_{1/2})O_3$ ceramic sample, indicating the AFE phase below T_{A-F}, the PE phase above T_C and a mixture of the intermediate FE phase and the AFE phase at $T_{A-F} < T < T_C$.

Direct evidence in support of the ferroelectric nature of the intermediate phase is obtained by pyroelectric current measurements, as shown in Fig. 5.9. Field cooling (FC) is performed with an electric field of 100 kV/cm applied upon cooling through T_C, from 242 ˚C to 225 ˚C. If the intermediate phase is ferroelectric, FC will turn the material into a poled state with a non-zero net polarization. Accordingly, the subsequent zero-field-heating (ZFH) after FC through T_C brings the system back to the non-polar paraelectric state with the decay of the polarization which can be detected as a sharp pyroelectric current peak. That is exactly what is measured in Fig. 5.9, Curve (1), confirming the FE nature of the intermediate phase. In a similar way, the subsequent zero-field-cooling (ZFC) after FC through the FE → AFE transition temperature results in the transformation from the poled ferroelectric state into the low temperature AFE non-polar

state, as revealed by the sharp pyroelectric current peak at T_{A-F} [Fig. 5.9, Curve (2)]. When the FC is performed with a negative polarity of the field, the subsequent ZFH and ZFC runs lead to negative current peaks at T_C and T_{A-F}, respectively, as shown in Fig. 5.9 by Curves (3) and (4). These results confirm both the polarization switching and, thereby, the ferroelectricity for the intermediate phase.

The spontaneous polarization (P_s) can be calculated from the integration of the pyroelectric current according to the following relationship:

$$P_s = \int p_i dT = \frac{1}{A}\int i\left(\frac{dt}{dT}\right) dT, \quad (5.5)$$

where p_i is the pyroelectric coefficient in the unit of $\frac{C}{m^2K}$, A is the area of the electrode, *i* is pyroelectric current, and $\left(\frac{dt}{dT}\right)$ is the temperature change rate (a constant here). The *Ps* value calculated from the ZFH (after FC) peak is 32.16 μC/cm^2, which is larger than the value of 24.50 μC/cm^2 calculated from the ZFC (after FC) peak. If the field-induced FE phase were entirely converted to the non-polar AFE phase during ZFC through T_{A-F}, the P_s value calculated from the ZFC current peak would be the same as the one calculated from the ZFH peak at which the poled FE phase transforms into the nonpolar PE phase. The significantly smaller polarization measured at T_{A-F} than at T_C can be attributed to the contribution from the incommensurate structure in the AFE phase. According to Tan *et al.*,[130] in $PbZrO_3$-based AFE ceramics with incommensurate modulations, ferroelectricity can be enhanced by the thickening of 180˚ domain walls which tends to retain the long-range polar order after the release of external field. Therefore, it is plausible that the macroscopic polarization induced upon FC is not totally released during the ZFC run through T_{A-F}, but partly retained in the low temperature AFE phase due to the incommensurate modulations, leading to a weaker pyroelectric current peak and thereby a smaller polarization calculated thereafter. Curve (5) in Fig. 5.9 is the baseline measured upon ZFC after ZFH up to T_C, which shows no pyroelectric current, confirming the non-polar nature of the material without applying an electric field.

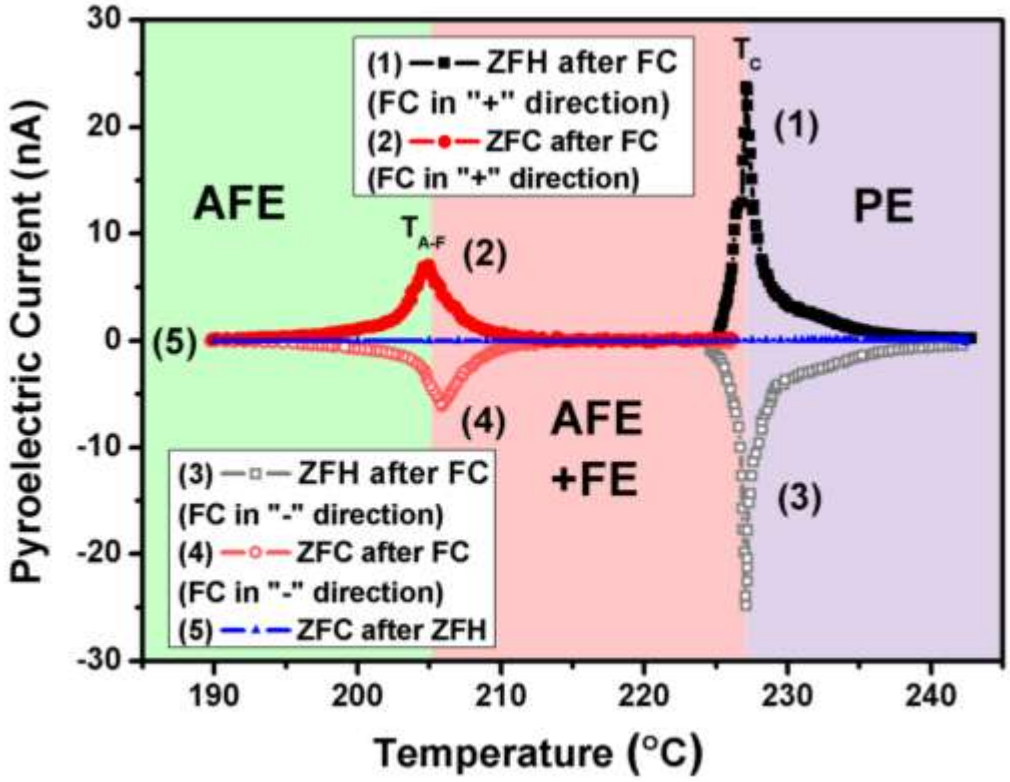

Figure 5.9 Pyroelectric measurement on (1-x)$PbZrO_3$-x$Pb(Mn_{1/2}W_{1/2})O_3$ (x=0.001) with various conditions.

As the intermediate phase appears in a relatively wider temperature range at higher x, the composition of 0.9$PbZrO_3$–0.1$Pb(Mn_{1/2}W_{1/2})O_3$ was chosen for structural analysis in order to determine the symmetry of the ferroelectric phase. X-ray diffraction patterns obtained at various temperatures and the variations of the calculated lattice parameters as a function of temperature for the different phases are shown in Fig. 5.10. For a better understanding of the nature of the symmetry, the indices for the orthorhombic $\sqrt{2}a\times2\sqrt{2a}\times2a$ setting and pseudocubic $a\times a\times a$ setting (a = cell dimension of paraelectric cubic phase) are both labeled in Fig. 5.10. Conversion method was shown in the previous section. It is known that the antiparallel displacements of Pb^{2+} in the AFE phase of $PbZrO_3$ are associated with the wave vector $q_\Sigma = \left(\frac{1}{4}\frac{1}{4}0\right)_{pc}$ [13, 23]. Therefore, the degree of Pb^{2+} ordering can be assessed by examining the evolution of the $\frac{1}{4}(hkl)$ reflection.

The intensity of the $\left(\frac{7}{4}\frac{-1}{4}0\right)_{pc}$ and $\left(\frac{5}{4}\frac{-3}{4}1\right)_{pc}$ peaks shows a decreasing trend with increasing temperature up to 130 ˚C at which point the system is primarily in the ferroelectric phase. Based on the dielectric measurements, the intermediate FE phase exists within the temperature range from 110 ˚C to 157 ˚C for 0.9PZ-0.1PMnW. It is noticed that, although very weak, the splitting of the $\{111\}_{pc}$ and $\{200\}_{pc}$ peaks can still be observed up to 150 ˚C, suggesting a possible coexistence of both the AFE and FE phases from 110 ˚C until T_C. From Fig. 5.10 (a), it can be seen that the $(111)_{pc}$ peak becomes more and more asymmetrical upon heating and eventually splits into two peaks starting at 110 ˚C, indicating the onset of a rhombohedral phase. The most unambiguous evidence in support of the rhombohedral symmetry can be found from the XRD pattern recorded at T = 130 ˚C, with a clear splitting of the pseudocubic $\{111\}_{pc}$ peak into the rhombohedral (111) and $(11\bar{1})$ peaks, as marked by an arrow in Fig. 5.10 (a). Since no tilting peaks are observed in the XRD patterns, *R*3*m* symmetry is found to be the best fit for the structure of the intermediate FE phase. Subsequently, Rietveld refinements are performed based upon *Pbam* symmetry for the XRD patterns recorded from 25 to 110 ˚C, a mixture of *Pbam* with *R*3*m* phases from 110 to 150 ˚C and the $Pm\bar{3}m$ symmetry above 150 ˚C. An example of fitting profile is shown in Fig. 5.10 (b) for T = 130 ˚C using a mixture of *Pbam* and *R*3*m* symmetries. The variations of the refined lattice parameters for the different phases as a function of temperature upon heating are presented in Fig. 5.10 (c). The continuous variation through $T_{A\text{-}F}$ of the orthorhombic lattice parameters, a_{pc}, b_{pc} and c_{pc}, confirms that the nonpolar AFE phase subsists in the temperature range from $T_{A\text{-}F}$ to T_C, coexisting with the intermediate ferroelectric *R*3*m* phase.

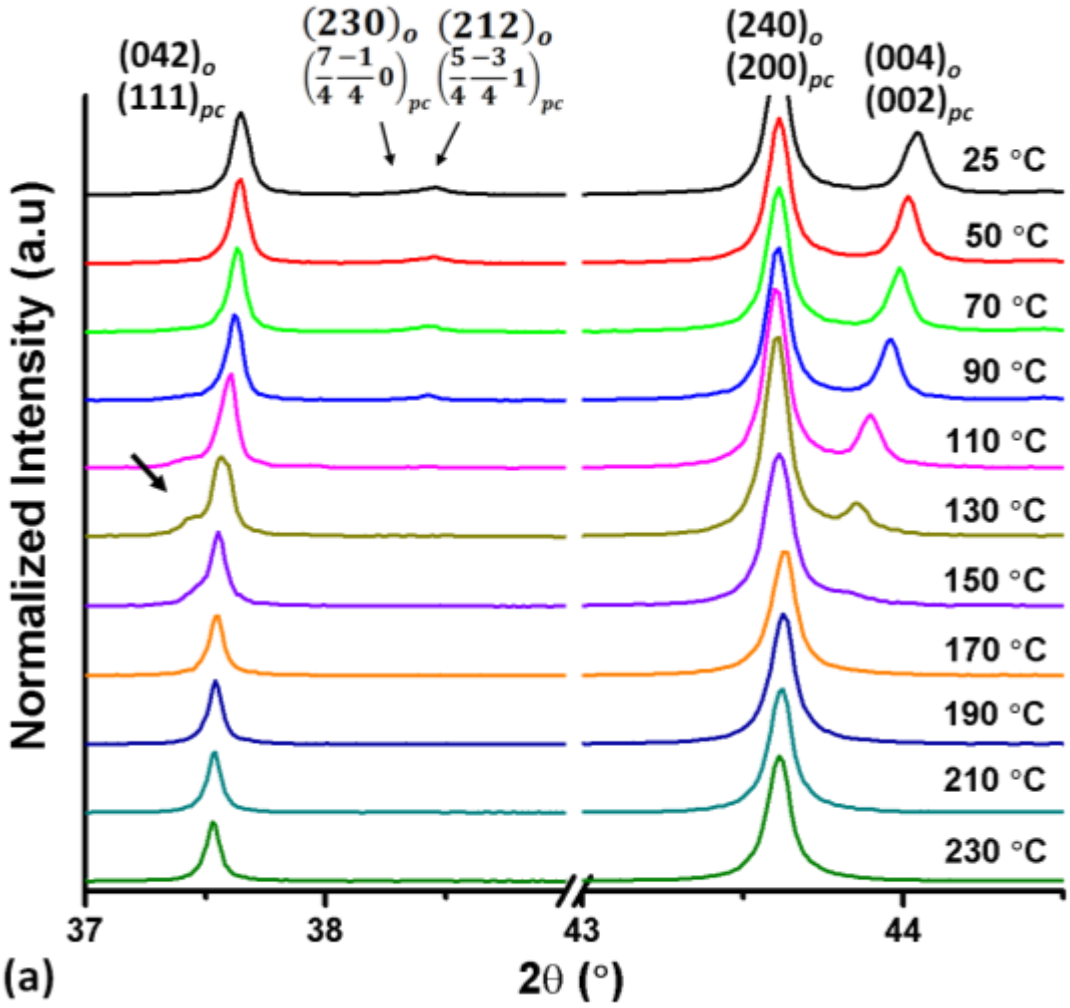
$(042)_o$
$(111)_{pc}$
$(230)_o$
$\left(\frac{7}{4}\frac{-1}{4}0\right)_{pc}$
$(212)_o$
$\left(\frac{5}{4}\frac{-3}{4}1\right)_{pc}$
$(240)_o$
$(200)_{pc}$
$(004)_o$
$(002)_{pc}$
25 °C
50 °C
70 °C
90 °C
110 °C
130 °C
150 °C
170 °C
190 °C
210 °C
230 °C
Normalized Intensity (a.u)
37
38
43
44
2θ (°)
(a)

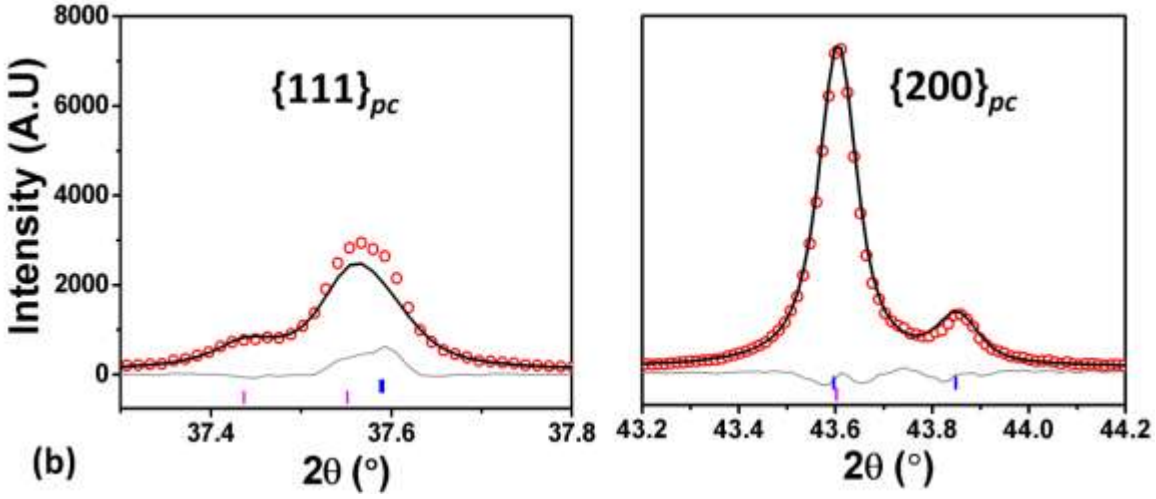
8000
6000
4000
2000
0
Intensity (A.U)
$\{111\}_{pc}$
37.4
37.6
37.8
2θ (°)
(b)
$\{200\}_{pc}$
43.2
43.4
43.6
43.8
44.0
44.2
2θ (°)

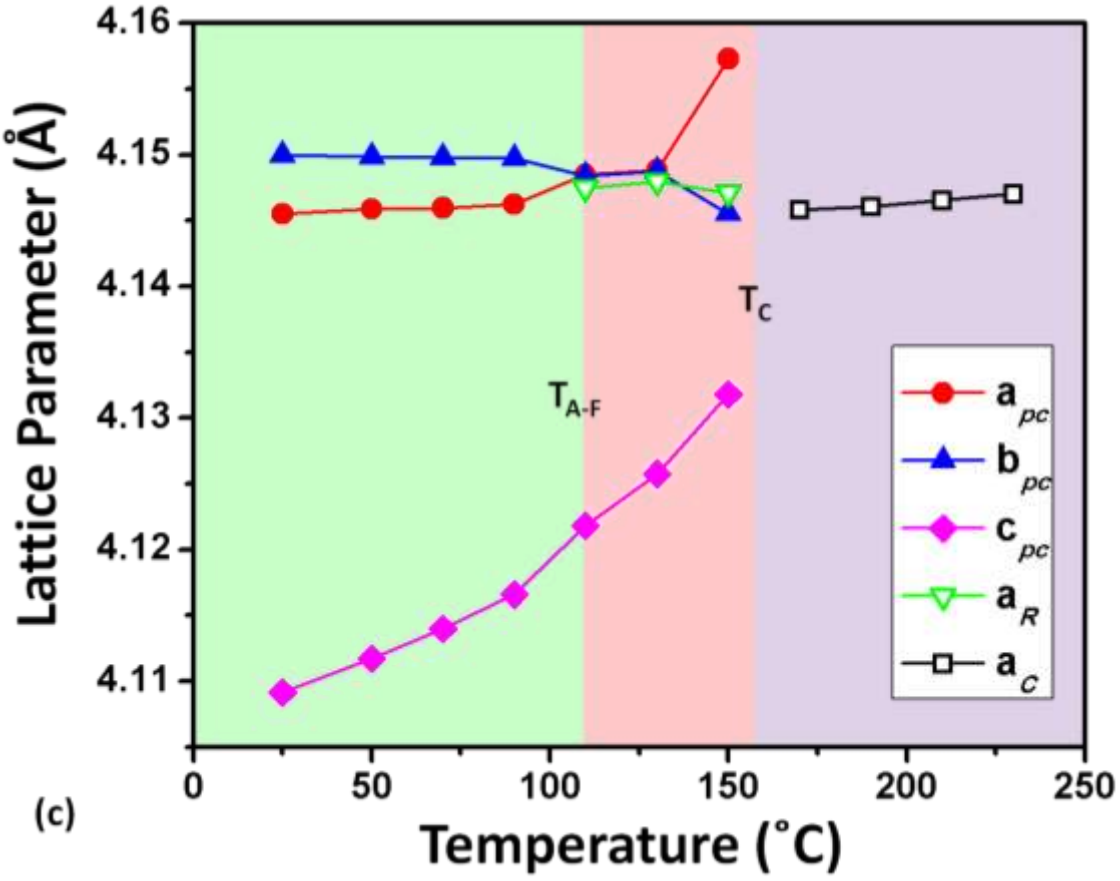

Figure 5.10 (a) XRD patterns of $0.9PbZrO_3$–$0.1Pb(Mn_{1/2}W_{1/2})O_3$ measured at various temperatures. Peaks are labeled in both orthorhombic (o) and pseudocubic (pc) settings. The arrow on the left indicates the splitting of $\{111\}_{pc}$ peak for T = 130 ˚C. (b) Rietveld refinement profiles of the $\{111\}_{pc}$ and $\{200\}_{pc}$ peaks at T = 130 ˚C. Experimental data: red dots; Calculated fit: black line; Difference plot: grey line; Ticks below: *Pbam* (blue) and *R*3*m* (pink) peak positions. (c) Variation of lattice parameters of the different phases with temperature, where a_{pc}, b_{pc} and c_{pc} are the orthorhombic lattice parameters converted into the pseudocubic unit cell, and a_R and a_C represent the lattice parameters for the rhombohedral and cubic phases, respectively.

5.5. Conclusion

A new solid solution of $(1-x)PbZrO_3$-$xPb(Mn_{1/2}W_{1/2})O_3$ (PZ-xPMnW) has been synthesized in of complex perovskite structure by solid state reaction. The symmetry of the system is refined to be *Pbam* for $0 \leq x \leq 0.1$. As the PMnW concentration increases,

the critical field is decreased, indicating a softening of the antiferroelectric order in PZ, while at the same time the induced polarization is increased. The reduction of the critical field makes it possible to avoid the dielectric breakdown during the AFE – FE switching at high electric field and the increase of the induced polarization P_{Ind} enhanced the material's discharging ability. The ceramic density was significantly improved by the formation of possible transient eutectic liquid phases arising from the Pb/W-based oxides. Measurements of the magnetization by means of SQUID confirm that the Mn ion exists in a high spin state with a 2+ oxidation state. The softening of AFE order and the improvement in induced polarization demonstrated in this work make the PZ-PMnW antiferroelectric ceramics an interesting material system for such applications as energy storage devices.

An intermediate phase is found in the (1-x)$PbZrO_3$-x$Pb(Mn_{1/2}W_{1/2})O_3$ solid solution system between the low temperature AFE phase and the high temperature PE phases. It is shown to have FE properties by various characterization techniques. In particular, the pyroelectric current measurements provide convincing evidence for the polar nature and the switchability of the spontaneous polarization of the ferroelectric phase. Structural analysis from temperature-variable XRD data show that the intermediate phase has rhombohedral symmetry, space group *R3m*, which is compatible with ferroelectricity. The discovery of the intermediate FE phase in a binary solid solution where both end members are antiferroelectric points to a new direction for the study of antiferroelectric local structure, dipolar frustration and incommensurate modulations. On the other hand, the electrical properties of the PZ-PMnW solid solution indicate a soft antiferroelectric feature which is of interest for potential applications in high-density energy storage capacitors and high-strain transducers.

Chapter 6: General Conclusion and Future Directions

6.1. $Pb(In_{1/2}Nb_{1/2})O_3$–$Pb(Mg_{1/3}Nb_{2/3})O_3$–$PbTiO_3$ (PIN-PMN-PT) Ternary Ferroelectric Solid Solution System

Rhombohedral, monoclinic (M_A/M_C) and tetragonal phases are found in coexistence in a compositionally segregated xPIN-yPMN-zPT (nominal composition x/y/z = 30/35/35) single crystal. Polarized light microscope measurements on the R area of the single crystal show significant change in both extinction angle and birefringence at 80˚C, indicating a phase transition from R to a monoclinic phase upon heating. X-ray diffraction on ceramic series with compositions across the morphotropic phase boundary suggests the nature of this phase transition is likely R→M_A. PLM measurements on the M_C area of the crystal reveal all three M_C domains distinguished by their unique temperature-dependent extinction angles θ_M. A pseudo-binary phase diagram of the (1-z)(PINPMN)-zPT system with the MPB region of the ternary PIN-PMN-PT solid solution has been proposed based on the structural, optical and dielectric results of both single crystal and ceramic systems. It helps clarify the MPB phase components of the ternary system, understand the structure and properties of the high performance ternary piezocrystals.

The monoclinic M_C phase found in the MPB region of ferroelectric solid solution is considered important for applications as well as for fundamental research. Conventionally, it is believed that for a thermodynamically stable phase, electric-field/pressure/temperature-induced phase transitions should always be reversible, i.e. the structure of a crystal is mainly determined by its as-grown composition whereas field/pressure/temperature-induced strain shall be released when annealed above its Curie temperature. Here we report a novel phenomenon that after applying electric field on a $Pb(In_{1/2}Nb_{1/2})O_3$-$Pb(Mg_{1/3}Nb_{2/3})O_3$-$PbTiO_3$ (PIN-PMN-PT) single crystal, the original monoclinic phase is transformed irreversibly into a tetragonal phase and cannot be restored to its original monoclinic phase after repeated high temperature treatments.

Based on previous theoretical calculations and current experimental results, it is proposed that the electric field causes collective migration or hopping of oxygen vacancies onto more stable planer positions during the poling. This ordered oxygen vacancy arrangement and the associated internal field favors the development of tetragonal 90 ˚domains upon subsequent cooling through T_C. This oxygen vacancy-based mechanism is supported by the different domain structure observed under PLM, and the different dielectric properties measured before and after thermal treatment in O_2 atmosphere, which is found to restore the M_C phase by compensating the oxygen vacancies eliminating the vacancy-related tetragonal phase memory effect. The role of oxygen vacancies in the formation of domain structure and phase symmetry found in this work may help understanding other domain engineering and phase transition phenomenon.

The domain memory effect and the polarization reversal phenomenon associated with the R→M_A phase transition are discovered in the PIN-PMN-PT single crystal and ceramics and are interpreted by a polarization-reversal model. This phenomenon enables certain types of ferroelectric materials to restore their polarization state and domain structure after experiencing FE→FE phase transition from a higher symmetry phase (R) to a lower symmetry phase (M_A) upon heating. A direct consequence of the polarization reversal effect and domain memory phenomenon is that the piezoelectric coefficient of the material does not undergo degradation following the R→M_A phase transition as opposed to the conventional R→T MPB transition which leads to the depoling and severe degradation of the piezo-performance. Our results, observations and interpretations provide a new guidance in the designing and selection of piezo/ferroelectric with a wider operation temperature range: the MPB composition undergoing a higher symmetry to a lower symmetry phase can exhibit the improved temperature tolerance compared with the conventional MPB compositions, becoming the material of choice for high depoling temperature and high performance piezoelectrics for a wide range of applications as electromechanical transducers.

For future work, advanced techniques such as neutron diffraction can be applied on PIN-PMN-PT single crystals in order to reveal the evolution of polarization in its MPB region. The detailed influence of oxygen vacancies on structure and electrical properties shall also be further analyzed by *in-situ* TEM or piezoresponse force microscopy (PFM) under

the variation of electric field. As for the study of the influence of FE→FE phase transition on electrical properties, materials with multiple FE→FE phase transitions such as $BaTiO_3$ shall be further studied in order to verify the polarization reversal model. For example, the rhombohedral-orthorhombic phase transition at -80 ˚C and the orthorhombic-tetragonal phase transition at 10 ˚C in $BaTiO_3$ can serve as good subjects to study the depoling effect related to FE→FE phase transition.

6.2. $Pb(Mg_{1/2}W_{1/2})O_3$-$Pb(Zn_{1/2}W_{1/2})O_3$ Solid Solution System

New antiferroelectric solid solution of $(1-x)Pb(Mg_{1/2}W_{1/2})O_3$ - $xPb(Zn_{1/2}W_{1/2})O_3$ (PMW-PZW) is synthesized by solid state reaction in the form of ceramics. The solubility limit of $Pb(Zn_{1/2}W_{1/2})O_3$ into the PMW perovskite structure reaches 30%. The antiferroelectric to paraelectric phase transition is revealed by dielectric anomalies at T_C which increases as with increasing PZW concentration, from 40.8 ˚C (x = 0) to 67.9 ˚C (x = 30%), indicting an enhancement of the antiferroelectric order as a result of the PZW substitution for PMW. Polarization - field variation exhibits a nearly linear relation with a very weak hysteresis up to a high electric field of 125 kV/cm, indicating a high dielectric strength. This antiferroelectric PMW-PZW ceramics with low processing temperature, low dielectric constant, low dielectric loss and high dielectric strength at room temperature form a new class of dielectric materials potentially useful as ceramic insulators. Further research can be focused on the study the local structure of Zn^{2+} center with neutron diffraction method and the further enhancement of ceramic quality such as high pressure sintering technique.

6.3. $Pb(Mg_{1/2}W_{1/2})O_3$-$Pb(Mn_{1/2}W_{1/2})O_3$ Solid Solution System

The solid solution of complex perovskite $(1-x)Pb(Mg_{1/2}W_{1/2})O_3$ - $xPb(Mn_{1/2}W_{1/2})O_3$ has been synthesized by a precursor-based 2-step solid-state reaction method similar to the synthesis of PMW-PZW. XRD measurements at room temperature confirm that the system crystallizes in an orthorhombic *Pmcn* antiferroelectric phase with a low concentration of Mn^{2+} ($x \leq 0.35$) and undergoes a phase transition from the $Pmcn$ to a cubic $Fm\bar{3}m$ phase where x is increased to 0.35. The displacements of Pb^{2+} ion along

both the *y*-and *z*-direction decreases, indicating a reduced antiferroelectricity with the increase of x. EPR spectroscopy shows that Mn adopts 2+ oxidation state with high-spin (S = 5/2), which is confirmed by magnetic measurement by SQUID. The simulation and analysis of the EPR spectrum indicates that the Mn^{2+} ion is in the center of a slightly distorted oxygen octahedron with tetragonal symmetry. The grain size of the solid solution ceramics is significantly enlarged by the formation of transient eutectic liquid phases arising from the Pb/W-based oxides. The dielectric measurement reveals the T_C of AFE-PE phase transition first increases slightly with increasing x until x=0.2, then decreases significantly at x>0.2. The decrease of T_C at x>0.2 is interpreted as a weakening of the AFE order, which is caused by the reduced Pb^{2+}-displacements whereas the cause of the increase in T_C at x≤0.2 is still unclear. Based on the T_C values from the dielectric measurements, a partial phase diagram of the solid solution is proposed which delimits the orthorhombic antiferroelectric *Pmcn* phase from the cubic paraelectric $Fm\bar{3}m$ phase is drawn. It also shows the composition induced *Pmcn* → $Fm\bar{3}m$ phase transition, consistent with the structural analysis by XRD. Combined wtih our previous study on Mn-doped PIN-PMN-PT ferroelectric solid solution, this work provides a deeper insight for the behavior of Mn^{2+} ion in Pb-based perovskites and guideline for the design of Mn^{2+}-containing anti/ferroelectric functional material in the future. For future work, advanced characterization techniques can be applied to investigate the local structure of Mn^{2+} center using neutron diffraction method and solid state NMR.

6.4. $PbZrO_3$-$Pb(Mn_{1/2}W_{1/2})O_3$ Antiferroelectric Solid Solution System

A new solid solution of (1-x)$PbZrO_3$-x$Pb(Mn_{1/2}W_{1/2})O_3$ (PZ-xPMnW) has been synthesized in of complex perovskite structure by solid state reaction. The symmetry of the system is refined to be *Pbam* for 0≤x≤0.1. As the PMnW concentration increases, the critical field is decreased while at the same time the induced polarization is increased, indicating a softening of the antiferroelectric order in PZ. The reduction of the critical field makes it possible to avoid the dielectric breakdown during the AFE – FE switching at high electric field and the increase of the induced polarization P_{Ind} enhanced the material's discharging ability. The ceramic density is significantly improved by the

formation of possible transient eutectic liquid phases arising from the Pb/W-based oxides. Measurements of the magnetization by means of SQUID confirm that the Mn ion exists in a high spin state with a 2+ oxidation state. The softening of AFE order and the improvement in induced polarization demonstrated in this work make the PZ-PMnW antiferroelectric ceramics an interesting material system for such applications as energy storage devices.

An intermediate phase is found in the (1-x)$PbZrO_3$-x$Pb(Mn_{1/2}W_{1/2})O_3$ solid solution system between the low temperature AFE phase and the high temperature PE phases. It is shown to have FE properties by various characterization techniques. In particular, the pyroelectric current measurements provide convincing evidence for the polar nature and the switchability of the spontaneous polarization of the ferroelectric phase. Structural analysis from temperature-variable XRD data show that the intermediate phase has rhombohedral symmetry, space group *R3m*, which is compatible with ferroelectricity. The discovery of the intermediate FE phase in a binary solid solution where both end members are antiferroelectric points to a new direction for the study of antiferroelectric local structure, dipolar frustration and incommensurate modulations.

For future work, more chemical modification on PZ-based antiferroelectric material shall be carried out. Growth of $PbZrO_3$-$Pb(M_{1/2}W_{1/2})O_3$ (M = Mn^{2+}, Zn^{2+},Mg^{2+}, Co^{2+}, etc) single crystal shall provide further information on composition/temperature induced antiferroelectric→ferroelectric phase transition. Chemical modifications of PZ-based antiferroelectric ceramic with Ti^{4+}, Hf^{4+}, Nb^{5+}, La^{3+} can also be tested in order to find the optimum composition for high-density energy storage capacitors and high-strain transducers.

References

1. R. D. Shannon, Acta Crystallogr A **32** (Sep1), 751-767 (1976).

2. A. Asamitsu, Y. Moritomo, Y. Tomioka, T. Arima and Y. Tokura, Nature **373** (6513), 407-409 (1995).

3. S. W. Cheong and M. Mostovoy, Nature Materials **6** (1), 13-20 (2007).

4. Y. Moritomo, A. Asamitsu, H. Kuwahara and Y. Tokura, Nature **380** (6570), 141-144 (1996).

5. Y. Maeno, H. Hashimoto, K. Yoshida, S. Nishizaki, T. Fujita, J. G. Bednorz and F. Lichtenberg, Nature **372** (6506), 532-534 (1994).

6. Z. G. Ye, Mrs Bull **34** (4), 277-283 (2009).

7. S. E. Park and T. R. Shrout, J Appl Phys **82** (4), 1804-1811 (1997).

8. C. B. Sawyer and C. H. Tower, Phys Rev **35** (3), 0269-0273 (1930).

9. G. H. Haertling, J Am Ceram Soc **82** (4), 797-818 (1999).

10. D. Damjanovic, Rep Prog Phys **61** (9), 1267-1324 (1998).

11. R. E. Cohen, Nature **358** (6382), 136-138 (1992).

12. B. Jaffe, P Ire **49** (8), 1264-& (1961).

13. C. Haas, Phys Rev **140** (3A), A863-& (1965).

14. B. Noheda, D. E. Cox, G. Shirane, J. Gao and Z. G. Ye, Phys Rev B **66** (5) (2002).

15. Z. G. Ye, B. Noheda, M. Dong, D. Cox and G. Shirane, Phys Rev B **64** (18) (2001).

16. H. X. Fu and R. E. Cohen, Nature **403** (6767), 281-283 (2000).

17. S. E. E. Park and W. Hackenberger, Curr Opin Solid St M **6** (1), 11-18 (2002).

18. G. A. Smolenskii, A. I. Agranovskaya and V. A. Isupov, Soviet Physics-Solid State **1** (6), 907-908 (1959).

19. G. Baldinozzi, P. Sciau and P. A. Buffat, Solid State Commun **86** (9), 541-544 (1993).

20. G. Baldinozzi, P. Sciau, M. Pinot and D. Grebille, Acta Crystallogr B **51**, 668-673 (1995).

21. E. Sawaguchi, H. Maniwa and S. Hoshino, Phys Rev **83** (5), 1078-1078 (1951).

22. E. Sawaguchi and T. Kittaka, J Phys Soc Jpn **7** (3), 336-337 (1952).

23. H. Fujishita and S. Hoshino, J Phys Soc Jpn **53** (1), 226-234 (1984).

24. G. A. Samara, Phys Rev B **1** (9), 3777-& (1970).

25. A. M. Glazer, K. Roleder and J. Dec, Acta Crystallogr B **49**, 846-852 (1993).

26. J. S. Speck, M. Degraef, A. P. Wilkinson, A. K. Cheetham and D. R. Clarke, J Appl Phys **73** (11), 7261-7267 (1993).

27. D. Viehland, Phys Rev B **52** (2), 778-791 (1995).

28. C. Heremans and H. L. Tuller, J Appl Phys **87** (3), 1458-1466 (2000).

29. M. F. c. Ladd, *Structure determination by x-ray crystallography : analysis by x-rays and neutrons*. (Springer, New York, 2012).

30. A. K. Jonscher, *Dielectric relaxation in solids*. (Chelsea Dielectrics Press, London, 1983).

31. W. C. McCrone, L. B. McCrone and J. G. Delly, *Polarized light microscopy*. (Ann Arbor Science Publishers, Ann Arbor, Mich., 1978).

32. A. A. Bokov, X. F. Long and Z. G. Ye, Phys Rev B **81** (17) (2010).

33. W. L. Warren, B. A. Tuttle and D. Dimos, Appl Phys Lett **67** (10), 1426-1428 (1995).

34. G. A. Smolenskii and A. I. Agranovskaya, Sov Phys-Sol State **1** (10), 1429-1437 (1960).

35. L. E. Cross, S. J. Jang, R. E. Newnham, S. Nomura and K. Uchino, Ferroelectrics **23** (3-4), 187-191 (1980).

36. S. Nomura and K. Uchino, Ferroelectrics **50** (1-4), 523-528 (1983).

37. B. Jaffe, W. R. Cook and H. L. Jaffe, *Piezoelectric ceramics*. (Academic Press, London, New York,, 1971).

38. Y. M. Jin, Y. U. Wang, A. G. Khachaturyan, J. F. Li and D. Viehland, Phys. Rev. Lett. **91** (19) (2003).

39. K. A. Schonau, L. A. Schmitt, M. Knapp, H. Fuess, R. A. Eichel, H. Kungl and M. J. Hoffmann, Phys Rev B **75** (18) (2007).

40. W. F. Rao and Y. U. Wang, Appl Phys Lett **91** (5) (2007).

41. M. Ahart, M. Somayazulu, R. E. Cohen, P. Ganesh, P. Dera, H. K. Mao, R. J. Hemley, Y. Ren, P. Liermann and Z. G. Wu, Nature **451** (7178), 545-U542 (2008).

42. D. Vanderbilt and M. H. Cohen, Phys Rev B **63** (9) (2001).

43. J. J. Yao, H. Cao, W. W. Ge, J. F. Li and D. Viehland, Appl Phys Lett **95** (5), - (2009).

44. A. K. Singh and D. Pandey, Phys Rev B **67** (6), - (2003).

45. A. K. Singh, D. Pandey and O. Zaharko, Phys Rev B **68** (17), - (2003).

46. A. K. Singh and D. Pandey, Phys Rev B **67** (6) (2003).

47. Y. Uesu, M. Matsuda, Y. Yamada, K. Fujishiro, D. E. Cox, B. Noheda and G. Shirane, J Phys Soc Jpn **71** (3), 960-965 (2002).

48. S. Fushimi and T. Ikeda, J Am Ceram Soc **50** (3), 129-& (1967).

49. M. Dong and Z. G. Ye, J Cryst Growth **209** (1), 81-90 (2000).

50. L. Zhang, M. Dong and Z. G. Ye, Mat Sci Eng B-Solid **78** (2-3), 96-104 (2000).

51. Q. H. Lu, X. F. Long and Y. H. Hu, Crystengcomm **12** (12), 4317-4320 (2010).

52. H. S. Luo, G. S. Xu, P. C. Wang and Z. W. Yin, Ferroelectrics **231** (1-4), 685-690 (1999).

53. H. S. Luo, G. S. Xu, H. Q. Xu, P. C. Wang and Z. W. Yin, Jpn J Appl Phys 1 **39** (9B), 5581-5585 (2000).

54. E. F. Alberta and A. S. Bhalla, Mater Lett **29** (1-3), 127-129 (1996).

55. N. Yasuda, H. Ohwa, K. Ito, M. Iwata and Y. Ishibashi, Ferroelectrics **230** (1-4), 417-422 (1999).

56. Y. Hosono, Y. Yamashita, H. Sakamoto and N. Ichinose, Jpn J Appl Phys 1 **42** (2A), 535-538 (2003).

57. Y. Hosono, Y. Yamashita, K. Hirayama and N. Ichinose, Japanese Journal of Applied Physics Part 1-Regular Papers Brief Communications & Review Papers **44** (9B), 7037-7041 (2005).

58. S. L. Swartz and T. R. Shrout, Mater Res Bull **17** (10), 1245-1250 (1982).

59. K. T. Zawilski, M. C. C. Custodio, R. C. DeMattei, S. G. Lee, R. G. Monteiro, H. Odagawa and R. S. Feigelson, J Cryst Growth **258** (3-4), 353-367 (2003).

60. J. Luo, W. Hackenberger, S. J. Zhang and T. R. Shrout, Ultrason, 261-264 (2008).

61. D. Vanderbilt and M. H. Cohen, Phys Rev B **63** (9), 094108 (2001).

62. C. S. Tu, V. H. Schmidt, I. C. Shih and R. Chien, Phys Rev B **67** (2), - (2003).

63. B. Noheda, Z. Zhong, D. E. Cox, G. Shirane, S. E. Park and P. Rehrig, Phys Rev B **65** (22), - (2002).

64. B. Noheda, D. E. Cox, G. Shirane, J. Gao and Z. G. Ye, Phys Rev B **66** (5), 054104 (2002).

65. F. Jona and G. Shirane, *Ferroelectric crystals*. (Pergamon Press, Oxford, New York,, 1962).

66. Z. G. Ye, Ferroelectrics **184**, 193-208 (1996).

67. V. A. Shuvaeva, A. M. Glazer and D. Zekria, J Phys-Condens Mat **17** (37), 5709-5723 (2005).

68. J. Cheng, Y. Yang, Y. H. Tong, S. B. Lu, J. Y. Sun, K. Zhu, Y. L. Liu, G. G. Siu and Z. K. Xu, J Appl Phys **105** (5) (2009).

69. B. Noheda, D. E. Cox, G. Shirane, S. E. Park, L. E. Cross and Z. Zhong, Phys Rev Lett **86** (17), 3891-3894 (2001).

70. H. M. Christen, J. H. Nam, H. S. Kim, A. J. Hatt and N. A. Spaldin, Phys Rev B **83** (14), - (2011).

71. A. A. Bokov and Z. G. Ye, Phys Rev B **66** (9) (2002).

72. L. H. Luo, D. Zhou, Y. X. Tang, Y. M. Jia, H. Q. Xu and H. S. Luo, Appl Phys Lett **90** (10) (2007).

73. Y. H. Chen, S. Hirose, D. Viehland, S. Takahashi and K. Uchino, Jpn J Appl Phys 1 **39** (8), 4843-4852 (2000).

74. A. A. Bokov and Z. G. Ye, Journal of Applied Physics **95** (11), 6347-6359 (2004).

75. Z. G. Ye, B. Noheda, M. Dong, D. Cox and G. Shirane, Phys Rev B **6418** (18), - (2001).

76. A. A. Bokov and Z. G. Ye, Appl Phys Lett **92** (8) (2008).

77. P. Bao, F. Yan, X. M. Lu, J. S. Zhu, H. M. Shen, Y. N. Wang and H. S. Luo, Appl Phys Lett **88** (9), - (2006).

78. M. K. Durbin, J. C. Hicks, S. E. Park and T. R. Shrout, J Appl Phys **87** (11), 8159-8164 (2000).

79. D. M. Smyth, *The defect chemistry of metal oxides*. (Oxford University Press, New York ; Oxford, 2000).

80. K. Ohwada, K. Hirota, P. W. Rehrig, P. M. Gehring, B. Noheda, Y. Fujii, S. E. E. Park and G. Shirane, J Phys Soc Jpn **70** (9), 2778-2783 (2001).

81. Z. L. Liao, P. Gao, X. D. Bai, D. M. Chen and J. D. Zhang, J Appl Phys **111** (11) (2012).

82. C. H. Park and D. J. Chadi, Phys Rev B **57** (22), R13961-R13964 (1998).

83. Y. Kitanaka, Y. Noguchi and M. Miyayama, Phys Rev B **81** (9) (2010).

84. L. X. He and D. Vanderbilt, Phys Rev B **68** (13) (2003).

85. Y. M. Jin, Y. U. Wang, A. G. Khachaturyan, J. F. Li and D. Viehland, J Appl Phys **94** (5), 3629-3640 (2003).

86. H. Wang, J. Zhu, N. Lu, A. A. Bokov, Z. G. Ye and X. W. Zhang, Appl Phys Lett **89** (4) (2006).

87. C. S. Tu, V. H. Schmidt, I. C. Shih and R. Chien, Phys Rev B **67** (2) (2003).

88. D. La-Orauttapong, B. Noheda, Z. G. Ye, P. M. Gehring, J. Toulouse, D. E. Cox and G. Shirane, Phys Rev B **65** (14) (2002).

89. M. Amin, Ieee T Ultrason Ferr **52** (10), 1632-1637 (2005).

90. W. S. Chang, L. C. Lim, P. Yang and C. S. Tu, Appl Phys Lett **93** (8) (2008).

91. C. He, X. Z. Li, Z. J. Wang, X. F. Long, S. Y. Mao and Z. G. Ye, Chem Mater **22** (19), 5588-5592 (2010).

92. Y. Hosono, Y. Yamashita, H. Sakamoto and N. Ichinose, Jpn J Appl Phys 2 **41** (11A), L1240-L1242 (2002).

93. S. J. Zhang, J. Luo, W. Hackenberger and T. R. Shrout, J Appl Phys **104** (6) (2008).

94. B. Jaffe, W. R. Cook and H. L. Jaffe, *Piezoelectric ceramics*. (Academic Press, London ; New York, 1971).

95. S. B. Majumder, S. Bhattacharyya, R. S. Katiyar, A. Manivannan, P. Dutta and M. S. Seehra, J Appl Phys **99** (2) (2006).

96. N. Chau, H. N. Nhat, N. H. Luong, D. L. Minh, N. D. Tho and N. N. Chau, Physica B **327** (2-4), 270-278 (2003).

97. I. Grinberg, M. R. Suchomel, P. K. Davies and A. M. Rappe, J Appl Phys **98** (9) (2005).

98. T. Fujita, O. Fukunaga, T. Nakagawa and S. Nomura, Mater Res Bull **5** (10), 759-& (1970).

99. W. F. Smith, *Principles of materials science and engineering*, 2nd ed. (McGraw-Hill, New York, 1990).

100. I. Grinberg, M. R. Suchomel, W. Dmowski, S. E. Mason, H. Wu, P. K. Davies and A. M. Rappe, Phys. Rev. Lett. **98** (10) (2007).

101. M. A. Hentati, M. Guennou, H. Dammak, H. Khemakhem and M. P. Thi, J Appl Phys **107** (6) (2010).

102. A. Molak, E. Talik, A. Kruczek, A. Paluch, A. Ratuszna and Z. Ujma, Mat Sci Eng B-Solid **128** (1-3), 16-24 (2006).

103. J. Blasco, R. I. Merino, J. Garcia and M. C. Sanchez, J Phys-Condens Mat **18** (7), 2261-2271 (2006).

104. G. Subias, J. Blasco, J. Garcia, J. Herrero-Martin and M. C. Sanchez, J Phys-Condens Mat **21** (7) (2009).

105. W. J. Lee and N. K. Kim, J Mater Sci **43** (10), 3608-3611 (2008).

106. R. E. Eitel, C. A. Randall, T. R. Shrout, P. W. Rehrig, W. Hackenberger and S. E. Park, Japanese Journal of Applied Physics Part 1-Regular Papers Short Notes & Review Papers **40** (10), 5999-6002 (2001).

107. W. K. Choo, H. J. Kim, J. H. Yang, H. Lim, J. Y. Lee, J. R. Kwon and C. H. Chun, Jpn J Appl Phys 1 **32** (9B), 4249-4253 (1993).

108. S. Stoll and A. Schweiger, J Magn Reson **178** (1), 42-55 (2006).

109. A. Abragam and B. Bleaney, *Electron paramagnetic resonance of transition ions*. (Oxford University Press, Oxford, 2012).

110. M. D. Glinchuk, V. V. Laguta, L. P. Yurchenko, J. Rosa, L. Jastrabik, V. V. Eremkin and V. G. Smotrakov, J Appl Phys **111** (1) (2012).

111. I. Mishra, R. Kripal and S. Misra, Chinese Phys Lett **29** (3) (2012).

112. B. Milsch, Phys Status Solidi A **133** (2), 455-464 (1992).

113. R. L. Carlin, *Magnetochemistry*. (Springer, Dusseldorf, Germany, 1986).

114. J. B. Goodenough, Phys Rev **117** (6), 1442-1451 (1960).

115. L. L. Y. Chang, Journal of the American Ceramic Society **54** (7), 357-358 (1971).

116. W. D. Kingery, Journal of Applied Physics **30** (3), 301-306 (1959).

117. W. D. Kingery and M. D. Narasimhan, J Appl Phys **30** (3), 307-310 (1959).

118. O. Khamman, X. Tan, S. Ananta and R. Yimnirun, J Mater Sci **44** (7), 1868-1872 (2009).

119. C. H. Lu, J Mater Sci **31** (3), 699-705 (1996).

120. C. H. Lu, Journal of the American Ceramic Society **77** (10), 2529-2535 (1994).

121. Z. Ren, N. Zhang, S. Huo, J. Y. Y. Wong and Z. G. Ye, Ferroelectrics **464** (1), 27-34 (2014).

122. Z. H. Ren, N. Zhang, X. F. Long and Z. G. Ye, J Am Ceram Soc **97** (6), 1700-1703 (2014).

123. I. Barbur, I. Ardelean, G. Borodi and A. Veres, Mater Lett **28** (1-3), 175-177 (1996).

124. I. Barbur and I. Ardelean, Phase Transit **74** (4), 367-373 (2001).

125. Z. Ren and Z. G. Ye, Ferroelectrics **464** (1), 130-135 (2014).

126. G. Shirane, E. Sawaguchi and Y. Takagi, Phys Rev **84** (3), 476-481 (1951).

127. C. T. Blue, J. C. Hicks, S. E. Park, S. Yoshikawa and L. E. Cross, Appl Phys Lett **68** (21), 2942-2944 (1996).

128. S. E. Park, M. J. Pan, K. Markowski, S. Yoshikawa and L. E. Cross, J Appl Phys **82** (4), 1798-1803 (1997).

129. H. He and X. Tan, Appl Phys Lett **85** (15), 3187-3189 (2004).

130. X. L. Tan, C. Ma, J. Frederick, S. Beckman and K. G. Webber, J Am Ceram Soc **94** (12), 4091-4107 (2011).

131. W. Y. Pan, C. Q. Dam, Q. M. Zhang and L. E. Cross, J Appl Phys **66** (12), 6014-6023 (1989).

132. D. Berlincourt, H. Jaffe, H. H. A. Krueger and B. Jaffe, Appl Phys Lett **3** (5), 90-92 (1963).

133. R. P. Brodeur, K. W. Gachigi, P. M. Pruna and T. R. Shrout, J Am Ceram Soc **77** (11), 3042-3044 (1994).

134. Benguigu.L, J Solid State Chem **3** (3), 381-& (1971).

135. B. Jaffe, R. S. Roth and S. Marzullo, J Res Nat Bur Stand **55** (5), 239-254 (1955).

136. N. Vittayakorn, P. Charoonsuk, P. Kasiansin, S. Wirunchit and B. Boonchom, J Appl Phys **106** (6) (2009).

137. D. Viehland, X. H. Dai, J. F. Li and Z. Xu, J Appl Phys **84** (1), 458-471 (1998).

138. D. Berlincourt, B. Jaffe and H. H. A. Krueger, J Phys Chem Solids **25** (7), 659-& (1964).

139. H. He and X. Tan, Phys Rev B **72** (2) (2005).

140. B. Jaffe, R. S. Roth and S. Marzullo, J Appl Phys **25** (6), 809-810 (1954).

141. Z. K. Xu, X. H. Dai, D. Viehland, D. A. Payne, Z. Li and Y. D. Jiang, J Am Ceram Soc **78** (8), 2220-2224 (1995).

142. B. A. Scott and G. Burns, J Am Ceram Soc **55** (7), 3 (1972).

143. T. Sa, N. Qin, G. Yang and D. Bao, Appl Phys Lett **102** (17), 4 (2013).

144. Q. F. Zhang, M. Y. Fan, S. L. Jiang, T. Q. Yang and X. Yao, Appl Phys Lett **101** (6) (2012).

145. W. Cochran, Adv Phys **9** (36), 387-423 (1960).

146. R. H. Lyddane, R. G. Sachs and E. Teller, Phys Rev **59** (8), 673-676 (1941).

147. W. J. Merz, Phys Rev **91** (3), 513-517 (1953).

148. L. E. Cross, Philos Mag **44** (357), 1161-1170 (1953).